Plant-Derived Biosorbents for Pollutant Removal and Carbon Nanoparticle Synthesis

A Dissertation

Submitted in partial fulfillment for the degree of

Doctor of Philosophy

Partha Protim Bakal

(Roll no. 156152010)

Thesis Supervisor: Prof. Gopal Das

Thesis Co-Supervisor: Prof. Aiyagari Ramesh

Centre for the Environment

Indian Institute of Technology Guwahati

Assam, India-781039, India

November, 2023

Dedicated to my Family and Friends

INDIAN INSTITUTE OF TECHNOLOGY GUWAHATI
Centre for the Environment

STATEMENT

I do hereby declare that the matter embodied in this thesis is the result of investigations carried out by me in the Centre for the Environment, Indian Institute of Technology Guwahati, India, under the guidance of Prof. Gopal Das, Department of Chemistry & Centre for the Environment, and Prof. Aiyagari Ramesh (co-supervisor), Department of Biosciences and Bioengineering, Indian Institute of Technology Guwahati, India. In keeping with the general practice of reporting scientific observations, due acknowledgments have been made wherever this work is based on the findings of other investigators.

Date: 01.11.2023

Place: IIT Guwahati (Partha Protim Bakal)

INDIAN INSTITUTE OF TECHNOLOGY GUWAHATI

Centre for the Environment

CERTIFICATE

This is to certify that **Mr. Partha Protim Bakal** (156152010) has been working under our supervision since January 2016 as a part-time registered Ph.D. student. His thesis entitled **"Plant-Derived Biosorbents for Pollutant Removal and Carbon Nanoparticle Synthesis "** is a genuine record of the results obtained from the research work carried out under our supervision in the Centre for the Environment, Indian Institute of Technology Guwahati, Assam-781039, India. We are forwarding his thesis to submit for the award of the degree of Doctor of Philosophy from this institute. We hereby certify that he has fulfilled all the requirements, according to the rules of this institute, regarding the investigations embodied in his thesis, and this work has not been submitted elsewhere for a degree.

Prof. Aiyagari Ramesh
(Thesis Co-Supervisor)
Professor, Dept. of Biosciences & Bioengineering
IIT Guwahati, Assam - 781039, India

Prof. Gopal Das
(Thesis Supervisor)
Professor, Department of Chemistry
IIT Guwahati, Assam - 781039, India

Acknowledgment

Firstly, I would like to express my deep appreciation to my supervisors Prof. Gopal Das and Prof. Aiyagari Ramesh, for their guidance, support, and encouragement throughout my Ph.D. journey. Their expertise, knowledge, and patience have been invaluable to me, and I am extremely grateful for the time and effort they have invested in my research.

I would also like to thank my Doctoral committee members Prof. Lal Mohan Kundu (Chairman of Doctoral committee), Prof. Ranjan Tamuli, and Prof. Senthilkumar Sivaprakasam, for their constructive feedback, insightful comments, and critical evaluation of my work. Their contribution has greatly improved the quality of my thesis.

I want to thank the Head of the Centre for the Environment, Prof. Utpal Bora, and previous HoC, Prof. Vikash Kumar Dubey and Prof. Mihir Kumar Purkait, under whose administration I was able to carry out my research work. I am also thankful to the Centre for the Environment and Central Instrument Facility, IIT Guwahati, for providing the necessary facilities to fulfill my Ph.D. thesis objectives.

I am grateful to my colleagues and fellow Ph.D. students who have shared their idea, provided feedback, and offered moral support throughout my research. I am particularly indebted to Dr. Mothe Gopi Kiran, Dr. Narendra Naik Deshavath, Dr. Lalit Goswami, Dr. Rajneesh Kumar, Dr. Arnab Ghosh, Dr. Deepa Sachan, Dr. Rahul Verma, Dr. Sayantan Sinha, Md. Aquib Jawed,Mr. Niladri Samanta, Mr. Prangan Duarah, Ms. Debolina Ghosh, Ms. Neha Gautam who has been my research partners for several years. Their enthusiasm, creativity, and friendship have been a constant source of inspiration and motivation.

I would like to thank the Centre for the Environment staff members Dr. Deepmoni Deka, Mr. Kaustubh Rakshit, Mr. Rajiv Kumar Gogoi, Mr. Supriyo Kumar Das, and Mr. Mridul Das, for their technical support and administrative assistance.

I want to express my heartfelt gratitude to my family members, who have been a constant source of love, support, and inspiration throughout my Ph.D. journey. First and foremost, I would like to thank my parents (Mr. Lokeswar Bakal and Mrs. Lilyma Bakal) for their unwavering love and support. Their encouragement, guidance, and sacrifice have allowed me to pursue my dreams and achieve my goals. I would also like to thank my spouse (Mrs. Jyotismita Gogoi) and children's (Dhanushka Bakal and Dushyant Bakal) for their love, understanding, and patience. Their support and encouragement have been invaluable to me, and I could not have completed my Ph.D. without their love and support. Their constant presence in my life has made this journey all the more meaningful and rewarding.

I would like to express my profound gratitude to Almighty God for being my guiding light and a constant source of strength during my Ph.D. journey. Throughout this challenging and transformative experience, I have felt his presence in every step of the way, and attribute my success to his divine grace.

In conclusion, I would like to express my sincere appreciation to all those who have contributed to my Ph.D. journey. Your support, encouragement, and guidance have been invaluable to me, and I could not have done this without you. Thank you.

Partha Protim Bakal

This synopsis report entitled "**Plant-Derived Biosorbents for Pollutant Removal and Carbon Nanoparticle Synthesis"** have been split up into five chapters based on the results and experiments performed during the research periods**.**

Chapter 1: Introduction & Literature Review:

This chapter briefly introduces potential biosorbents from plant-derived materials, activated biochar, and hydrochar to remove organic (dye) and inorganic (heavy metals) pollutants from an aqueous environment. Nowadays, plant-based biomass materials attracted many researchers over the last decades in water remediation. Plant-based biosorbents are especially attractive due to their eco-friendly nature, cost-effectiveness, and recyclability. Therefore, sufficient research has been carried out, and experiments were optimized for large-scale or industrial applications. Generally, biosorbents can be derived from animals, plants, and microbial wastes. The animal sources are fishery, and animal husbandry, while plant-based biomass is forestry and agriculture. Herein our focus is on the plant-based biosorbent for synthesizing activated biochar and hydrochar for the removal of dyes and heavy metals and synthesis of carbon dots for metal sensing applications. The significant components present in biomass are cellulose, hemicellulose, lignin, and proteins, chitin, starch which gives firmness and strength to the material. Since carbon is the most abundant element in plant biomass and recently various literature has reported the synthesis of carbon dots, we have also explored the possibility of carbon dot synthesis and its application towards heavy metal sensing applications. After its discovery in 2004, much literature has been reported on synthesizing carbon dots from biomass. Carbon dots (CDs) are one of the current growing research areas in carbon nanotechnology due to their fluorescence property. It has various advantages over earlier conventional quantum dots due to its low toxicity, biocompatibility, wide application in bioimaging, sensing, and photocatalytic degradation of multiple pollutants. Hydrochar is generated during synthesizing carbon dots (hydrothermal treatment), which can be utilized to remove heavy metal ions, and carbon dots can be used for heavy metal sensing applications. Activated biochar and hydrochar generated from the natural raw biosorbent got much attention due to its high surface area and pore volume, which can be used for the removal of both organic and inorganic pollutants from an aqueous environment. In recent years, water pollution has been increasing due to industrial activity, urbanization, and growth in population. Water bodies are polluted by various pollutants, such as heavy metal ions, dyes, and pharmaceutical compounds. They are toxic to humans and other creatures, even at low concentrations. Since these pollutants are soluble in water, hence it is transported to our bodies which may cause different types of diseases, including cancer. Therefore the elimination of these pollutants from wastewater is a matter of concern. Various wastewater treatment techniques are available, which include chemical

methods (Chemical oxidation, precipitation, coagulation, ion exchange, solvent extraction, hydrolysis), physical methods (Adsorption, filtration, distillation, sedimentation), and biological methods (Rotating biological contractor, activated sludge, reactors, and tracking filters). Among these techniques, adsorption has been chosen due to its cost-effective, low energy consumption, simple of operation, and recyclability.

Chapter 2: Experimental Methods and Characterization

This chapter is an extensive report of the various methods used in the synthesis of biosorbent, activated biochar, hydrochar, synthesis of carbon dots and their characterization with the specifications of instruments employed in the characterization of the synthesized Biosorbents and detailed analysis are represented in depth.

Chapter 3: A comparative study of raw *vs.* activated biochar derived from "*Ricinus communis*" stem for preferential adsorption of cationic dyes. *(Water conservation Science & Engineering,* 8, 19 (2023). https://doi.org/10.1007/s41101-023-00192-1*)*

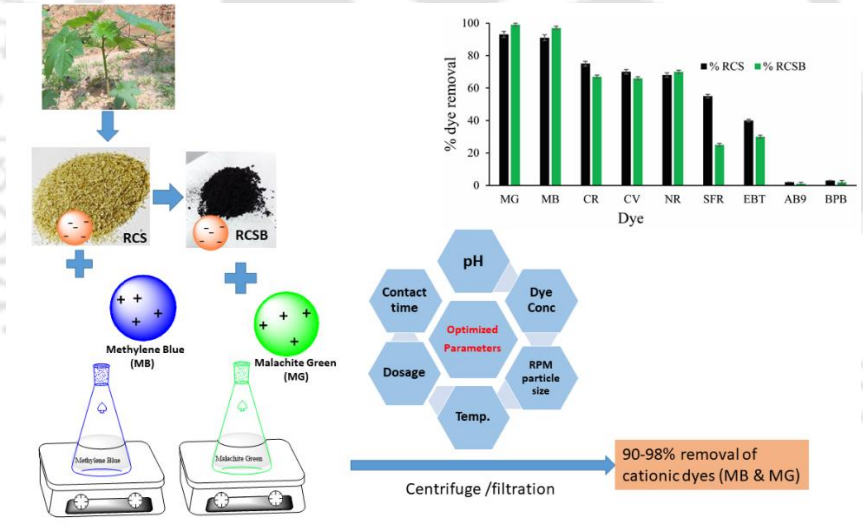

Ricinus communis stem (RCS) was chemically activated with potassium carbonate (K_2CO_3) and heated at 300˚C to produce low-temperature *Ricinus communis stem*-activated biochar (RCSB). These two biosorbents (RCS and RCSB) were used for the removal of methylene blue (MB) and malachite green (MG) preferentially from synthetic aqueous solutions. Various analytical techniques were used to explore the surface morphology, surface area, crystallinity, elemental composition, and functional groups of natural and potassium carbonate-activated *Ricinus communis* stem. Adsorption experiments were performed to evaluate the effect of pH, adsorbent dosage, contact time, initial dye concentration, stirring speed, particle size, and temperature. Initially, adsorption experiments were carried out with nine cationic and anionic dyes. Among

these dyes, two cationic dye, malachite Green (MG) and methylene Blue (MB) shows more than 90% dye removal using RCS (92%) and RCSB (99%). The maximum adsorption capacities q_e (mg g^{-1}) of all four systems are MB-RCSB: 80.7 mg g^{-1}, MG-RCSB 60 mg g^{-1}, MB-RCS: 68.71 mg g^{-1}, and MG-RCS 51 mg g^{-1}, respectively. The kinetics and equilibrium data were best fitted with the intra-particle diffusion kinetics model (R^2=1) and the langmuir isotherm model. The thermodynamic parameters support the feasible, spontaneous, and exothermic adsorption in the temperature range of 293-323K. Desorption experiments were carried out at pH 2 with an efficiency of ~97 %. Regeneration study indicates biosorbents can be recycled in up to five cycles. The present studies suggest using RCS and RCSB has potential application as eco-friendly biosorbent for efficient removal of MG and MB dyes up to 99%.

Chapter 4: Biochar Derived from the Stem of *Ricinus communis* and *Colocasia esculanta*: Efficient Adsorbent for the Removal of Cd(II) and Pb(II) Ions from an Aqueous Environment (J. Water Chem. Technol. 45, 200–210 (2023)
https://doi.org/10.3103/S1063455X23030025

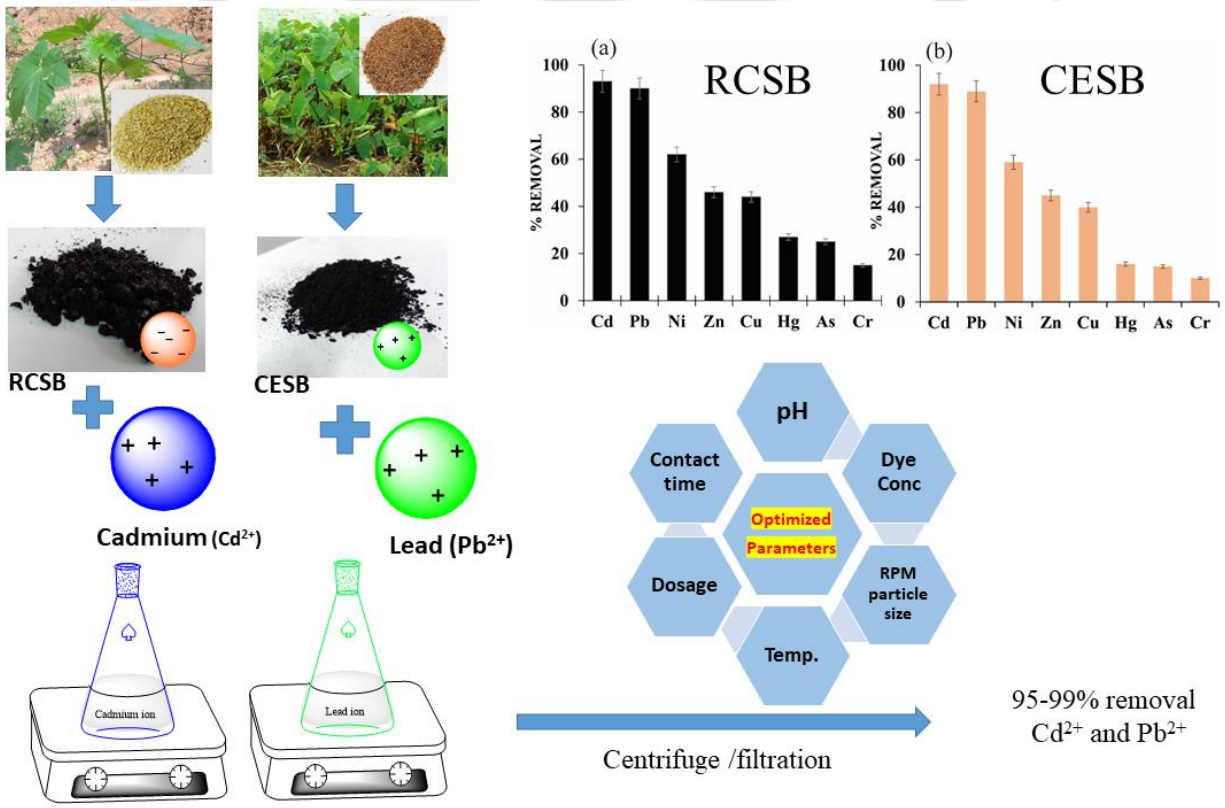

Potassium carbonate-activated biochar derived from the stems of *Ricinus communis* (RCSB) and *Colocasia esculanta* (CESB) were used for the efficient removal of Cd^{2+} and Pb^{2+} (50 mg L^{-1} each) from synthetic water. These two ions adsorption is higher than other tested heavy metal ions (*viz.* Ni^{2+}, Zn^{2+}, Cu^{2+}, Hg^{2+}, As^{5+}, and Cr^{6+} ions). Different adsorption parameters (pH, metal concentration, time, dosage, and temperature) were studied to get the optimized result. The

adsorption isotherm, kinetics, thermodynamics, and mechanism were studied. The adsorption isotherm studies indicate that heavy metal ion biosorption follows the Freundlich isotherm. The adsorption kinetic model can be best described as pseudo-second order, and the adsorption mechanism is physical adsorption. The optimum conditions for the adsorption of Cd^{2+} and Pb^{2+} by activated biochars were: adsorption time 120 minutes, temperature 20-25^{o}C, and pH between 6.8 and 7.2. The adsorption capacity of Cd-RCSB, Cd-CESB was ~204 mg.g $^{-1,}$ and Pb-RCSB, Pb-CESB was found to be ~200 mg.g $^{-1}$ and ~208 mg.g $^{-1}$. The adsorption thermodynamics showed that the adsorption was a spontaneous and endothermic process. Desorption studies show that biochar can be recycled for up to 5 cycles. All these results can be summed up that RCSB & CESB have good potential for removal of heavy metal ions (particularly Cd^{2+} & Pb^{2+}) from an aqueous environment up to 99%.

Chapter 5: Simultaneous removal and sensing of heavy metal ions using plant-derived biosorbent.

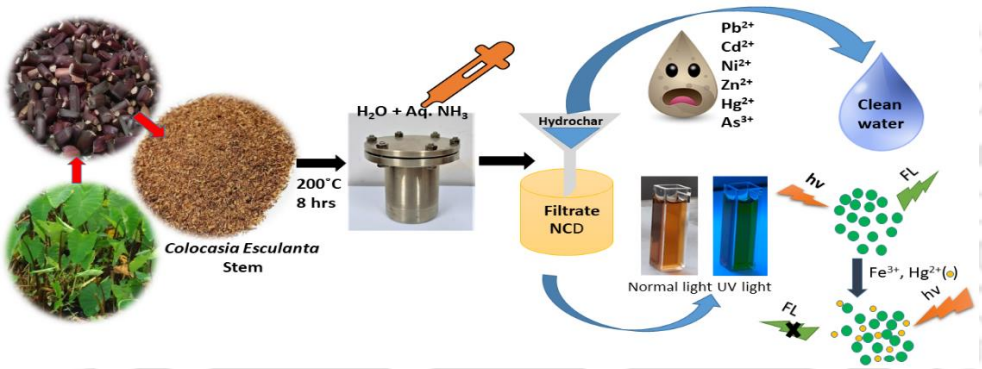

In this chapter, *Colocasia esculanta* stems (CES) has been chosen for simultaneous removal and sensing applications of heavy metals. Hydrochar generated in the hydrothermal treatment process is used for the adsorption of Pb^{2+} and Cd^{2+} ions. Various experimental parameters (pH, metal concentration, time, dosage and temperature) were studied to get the optimized result. The adsorption isotherm studies indicate that heavy metal ion biosorption follows the Freundlich isotherm. The adsorption kinetic model can be best described as pseudo-second-order, and the adsorption mechanism is physical adsorption. The optimum conditions for Cd^{2+} and lead Pb^{2+} by activated hydrochar were: adsorption time 120 minutes, temperature 20-25^{o}C, and pH between 6.8 and 7.2. The filtrate is taken for preparing carbon dots and heavy metal sensing applications. UV, transmission electron microscopy, atomic force microscope, Raman, FTIR, UV-Vis, and fluorescence spectroscopy characterized the synthesized carbon dots. The resulting carbon dots exhibit stable fluorescence with a quantum yield of 15.5%. The carbon dots emitted the fluorescence emission in 445nm wavelength and were used to detect Hg^{2+} and Fe^{3+} ions at the excitation of 370 nm. It has been found that Hg^{2+} and Fe^{3+} ions influence the fluorescence intensity

quenching of carbon dots stronger than other heavy metals, and detection can be achieved within 2 minutes. Hence *Colocasia esculanta* stem Simultaneous removal and sensing of heavy metal ions using plant-derived biosorbent

Conclusion and Future Scope

Plants are an abundant and renewable source of biomaterials that can be used for a variety of applications, including environmental remediation and nanotechnology. In conclusion, plant-derived biosorbents (Biochar and hydrochar) derived from *Ricinus communis* stem and *Colocasia esculanta* stem can be used for the removal of dyes and heavy metals, the synthesis of carbon nanoparticles, and the development of metal sensors. These sensors have shown promising results for the detection of a range of metals, including iron and mercury. This biochar has been synthesized at a comparatively lower temperature than previously reported. Cost analysis shows the synthesis process is economic. Further research is needed to optimize the biosorption process, improve the properties of carbon nanoparticles, and develop more sensitive metal sensors. Nevertheless, the potential of plant-derived materials for these applications makes them an attractive and sustainable alternative to conventional materials.

The future scope of plant-derived biosorbents for pollutant removal and carbon dot synthesis holds immense potential in various applications. With growing environmental concerns and the need for sustainable solutions, utilizing plant-based materials as biosorbents offers a renewable and eco-friendly approach to pollutant removal from water. These biosorbents, derived from plants such as agricultural waste, or other biomass sources, can effectively adsorb heavy metals, organic compounds, and even emerging pollutants. Additionally, plant-derived materials can be utilized in the synthesis of carbon dots, which are nanoparticles with unique optical and electronic properties. These carbon dots have applications in diverse fields, including bioimaging, sensing, drug delivery, and energy conversion. The combination of pollutant removal and carbon dot synthesis using plant-derived materials presents a promising avenue for creating sustainable and multifunctional solutions for environmental remediation and advanced technologies.

CONTENTS

Chapter 1: Introduction

Chapter 2: Experimental methods and Characterization

Chapter 5: **Hydrochar and N-CDs derived from Colocasia esculanta stem for effective removal and sensing of toxic metal ions.**

Chapter 1

Introduction

Chapter 2

Experimental Methods and Characterization

1. Introduction

1.1 Water pollution:

Water is the best gift from mother earth because of its importance for the viability of different flora and fauna on our planet [1.1]. As it is a limited natural resource, conserving its quality is of prime importance. But water quality decreases daily due to various anthropogenic activities, increasing industrialization, and unplanned urbanization. Water pollution caused by the discharge of dyes and heavy metals into water bodies is a growing concern due to its adverse impact on human health and aquatic life. Both dyes and heavy metals are commonly used in various industrial processes, including textile manufacturing, mining, and metal processing. Dyes are a significant contributor to water pollution as they are often released into water bodies during the dyeing process or disposal of wastewater. Many dyes contain toxic chemicals that can affect the quality of the water, making it unfit for consumption by humans and animals.

Moreover, dyes can reduce the amount of sunlight penetration, affecting aquatic plants' growth and an aqueous ecosystem's overall health. Heavy metals, such as lead, cadmium, and mercury, can also contribute to water pollution. They are released into the water through industrial discharge, mining activities, and agricultural runoff. These metals can accumulate in the food chain and pose significant health risks to humans and animals who consume contaminated water. Exposure to heavy metals can cause damage to the nervous system, kidneys, and liver and may even lead to cancer. Different types of organic(dyes) and inorganic pollutants (heavy metals) are significant pollutants in wastewater that disturb the aquatic environment [1.2,1.3]. Dyes are water-soluble complex organic compounds produced by dye industries, approximately 7×10^5 tonnes yearly [1.4]. The wastewater from these industries contains various hazardous dyes and heavy metals, which harm aquatic life [1.5].

Organic pollutants are synthetic dyes, pharmaceuticals, petroleum, and oil derived from crude and inorganic pollutants are heavy metal ions, nitrates, nitrites, phosphates, fluoride, and ammonium. Various industries such as textile, plastics, cosmetics, printing, carpet, food, leather, tannery, paper, mining, and minerals are the primary consumers of dyes and heavy metal ions used as a mordant [1.6–1.9]. These pollutants are released into water bodies such as lakes, ponds, rivers, seas, or soils, and untreated pollutants cause high chemical oxygen demand (COD), high coloring, and poor biochemical degradability of dyes and carcinogenic, mutagenic, teratogenic, toxic, and non-biodegradable heavy metals and attracted researchers for efficient and cost-effective treatment method [1.10]. Efforts to

address the water pollution caused by dyes and heavy metals include strict policy regulation, such as imposing influence discharge limits and using sustainable production policies. Different techniques have been used for the remediation of pollutants from polluted water, such as incineration, precipitation, coagulation, flocculation, membrane filtration, ion exchange, photochemical, electrochemical, biological, advanced oxidation process, adsorption, etc.[1.11].Out of all, adsorption is the most useful, valuable, and economical process.

1.2 Dyes as Pollutants

Dyes are colored complex organic compounds that are used to disperse color to paper, leather, hair, plastic, textile, drugs, foodstuffs, etc.Dyes exhibit color due to chromophores. Dyes are soluble in water and attach to fabric due to the presence of auxochrome in their structure [1.12]**.** Dyes have a complex molecular structure, are resistant to light and water oxidation, and are highly tough to degrade, causing harmful effects on human health, animals, and aquatic biota. Dyes released as effluents from different industries are shown in Table 1.1 [1.13]

Table 1.1 Different industries responsible for the presence of dye effluent in environment

Industry	**% of dye effluent**
Textile	54%
Dying	21%
Paper & Pulp	10%
Tannery & paint	8%
Dye manufactured	7%

The textile industry is the primary source of water pollution, and dye-bearing wastewater is unpleasant and undesirable as it contains non-biodegradable pollutants that are toxic to organisms [1.14]. Higher dye concentration causes various problems, such as water quality depletion, degraded vital water parameters, decreased dissolved oxygen, increased COD, and decreased water transparency. Therefore, it disturbs the growth of aquatic species. Dyes in the water body reduce the sunlight, disturbing the biological activity of marine species [1.15].

If dye concentration exceeds 2.0 mg kg^{-1}, ailments such as hemolytic anemia, abdominal and chest pain, hemolysis, high fever cyanosis, allergies, and breast cancer occur [1.16,1.17].

1.3 Dyes in the present study:

Two cationic dyes, viz., Malachite Green and Methylene Blue, were used in the current study, and their physicochemical properties are mentioned below.

1.3.1 Methylene Blue (MB):

Methylene Blue is a dark blue crystalline, odorless powder soluble in water, chloroform, and alcohol. In water, it gives dark blue color. It is used for dyeing fabrics, paper, and plastic. It is also used in pharmaceuticals, food processing, and tannery industries. It was initially synthesized in 1876 by Heinrich Caro and is also known as Tetramethylthionine chloride. It irritates the eyes, gastrointestinal tract and causes nausea, vomiting, and diarrhea [1.18].

Table 1.2 General characteristics of methylene blue and malachite green. [1.19]

Dye	Malachite Green (MG)	Methylene Blue (MB)
Molecular structure	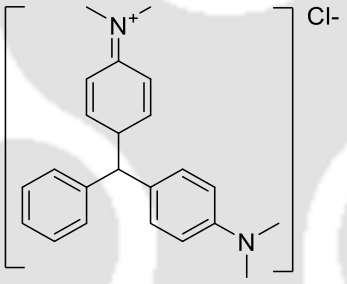	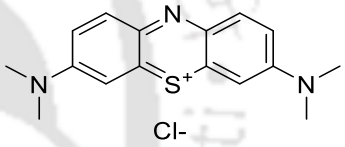
Class	Cationic N-methylated diamino triphenyl methane	Cationic thiazine dye
Chemical formula	$C_{23}H_{25}ClN_2$	$C_{16}H_{18}N_3SCl$
Mol. Weight (g/mol)	364.9	319.85
Colour Index name	Basic green 4 (BG 4)	Basic Blue 9 (BG 9)
Colour Index number	42,000	52,015
λ_{max} (nm)	619	664

1.3.2 Malachite green (MG):

Malachite green is a synthetic dye used for various purposes, including as a dye for silk and wool and as an antifungal agent in fish farming. However, it was banned in many countries due to its toxic properties and potential health risks. Its structures and other properties are shown in Table 1.2. The use of malachite green has been linked to various health problems in humans and animals, including

cancer, genetic mutations, and developmental abnormalities. It can also adversely affect the environment, particularly in aquatic ecosystems, where it can accumulate in the food chain and cause harm to fish and other marine organisms. Various health problems associated with the use of MG include a reduction in red blood cell (RBC) count (dyscrasia) and enhanced white blood cell count (leukocytosis), haemoglobin (anemia), and interruption of blood coagulation, eye blisters . MG is also implicated in the impairment of the kidney, liver, spleen, and heart and the infliction of lacerations on the skin, eyes, lungs, and bones. Therefore, there is an urgent need for the adaptation of eco-friendly approaches for the treatment of MG effluents before their release into water bodies and streams to safeguard the ecosystem

1.4 Heavy metal ions as a pollutant

The term "heavy metals" was given in 1817 AD by German chemist Leopold Gmelin . He divided the elements into non-metals, light metals, and heavy metals based on their densities. Light metals had densities of 0.860-5.0 g/cm^3, and heavy metals with densities greater than 5 g/cm^3-22.00g/cm^3; however, it depends less on density properties than chemical properties [1.20]. Heavy metals include arsenic (As), copper (Cu), cobalt (Co), zinc (Zn), lead (Pb), chromium (Cr), mercury (Hg), iron (Fe), cadmium (Cd), tin (Sn) and aluminum (Al). Metals like Sn and Al are grouped as less toxic heavy metals. Certain heavy metals, such as Mn, Cu, Ni, Fe, Zn, and Co are required in low concentrations for the basic life cycle occurring in living organisms. However, these become highly harmful and mutagen at higher concentrations. Whereas certain heavy metals, namely Cr, Hg, As, Pb, and Cd, have no role in biological processes, even minute amounts of these are toxic to living components, and these are classified as non-essential heavy metals[1.21] as shown in figure 1.1

Figure 1.1 Essential and non-essential heavy metals

Various sources of heavy metals include effluents from industries viz., metallurgical, textile, printing, electroplating, leather, and other metal processing industries and also include soil erosion, mining activity, motor vehicle emission, landfill leaches, lead-acid batteries, municipal water, and paint industries[1.22,1.23]. Heavy metals such as arsenic, lead, cadmium, chromium, nickel, etc., cause harmful effects on flora, fauna, and humans because they are toxic and non-biodegradable even at low concentrations [1.24]. Diseases and source of various heavy metals are shown in table 1.3.

Table 1.3 Diseases and Source of various heavy metals

HEAVY METALS	DISEASES	SOURCE(S)
Mercury	Minamata	Industrial waste, mining, chlor alkali process, Pesticide.
Cadmium	Itai-Itai	Metal plating, mining waste.
Arsenic	Black-Foot	Chemical waste, pesticides.
Lead	Plumbusis	Plumbing, gasoline, water pipes.
Nickel	Nickel itch	Nickel-cadmium batteries, electroplating, metal Processing.
Chromium (VI)	Cancer, skin ulceration	Electroplating, electronic equipment, steel production, textile industry

1.5 Wastewater treatment methods:

Wastewater treatment methods are essential for removing pollutants and contaminants from wastewater before it is discharged back back into the environment or reused. These methods typically involve a combination of chemical, physical, and biological processes.These wastewater treatment methods are shown in table 1.4

Table 1.4 Wastewater treatment methods [1.26]

Wastewater treatment methods	Chemical Treatment methods	Chemical oxidation Chemical precipitation Oxidation Coagulation Electrochemical oxidation Floatation Hydrolysis Ion Exchange
	Physical treatment methods	Adsorption Filtration Distillation Oil/water separation Sedimentation Membrane technologies
	Biological treatment methods	Rotating biological contactors Bioaugmentation Activated sludge Anaerobic processes Extended aeration Bioogical nitrogen removal

1.5.1 Adsorption for wastewater treatment

Adsorption occurs when the molecule or particles, known as the adsorbate, are attracted to the surface of a solid material, known as adsorbent, through various intermolecular forces, such as van der Waals forces, hydrogen bonding, or electrostatic interaction. Adsorption is due to the unsaturated and unbalanced molecular forces on every solid surface. When a solid surface comes near a liquid or gas, there is a reaction between the surface and that of the liquid or the gas. The solid surface tends to be in equilibrium with these residual forces by attracting and retaining its surface on the gas or liquid. This results in a greater concentration of the gas or liquid near the solid surface than in the bulk gas or vapor phase, despite the nature of the gas or vapor. Among various wastewater treatment methods, adsorption is the best and most effective because it is well established and powerful technique for treating domestic and industrial effluents. Various advantages of adsorption methods are mentioned in Fig. 1.2. Adsorption is widely used for dye and heavy metal removal and is broadly applicable in wastewater treatment.

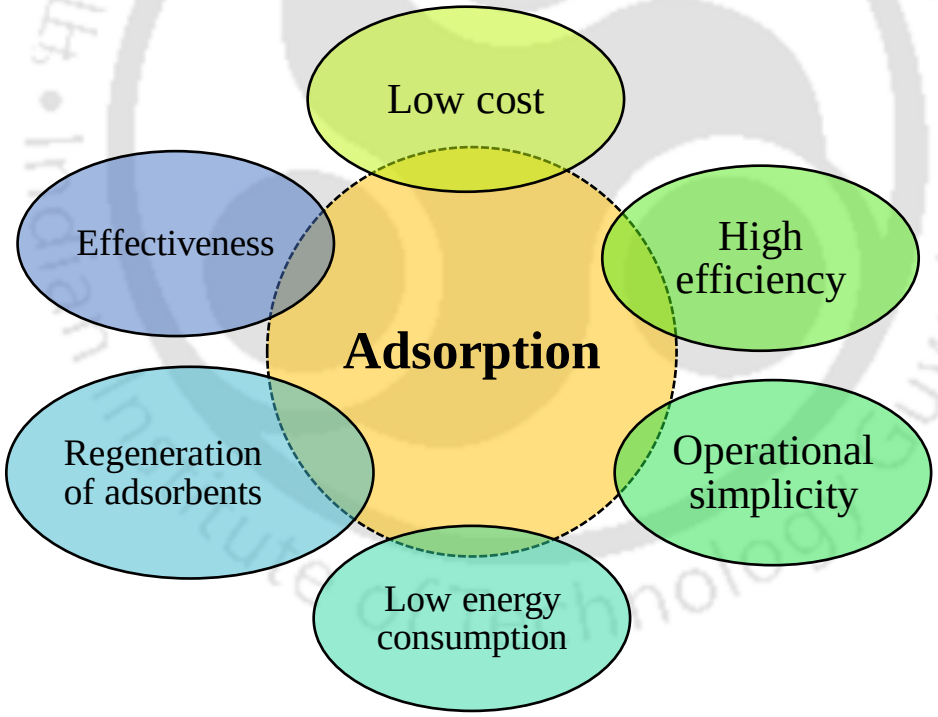

Figure 1.2 Various advantages of adsorption.

1.5.2 Types of adsorption:

Adsorption can be categorized into two types:

1) Physical adsorption (Physisorption) 2) Chemical adsorption (Chemisorption)

1.5.2.1 Physical adsorption

Physical adsorption, also known as physisorption or van der Waals adsorption, is a type of adsorption in which the adsorbate molecule or particles are attracted to the surface of the adsorbent through weak van der Waals forces, such as London dispersion forces or dipole-dipole interactions. These forces are generally weaker than chemical bonds and are reversible, meaning that adsorbate can easily desorb from the surface of the adsorbent[1.27]; Interactions between polar and non-polar molecules in which dipole moments are induced represent one class of physical adsorption. The heat evolved in physical adsorption is usually less than 20 kJ mol^{-1}.

1.5.2.2 Chemical adsorption

Chemisorption is a type of adsorption that involves a chemical reaction between the adsorbate and adsorbent surface. In chemisorption, the adsorbate forms a chemical bond with the surface of the adsorbent, resulting in a solid and irreversible attachment. The chemisorption process involves the activation of the adsorbent surface, usually by exposure to high temperatures or by treatment with chemicals that can create active sites on the surface [1.28]. The adsorbate molecules must have a certain energy level to break their chemical bonds and react with the surface. In chemisorption, strong, attractive forces form new bonds between the adsorbate and active centers of the adsorbent. It is either exothermic or endothermic, and the extent of the adsorption may decrease or increase with the temperature rise. The heat of adsorption, in this case, is in the order of 20-100 $Kcalmol^{-1}$.

1.6 Classification of Adsorbent:

(1) Synthetic adsorbent: Various porous adsorbents were synthesized with high adsorption capacities, but the manufacturing is comparatively costly. For example activated carbon, zeolites, or polymer resins.

(2) Natural adsorbent: Natural materials, i.e., plant root, leaf, and agricultural waste, are dried, crushed, sieved, washed with distilled water, and used as adsorbent to treat natural and synthetic dye/metal solutions. This process is cheap, but the adsorption capacity is comparatively low. Some examples are: charcoal, clays, clay minerals, dry plants, red mud, rice husk, sawdust etc.

(3) Semi-synthetic adsorbent: These types of materials are partially derived from the natural sources but have been chemically modified or processed to enhance their adsorption properties. The significant advantages of this adsorbent include low cost, high efficiency, minimization of chemical or biological sludge, no additional nutrient requirement, and regeneration of absorbent with the possibility of metal recovery. These materilas combine the benefits of natural materials with the tunabliity and improved performance achieved through synthetic modification. Here are a few examples of semi-synthetic adsorbents: Activated alumina, activated carbon from natural precursors, modified clays, modified chitosan, modified cellulose etc.

1.7 Plant-based adsorbent:

Plant-based adsorbents are natural materials derived from plants that have been used for centuries for various purposes. These materials are attractive as adsorbents due to their abundance, natural affinity, low cost, biodegradability, and sustainability. They can remove pollutants from aqueous solutions, including dyes, heavy metals, and organic compounds.

Plant-based adsorbents can be obtained from various parts of plants, including agricultural waste, leaves, stems, roots, and bark. They contain a variety of functional groups, such as carboxyl, hydroxyl, and amino groups, that enable them to interact with different types of pollutants [1.29]. These materials are rich in natural adsorbent compounds, such as lignin and cellulose, which can be extracted and processed to create effective adsorbent materials. The adsorption capacity of these materials can be enhanced by modification techniques such as chemical treatment, physical activation, and incorporation into composite materials [1.30]. Plant-based adsorbents have several advantages over conventional adsorbents, such as activated carbon. They are renewable, biodegradable, and have low toxicity. Moreover, they are locally sourced, making them suitable for use in developing countries where access to clean water is a significant challenge.

Plant-based adsorbents have been extensively studied for their potential applications in water treatment, environmental remediation, and wastewater treatment. They have also been explored as potential adsorbents for pharmaceuticals, food additives, and other industrial pollutants. Research in this area is ongoing, and there is growing interest in developing new plant-based adsorbents and optimizing experimental parameters.

1.8 Classification of Industrial Adsorbents:

Industrial adsorbents are classified into three types according to their constitution:

(1) Oxygen-containing adsorbent: contains compounds typically hydrophilic and polar, including materials such as silica gel and zeolites.

(2) Carbon-based adsorbent based compounds are typically hydrophobic and non-polar, including materials such as activated carbon and graphite

(3) Polymer-based adsorbent: Based compounds are polar or non-polar functional groups in a porous polymer matrix [1.31]

1.9 Introduction to carbon dots or carbon nanoparticles:

Carbon is one of the most abundant elements on earth after oxygen, comprising the basic building block of all living things. Carbon and its compounds play a significant role in today's world, making it the most widely studied element according to the Web of Science database [1.33]. Detailed research on nanostructures led to the discovery of carbon-based nanomaterials with the notable advent of the zero-dimensional fullerene first reported by Smalley, Kroto, Curl et al. in 1985 at Rice University and University of Sussex [1.34], followed by the discovery of other two allotropes, carbon nanotubes (CNTs) and graphene in 1991 and 2004 respectively [1.35,1.36] which added a new dimension to the field of nanotechnology and thus started the era of carbon nanomaterials. Since the finding of carbon nanomaterials, its family has been growing with the addition of new members from time to time, as shown in Figure 1.4. Carbon nanomaterials have acted as the prime focus of nanotechnology-based research in the last two and half decades, which is well noticeable from the Nobel Prize awarded in Chemistry (fullerenes), 1996, Kavli Prize in Nanoscience (carbon nanotubes) 2008 and the Nobel Prize in Physics (graphene) 2010, thereby highlighting the prospective class of materials in the field of modern material science research [1.37]. Various carbon allotropes are shown in table 1.5

Table 1.5 Different carbon allotropes

	Carbon allotropes
Zero dimensional	Fullerene, Nano-diamond, Graphene dots, Onion-like carbon, Carbon dots
One dimensional	Single-walled Carbon Nanotube, Multi-walled Carbon Nanotube, Carbon Nanohorns

Two-dimensional	Graphene, Carbon Nano Ribbon-unzipped Carbon nanotubes
Three dimensional	Multilayered Graphitic Sheets, Diamonds, Carbon Nanotubes Network

1.9.1 Plant-derived Carbon dots (CD)

Plant-based carbon dots are a type of carbon nanomaterials that are derived from natural plant sources. These tiny particles are typically less than 10 nanometers in size and are composed of other elements, such as oxygen and nitrogen. Carbon dots have many unique properties that make them attractive for various applications. They are biocompatible, non-toxic, and biodegradable, making them ideal for biomedical applications such as drug delivery and bioimaging. They also have excellent fluorescence properties, which make them useful in sensing and imaging applications. Recently, much recognition has been given to the green synthesis of carbon dots and its application. Carbon dots are novel fluorescent carbon nanomaterials and the most important members of the carbon nanomaterials family. Carbon dots generally are well-dispersed spherical particles with particle sizes less than 10 nm. First discovered by Xu et al. in 2004 [1.38] and subsequently named by Sun et al. in 2006 [1.39], Natural products are potent carbon precursors to synthesizing carbon dots with interesting chemical and physical properties like good biocompatibility, low cytotoxicity, facile synthesis, unique optical properties, low-cost, eco-friendly, large functional groups (amino, hydroxyl, carboxyl) and inexpensive precursors [1.40]. Hence, C-dots have been extensively used in many fields, such as cell imaging [1.41,1.42], in vivo imaging [1.43,1.44], drug delivery[1.45,1.46], fluorescence sensing[1.47–1.49], photocatalysis [1.49–1.51], multicolor light-emitting diode (LED) production [1.52,1.53], energy conversion and storage [1.54–1.56], etc. C-dots comprise carbon, hydrogen, oxygen, and nitrogen; their quantity depends on the synthesis method and precursors [1.57]. Carbon dots are abundant with -OH and -COOH functional groups, forming hydrogen bonds with water and showing excellent water solubility. Carbon dots have extraordinary optical properties, for example, strong fluorescence, long fluorescence time, photostability, broad excitation spectrum, and narrow emission spectrum. All these properties make carbon dots unique from commonly used organic or inorganic fluorophores [1.58–1.60]. Amongs the carbon dots properties, their fluorescence emissions and optical properties have gained more research interest in recent years [1.61]. CD are categorized into three types: raw CD, passivated CD, and functionalized CD [1.60]

1.9.2 Top-down and bottom-up methods for carbon dots synthesis

Top-down and bottom-up methods are two commonly used approaches for the synthesis of carbon dots(CDs). In top -down method, larger carbonaceous materials, such as graphite or carbon nanotubes, are broken down into smaller particles or structures which are then further processed to obtain CDs. This method involves processes like laser ablation, electrochemical exfoliation, or chemical oxidation, which can produce CDs with controlled sizes and properties. However, it often requires complex and energy-intensive procedures.

On the otherhand , the bottom-up method involves building CDs from smaller molecular precursors or starting materials. This approach typically involves chemical reactions, such as hydrothermal synthesis, solvothermal methods, or microwave-assisted synthesis, which enable the controlled growth of CDs with precise size and surface functionalization. The bottom-up method offers better control over the composition, size, and surface properties of CDs. It also allows for the incorporation of various functional groups, doping agents, or heteroatoms into the CD structure, leading to enhanced properties and tailored applications [1.62]. Hydrothermal or solvothermal is an eco-friendly, non-toxic, cost-effective, one-step synthesis process where carbonization of organic molecules occurs in the presence of water in a hydrothermal autoclave at high temperature and pressure. The hydrothermal method controls the size and quantum yield of carbon dots. Carbon-based quantum dots are synthesized from various organic molecules such as glucose, citric acid, amino acid, protein, carbohydrates, chitosan, or natural resource and bio-waste materials [1.63–1.67]. Hydrochar is a type of solid material that is produced through the process of hydrothermal carbonization(HTC) [1.68]. This process involves heating biomass, such as agricultural waste or other organic matter, in water under high pressure and temperature.

Both top-down and bottom-up methods have their advantages and limitations, and the choice of method depends on the desired CD properties and the specific application requirements.

1.10 Optical properties of carbon dots

1.10.1 Absorption

Carbon dots show strong absorption in the UV region with a stretching tail in the visible range. Some peaks in between 250-390 nm range due to the electronic transition of π-π^* of the C=C bond of the benzene ring [1.69,1.70]

1.10.2 Photoluminescence

The attractive characteristics of Carbon dots (CDs) are their strong and tunable photoluminescence[1.71]. It is the emission of light from an excited photon from a higher electronic state to a lower electronic form. CDs PL is a property that is photo-induced emission are led by excitation wavelength, particle size, different degrees of π conjugation, nature of doping atoms, surface passivation agent, and pH of solvent [1.72–1.75]. Depending on the excitation wavelength, carbon dots emit different fluorescence, like green, blue, cyan, orange, red, and yellow.

1.11 Application of Carbon Dots

Carbon dots (CDs) are a class of nanoparticles composed of carbon atoms that are small in size, typically less than 10 nm in diameter, and possess unique physiochemical properties. Due to their fascinating optical, electronic, and surface properties, carbon dots have gained significant attention in various fields. Some potential applications of carbon dots are mentioned below and shown in Figure 1.3

(i) Bioimaging: Carbon dots can be used as an imaging agent due to their fluorescence properties. They can be used for detecting and imaging cells, tissues, and organs.

(ii) Sensors: Carbon dots can be used as sensors for the detection of various analytes, such as heavy metals, toxins, and pH. They can also detect biomolecules such as glucose, proteins, and DNA.

(iii) Optoelectronics: Carbon dots have potential applications in optoelectronics due to their excellent electrical and optical properties. They can be used in light-emitting diodes (LEDs), solar cells, and field-effect transistors (FETs).

(iv) Drug delivery: Carbon dots can be used for drug delivery due to their small size, biocompatibility, and ability to penetrate cell membranes. They can be used to deliver drugs to specific cells or tissues.

(v) Catalysis: Carbon dots can be used as catalysts in various chemical reactions. They can be used in photocatalysis, electrocatalysis, and enzymatic catalysis.

(vi) Environmental applications: Carbon dots can be used in environmental applications such as water purification and air pollution control. They can be used to remove pollutants from water and air due to their ability to absorb heavy metals and organic compounds.

Carbon dots have tremendous potential in various fields due to their unique properties and ease of synthesis.

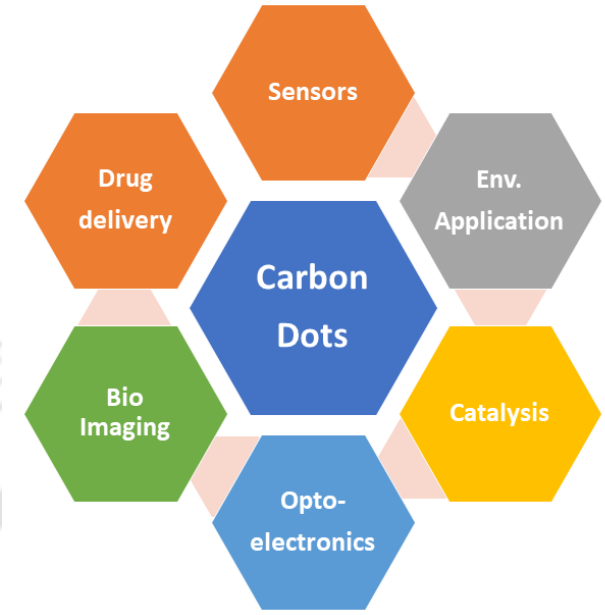

Fig. 1.3 Application of carbon dots in different fields

1.12 Conclusion and Outlook

Plant-derived materials , also known as bio-mass derived materials, are materials that are synthesized from natural sources such as plants, including their leaves, stems, seeds, and fibres. These materials offer numerous advantages over synthetic counterparts, including their renewability, biodegradability, and low environmental impact. Plant-derived biochar , a form of charcoal produced from biomass , has gained significant attention as a promising material for various applications. Biochar production involves the pyrolysis or carbonization of biomass materials,such as agricultural residue, wood waste. The process occurs under limited conditions, resulting in the conversion of organic matter into a stable carbon-rich material. The choice of biomass feedstock and pyrolysis can influence the property of the biochar. The properties of plant-derived biochar are influenced by factors such as feedstock type, pyrolysis temperature, residence time, and post-treatment processes. Biochar typically possesses a high carbon content, low ash content, and a porous structure with a large surface area. The surface area and pore structure of biochar play a crucial role in its potential applications.

Hydrochar, a carbonaceous material produced through hydrothermal carbonization (HTC) of biomass, has gained attention for its potential applications in water treatment, particularly for dye and heavy metal removal, as well as in the development of carbon dots.

These biosorbents have demonstrated promising results in high removal efficiency, low cost, and eco-friendliness. Additionally, synthesizing carbon dots using plant extracts has created new possibilities for novel materials with unique properties and applications.Plant-based biosorbents provide an efficient and sustainable solution to water pollution and create value-added products such as carbon dots through waste materials. As a new class of nanomaterials, carbon dots have shown great potential in various fields, such as bioimaging, sensors, optoelectronics,

The attention towards biochar, hydrochar for dye and heavy metal removal, as well as the development of carbon dots for water treatment which offers several advantages such as sustainability, cost-effectiveness, versatility,Environmental remediation. Further research and development in these areas can lead to advancements in water treatment technologies, providing efficient and sustainable solutions for pollutant removal and water purification.

1.13 Thesis objectives

The objectives of this thesis work are broadly classified into two primary goals:

- Plant-derived biosorbent for removal of dyes and heavy metals by optimization of various experimental parameters (adsorbent dosages, pH, concentrations of pollutants, contact time, and temperature)
- Synthesis and characterization of hydrochar and carbon nanoparticles and their use in heavy metal ion sensing applications.

Objective 1:

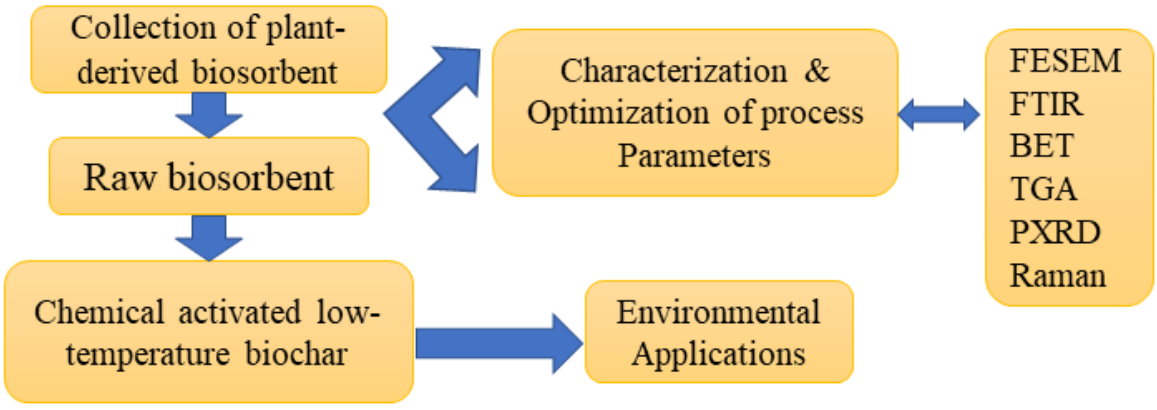

Objective 2

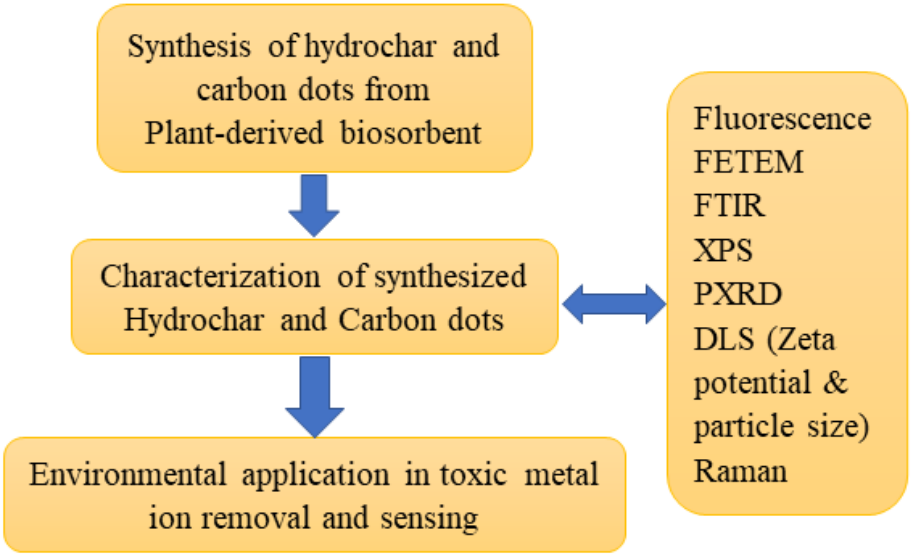

Reference

[1.1] A.M. Elgarahy, K.Z. Elwakeel, S.H. Mohammad, G.A. Elshoubaky, A critical review of biosorption of dyes, heavy metals and metalloids from wastewater as an efficient and green process, Cleaner Engineering and Technology. 4 (2021) 100209. https://doi.org/10.1016/J.CLET.2021.100209.

[1.2] A.G. Varghese, S.A. Paul, M.S. Latha, Remediation of heavy metals and dyes from wastewater using cellulose-based adsorbents, Environmental Chemistry Letters. 17 (2019) 867–877.

[1.3] A. Saravanan, P.S. Kumar, M. Govarthanan, C.S. George, S. Vaishnavi, B. Moulishwaran, S.P. Kumar, S. Jeevanantham, P.R. Yaashikaa, Adsorption characteristics of magnetic nanoparticles coated mixed fungal biomass for toxic Cr (VI) ions in an aquatic environment, Chemosphere. 267 (2021) 129226.

[1.4] B.N. Shelke, M.K. Jopale, A.H. Kategaonkar, Exploration of biomass waste as low-cost adsorbents for removal of methylene blue dye: A review, Journal of the Indian Chemical Society. 99 (2022) 100530. https://doi.org/10.1016/j.jics.2022.100530.

[1.5] K.A. Adegoke, O.S. Bello, Dye sequestration using agricultural wastes as adsorbents, Water Resources, and Industry. 12 (2015) 8–24. https://doi.org/10.1016/j.wri.2015.09.002.

[1.6] A. Jahanban-Esfahlan, R. Jahanban-Esfahlan, M. Tabibiazar, L. Roufegarinejad, R. Amarowicz, Recent advances in the use of walnut (Juglans regia L.) shell as a valuable plant-based bio-sorbent for the removal of hazardous materials, RSC Adv. 10 (2020) 7026–7047. https://doi.org/10.1039/C9RA10084A.

[1.7] H. Medhi, P.R. Chowdhury, P.D. Baruah, K.G. Bhattacharyya, Kinetics of Aqueous Cu(II) Biosorption onto Thevetia peruviana Leaf Powder, ACS Omega. 5 (2020) 13489–13502. https://doi.org/10.1021/acsomega.9b04032.

[1.8] A. Sintakindi, B. Ankamwar, Uptake of Methylene Blue from Aqueous Solution by Naturally Grown Daedalea africana and Phellinus adamantinus Fungi, Cite This: ACS Omega. 5 (2020) 12905–12914. https://doi.org/10.1021/acsomega.0c00673.

[1.9] K.G. Akpomie, J. Conradie, Efficient synthesis of magnetic nanoparticle-Musa acuminata peel composite for the adsorption of anionic dye, Arabian Journal of Chemistry. 13 (2020) 7115–7131. https://doi.org/10.1016/J.ARABJC.2020.07.017.

[1.10] D. Sachan, A. Ghosh, G. Das, Valorization of aquatic weed Salvinia minima to value-added eco-friendly biosorbent: preferential removal of dye and heavy metal, International Journal of Environmental Science and Technology. (2022). https://doi.org/10.1007/s13762-022-04126-7.

[1.11] S. Kumari, A.A. Khan, A. Chowdhury, A.K. Bhakta, Z. Mekhalif, S. Hussain, Efficient and highly selective adsorption of cationic dyes and removal of ciprofloxacin antibiotic by surface modified nickel sulfide nanomaterials: Kinetics, isotherm and adsorption mechanism, Colloids and Surfaces A: Physicochemical and Engineering Aspects. 586 (2020) 124264. https://doi.org/10.1016/J.COLSURFA.2019.124264.

[1.12] W.Z. Tang, Huren An, UV/TiO2 photocatalytic oxidation of commercial dyes in aqueous solutions, Chemosphere. 31 (1995) 4157–4170. https://doi.org/10.1016/0045-6535(95)80015-D.

[1.13] V. Katheresan, J. Kansedo, S.Y. Lau, Efficiency of various recent wastewater dye removal methods: A review, Journal of Environmental Chemical Engineering. 6 (2018) 4676–4697. https://doi.org/10.1016/J.JECE.2018.06.060.

[1.14] A.B. Albadarin, C. Mangwandi, Mechanisms of Alizarin Red S and Methylene blue biosorption onto olive stone by-product: isotherm study in single and binary systems, Journal of Environmental Management. 164 (2015) 86–93.

[1.15] C. Zaharia, D. Suteu, A. Muresan, R. Muresan, A. Popescu, others, Textile wastewater treatment by homogenous oxidation with hydrogen peroxide, Environmental Engineering, and Management Journal. 8 (2009) 1359–1369.

[1.16] N. Mahmoodi-Babolan, A. Heydari, A. Nematollahzadeh, Removal of methylene blue via bioinspired catecholamine/starch superabsorbent and the efficiency prediction by response surface methodology and artificial neural network-particle swarm optimization, Bioresource Technology. 294 (2019) 122084.

[1.17] L.R. Bonetto, J.S. Crespo, R. Guégan, V.I. Esteves, M. Giovanela, Removal of methylene blue from aqueous solutions using a solid residue of the apple juice industry: Full factorial design, equilibrium, thermodynamics, and kinetics aspects, Journal of Molecular Structure. 1224 (2021) 129296.

[1.18] J. Zolgharnein, M. Bagtash, T. Shariatmanesh, Simultaneous removal of a binary mixture of Brilliant Green and Crystal Violet using derivative spectrophotometric determination, multivariate optimization and adsorption characterization of dyes on surfactant modified nano-$γ$-alumina, Spectrochimica Acta Part A: Molecular and Biomolecular Spectroscopy. 137 (2015) 1016–1028.

[1.19] S. Rangabhashiyam, S. Lata, P. Balasubramanian, Biosorption characteristics of methylene blue and malachite green from simulated wastewater onto Carica papaya wood biosorbent, Surfaces, and Interfaces. 10 (2018) 197–215. https://doi.org/10.1016/j.surfin.2017.09.011.

[1.20] S.J. Hawkes, What Is a “Heavy Metal”?, Journal of Chemical Education. 74 (1997) 1374. https://doi.org/10.1021/ed074p1374.

[1.21] D. Bagal-Kestwal, M.S. Karve, B. Kakade, V.K. Pillai, Invertase inhibition based electrochemical sensor for the detection of heavy metal ions in the aqueous system: Application of ultra-microelectrode to enhance sucrose biosensor’s sensitivity, Biosensors, and Bioelectronics. 24 (2008) 657–664. https://doi.org/10.1016/J.BIOS.2008.06.027.

[1.22] J.O. Nriagu, A global assessment of natural sources of atmospheric trace metals, Nature. 338 (1989)

47–49.
[1.23] L.S. Thakur, M. Parmar, Adsorption of heavy metal (Cu2+, Ni2+, and Zn2+) from synthetic wastewater by tea waste adsorbent, International Journal of Chemical and Physical Sciences. 2 (2013) 6–19.
[1.24] P. Trivedi, L. Axe, Modeling Cd and Zn sorption to hydrous metal oxides, Environmental Science \& Technology. 34 (2000) 2215–2223.
[1.25] N. Kataria, V.K. Garg, M. Jain, K. Kadirvelu, Preparation, characterization and potential use of flower shaped Zinc oxide nanoparticles (ZON) for the adsorption of Victoria Blue B dye from aqueous solution, Advanced Powder Technology. 27 (2016) 1180–1188.
[1.26] N.B. Singh, G. Nagpal, S. Agrawal, Rachna, Water purification by using Adsorbents: A Review, Environmental Technology & Innovation. 11 (2018) 187–240. https://doi.org/10.1016/J.ETI.2018.05.006.
[1.27] N. Lal, A.K. Srivastava, Decolorization of malachite green by newly isolated Bacillus strain MTCC-3330, Archives of Environmental Science. 5 (2011) 71–76.
[1.28] A. Gil, Classical and new insights into the methodology for characterizing adsorbents and metal catalysts by chemical adsorption, Catalysis Today. (2023).
[1.29] A. Saravanan, P.S. Kumar, R. V Hemavathy, S. Jeevanantham, M.J. Jawahar, J.P. Neshaanthini, R. Saravanan, A review on synthesis methods and recent applications of nanomaterial in wastewater treatment: Challenges and future perspectives, Chemosphere. (2022) 135713.
[1.30] K. Azam, N. Shezad, I. Shafiq, P. Akhter, F. Akhtar, F. Jamil, S. Shafique, Y.-K. Park, M. Hussain, A review on activated carbon modifications for treating wastewater containing anionic dyes, Chemosphere. (2022) 135566.
[1.31] S. V, N.D. CH, S.B. G, R.T. Y, Role of Biosorption in Environmental Cleanup, Journal of Microbial & Biochemical Technology. 3 (2011) 1–8. https://doi.org/10.4172/1948-5948.r1-001.
[1.32] D.C. Kalyani, A.A. Telke, R.S. Dhanve, J.P. Jadhav, Ecofriendly biodegradation and detoxification of Reactive Red 2 textile dye by newly isolated Pseudomonas sp. SUK1, Journal of Hazardous Materials. 163 (2009) 735–742.
[1.33] O. Kozák, M. Sudolská, G. Pramanik, P. Cígler, M. Otyepka, R. Zbořil, Photoluminescent Carbon Nanostructures, Chemistry of Materials. 28 (2016) 4085–4128. https://doi.org/10.1021/acs.chemmater.6b01372.
[1.34] H.W. Kroto, J.R. Heath, S.C. O'Brien, R.F. Curl, R.E. Smalley, C 60: buckminsterfullerene, Nature. 318 (1985) 162–163.
[1.35] S. Iijima, Helical microtubules of graphitic carbon, Nature. 354 (1991) 56–58.
[1.36] K.S. Novoselov, A.K. Geim, S. V Morozov, D. Jiang, Y. Zhang, S. V Dubonos, I. V Grigorieva, A.A. Firsov, Electric field effect in atomically thin carbon films, Science. 306 (2004) 666–669.
[1.37] M.M. Titirici, R.J. White, N. Brun, V.L. Budarin, D.S. Su, F. Del Monte, J.H. Clark, M.J. MacLachlan, Sustainable carbon materials, Chemical Society Reviews. 44 (2015) 250–290. https://doi.org/10.1039/c4cs00232f.
[1.38] X. Xu, R. Ray, Y. Gu, H.J. Ploehn, L. Gearheart, K. Raker, W.A. Scrivens, Electrophoretic analysis and purification of fluorescent single-walled carbon nanotube fragments, Journal of the American Chemical Society. 126 (2004) 12736–12737. https://doi.org/10.1021/ja040082h.
[1.39] Y.P. Sun, B. Zhou, Y. Lin, W. Wang, K.A.S. Fernando, P. Pathak, M.J. Meziani, B.A. Harruff, X. Wang, H. Wang, P.G. Luo, H. Yang, M.E. Kose, B. Chen, L.M. Veca, S.Y. Xie, Quantum-sized carbon dots for bright and colorful photoluminescence, Journal of the American Chemical Society. 128 (2006)

7756–7757. https://doi.org/10.1021/ja062677d.

[1.40] C. Long, Z. Jiang, J. Shangguan, T. Qing, P. Zhang, B. Feng, Applications of carbon dots in environmental pollution control: A review, Chemical Engineering Journal. 406 (2021) 126848. https://doi.org/10.1016/j.cej.2020.126848.

[1.41] M. Zhang, R. Su, J. Zhong, L. Fei, W. Cai, Q. Guan, W. Li, N. Li, Y. Chen, L. Cai, others, Red/orange dual-emissive carbon dots for pH sensing and cell imaging, Nano Research. 12 (2019) 815–821.

[1.42] J. Liu, Y. Dong, Y. Ma, Y. Han, S. Ma, H. Chen, X. Chen, One-step synthesis of red/green dual-emissive carbon dots for ratiometric sensitive ONOO- probing and cell imaging, Nanoscale. 10 (2018) 13589–13598.

[1.43] K. Qin, D. Zhang, Y. Ding, X. Zheng, Y. Xiang, J. Hua, Q. Zhang, X. Ji, B. Li, Y. Wei, Applications of hydrothermal synthesis of Escherichia coli derived carbon dots in vitro and in vivo imaging and p-nitrophenol detection, Analyst. 145 (2020) 177–183.

[1.44] J. Liu, D. Li, K. Zhang, M. Yang, H. Sun, B. Yang, One-step hydrothermal synthesis of nitrogen-doped conjugated carbonized polymer dots with 31% efficient red emission for in vivo imaging, Small. 14 (2018) 1703919.

[1.45] Y. Shu, J. Lu, Q.-X. Mao, R.-S. Song, X.-Y. Wang, X.-W. Chen, J.-H. Wang, Ionic liquid mediated organophilic carbon dots for drug delivery and bioimaging, Carbon. 114 (2017) 324–333.

[1.46] S.K. Kailasa, J.R. Bhamore, J.R. Koduru, T.J. Park, Carbon dots as carriers for the development of controlled drug and gene delivery systems, Biomedical Applications of Nanoparticles. (2019) 295–317.

[1.47] J. Jana, H.J. Lee, J.S. Chung, M.H. Kim, S.H. Hur, Blue emitting nitrogen-doped carbon dots as a fluorescent probe for nitrite ion sensing and cell-imaging, Analytica Chimica Acta. 1079 (2019) 212–219.

[1.48] J. Wang, R.S. Li, H.Z. Zhang, N. Wang, Z. Zhang, C.Z. Huang, Highly fluorescent carbon dots as selective and visual probes for sensing copper ions in living cells via an electron transfer process, Biosensors, and Bioelectronics. 97 (2017) 157–163.

[1.49] J. Hu, F. Tang, Y.-Z. Jiang, C. Liu, Rapid screening and quantitative detection of Salmonella using a quantum dot nanobead-based biosensor, Analyst. 145 (2020) 2184–2190.

[1.50] M. Han, S. Zhu, S. Lu, Y. Song, T. Feng, S. Tao, J. Liu, B. Yang, Recent progress on the photocatalysis of carbon dots: Classification, mechanism and applications, Nano Today. 19 (2018) 201–218. https://doi.org/10.1016/J.NANTOD.2018.02.008.

[1.51] Y. Zhou, E.M. Zahran, B.A. Quiroga, J. Perez, K.J. Mintz, Z. Peng, P.Y. Liyanage, R.R. Pandey, C.C. Chusuei, R.M. Leblanc, Size-dependent photocatalytic activity of carbon dots with surface-state determined photoluminescence, Applied Catalysis B: Environmental. 248 (2019) 157–166.

[1.52] F. Yuan, T. Yuan, L. Sui, Z. Wang, Z. Xi, Y. Li, X. Li, L. Fan, Z. Tan, A. Chen, others, Engineering triangular carbon quantum dots with unprecedented narrow bandwidth emission for multicolored LEDs, Nature Communications. 9 (2018) 1–11.

[1.53] J. Zheng, X. Liu, Y. Yang, X. Liu, B. Xu, Rapid and green synthesis of fluorescent carbon dots from starch for white light-emitting diodes, New Carbon Materials. 33 (2018) 276–288.

[1.54] C. Hu, M. Li, J. Qiu, Y.-P. Sun, Design, and fabrication of carbon dots for energy conversion and storage, Chemical Society Reviews. 48 (2019) 2315–2337.

[1.55] K.A.S. Fernando, S. Sahu, Y. Liu, W.K. Lewis, E.A. Guliants, A. Jafariyan, P. Wang, C.E. Bunker, Y.-P. Sun, Carbon quantum dots and applications in photocatalytic energy conversion, ACS Applied Materials \& Interfaces. 7 (2015) 8363–8376.

[1.56] R. Genc, M.O. Alas, E. Harputlu, S. Repp, N. Kremer, M. Castellano, S.G. Colak, K. Ocakoglu, E. Erdem, High-capacitance hybrid supercapacitor based on multi-colored fluorescent carbon-dots, Scientific Reports. 7 (2017) 1–13.

[1.57] J. Peng, W. Gao, B.K. Gupta, Z. Liu, R. Romero-Aburto, L. Ge, L. Song, L.B. Alemany, X. Zhan, G. Gao, others, Graphene quantum dots derived from carbon fibers, Nano Letters. 12 (2012) 844–849.

[1.58] J.C.G.E. da Silva, H.M.R. Gonçalves, Analytical and bioanalytical applications of carbon dots, TrAC Trends in Analytical Chemistry. 30 (2011) 1327–1336.

[1.59] Y. Wang, A. Hu, Carbon quantum dots: synthesis, properties and applications, Journal of Materials Chemistry C: Materials for Optical and Electronic Devices. 2 (2014) 6921–6939. https://doi.org/10.1039/c4tc00988f.

[1.60] Z. Yang, Z. Li, M. Xu, Y. Ma, J. Zhang, Y. Su, F. Gao, H. Wei, L. Zhang, Controllable synthesis of fluorescent carbon dots and their detection application as nanoprobes, Nano-Micro Letters. 5 (2013) 247–259.

[1.61] Y. Zhao, X. Liu, Y. Yang, L. Kang, Z. Yang, W. Liu, L. Chen, Carbon Dots: From Intense Absorption in Visible Range to Excitation-Independent and Excitation-Dependent Photoluminescence, Fullerenes, Nanotubes and Carbon Nanostructures. 23 (2015) 922–929. https://doi.org/10.1080/1536383X.2015.1018413.

[1.62] C. Kang, Y. Huang, H. Yang, X.F. Yan, Z.P. Chen, A review of carbon dots produced from biomass wastes, Nanomaterials. 10 (2020) 1–24. https://doi.org/10.3390/nano10112316.

[1.63] Z.-C. Yang, M. Wang, A.M. Yong, S.Y. Wong, X.-H. Zhang, H. Tan, A.Y. Chang, X. Li, J. Wang, Intrinsically fluorescent carbon dots with tunable emission derived from hydrothermal treatment of glucose in the presence of monopotassium phosphate, Chemical Communications. 47 (2011) 11615–11617.

[1.64] Y. Yang, J. Cui, M. Zheng, C. Hu, S. Tan, Y. Xiao, Q. Yang, Y. Liu, One-step synthesis of amino-functionalized fluorescent carbon nanoparticles by hydrothermal carbonization of chitosan, Chemical Communications. 48 (2012) 380–382.

[1.65] Z. Zhang, J. Hao, J. Zhang, B. Zhang, J. Tang, Protein as the source for synthesizing fluorescent carbon dots by a one-pot hydrothermal route. Rsc Adv 2: 8599--8601, (2012).

[1.66] N. Wang, Y. Wang, T. Guo, T. Yang, M. Chen, J. Wang, Green preparation of carbon dots with papaya as carbon source for effective fluorescent sensing of Iron (III) and Escherichia coli, Biosensors and Bioelectronics. 85 (2016) 68–75.

[1.67] A. Kumar, A.R. Chowdhuri, D. Laha, T.K. Mahto, P. Karmakar, S.K. Sahu, Green synthesis of carbon dots from Ocimum sanctum for effective fluorescent sensing of Pb2+ ions and live cell imaging, Sensors and Actuators B: Chemical. 242 (2017) 679–686.

[1.68] M. Śliz, F. Tuci, K. Czerwińska, S. Fabrizi, L. Lombardi, M. Wilk, Hydrothermal carbonization of the wet fraction from mixed municipal solid waste: Hydrochar characteristics and energy balance, Waste Management. 151 (2022) 39–48.

[1.69] Z. Luo, Y. Lu, L.A. Somers, A.T.C. Johnson, High yield preparation of macroscopic graphene oxide membranes, Journal of the American Chemical Society. 131 (2009) 898–899.

[1.70] F. Yuan, S. Li, Z. Fan, X. Meng, L. Fan, S. Yang, Shining carbon dots: Synthesis and biomedical and optoelectronic applications, Nano Today. 11 (2016) 565–586.

[1.71] X. Zhao, A. Wang, S. Gao, D. Yan, W. Guo, Y. Xu, Y. Meng, C. Wang, G. Shan, Enhancing photoluminescence of carbon quantum dots doped PVA films with randomly dispersed silica

microspheres, Scientific Reports. 10 (2020) 1–10. https://doi.org/10.1038/s41598-020-62563-1.

[1.72] S. Zhu, J. Zhang, C. Qiao, S. Tang, Y. Li, W. Yuan, B. Li, L. Tian, F. Liu, R. Hu, others, Strongly green-photoluminescent graphene quantum dots for bioimaging applications, Chemical Communications. 47 (2011) 6858–6860.

[1.73] J. Shen, Y. Zhu, X. Yang, J. Zong, J. Zhang, C. Li, One-pot hydrothermal synthesis of graphene quantum dots surface-passivated by polyethylene glycol and their photoelectric conversion under near-infrared light, New Journal of Chemistry. 36 (2012) 97–101.

[1.74] Y. Li, Y. Hu, Y. Zhao, G. Shi, L. Deng, Y. Hou, L. Qu, An electrochemical avenue to green-luminescent graphene quantum dots as potential electron-acceptors for photovoltaics., Advanced Materials (Deerfield Beach, Fla.). 23 (2011) 776–780. https://doi.org/10.1002/adma.201003819.

[1.75] L. Tian, D. Ghosh, W. Chen, S. Pradhan, X. Chang, S. Chen, Nanosized carbon particles from natural gas soot, Chemistry of Materials. 21 (2009) 2803–2809.

The present chapter discusses detailed information on the raw material and chemicals used in synthesizing activated biochar and hydrochar from the stem of *Ricinus communis* and *Colocasia esculanta.* Both plants' stem has been used to synthesize activated biochar and its application in removing dyes and heavy metals from an aqueous environment. *Colocasia esculanta* stem has been used for synthesizing hydrochar using hydrothermal treatment, and filtrate of hydrothermal treatment was used for synthesizing carbon dots and its application in toxic metal ion sensing in actual water samples. The synthesis procedure and specification of instruments used to characterize raw, activated biochar, hydrochar, and nitrogen-doped carbon nanoparticles are discussed in this chapter. In addition, these plant-derived materials are also applied in various water purification and sensing applications and are presented in this chapter.

2.1 Materials and reagents :

2.1.1 Raw materials:

The matured stem of *Ricinus communis(RCS)* and *Colocasia esculanta(CES)* was collected locally from the premises of the Indian Institute of Technology Guwahati, North Guwahati, Assam, India (Location 26°11′14″N 91°41′30″E) campus during June month. The collected stems were cleaned and washed with double distilled water to remove the dirt particles present on the surface. The stems were cut into small pieces and dried under sunlight for three days. The wholly dried material was ground using a sieve (Heico, standard Indian sieve) to powdered form with 150-300µm particle size. Finally, the powdered material was dried in a hot air oven at 110˚C for 5 hours and kept in an airtight container for subsequent use. The raw dried stems were denoted as RCS, CES followed by activated biochar as RCSB, CESB, and hydrochar as RCSH and CESH.

2.1.2 Chemicals:

All the reagents and chemicals used in synthesizing plant-derived biosorbent materials were of analytical grade, used without further purification, and purchased from Merck Ltd. Himedia, SRL chemicals, and Loba chemie. Hydrochloric acid (HCl) and anhydrous sodium hydroxide (NaOH) were used for the pH adjustment of dyes and heavy metals. K_2CO_3 has been used for the activation of biochar. Malachite green (MG), methylene blue (MB), congo red (CR), crystal violet (CV), neutral Red (NR), safranin (SFR), eriochrome black T (EBT), acid blue 9 (AB9) and bromophenol blue (BPB) was used for the comparative dyes removal studies, and these were purchased from Loba chemicals. Prepared cadmium, lead, nickel, zinc, copper, mercury, arsenic, and chromium solutions were prepared from their chloride salts for toxic metal removal studies. pH was maintained by (1M) HCl and (1M) NaOH solutions in all the experiments. Carbon nanoparticles

were synthesized and used for the sensing application of Hg^{2+} and Fe^{3+}. Standard stock solutions (1mM) of metal ions (Ag^{+}, Cd^{2+}, Co^{2+}, Cu^{2+}, Fe^{3+}, Hg^{2+}, Mg^{2+}, Mn^{2+}, Na^{+}, Ni^{2+}, Pb^{2+}, Zn^{2+}, Al^{3+}, Cr^{3+}) were prepared with ultrapure water from the respective metal salts ($AgNO_3$, Cd $(NO_3)_2$, $CoCl_2.6H_2O$, $CuSO_4.5H_2O$, $FeCl_3$, $HgCl_2$, $MgSO_4$, $MnCl_2$, NaCl, $NiCl_2.6H_2O$, Pb $(NO_3)_2$, Zn $(CH_3COO)_2$, Al $(NO_3)_3$. All these salts were purchased from SRL Chemicals, Mumbai, India. Quinine sulfate dihydrate was obtained from Himedia, India.

2.2 Characterization and Analytical Methods:

Characterization of biosorbents is an essential step in understanding their physical, chemical, and structural properties. The following are some of the methods used for the characterization of biosorbents:

(i) Fourier-transform infrared spectroscopy (FTIR): This Instrument is used to identify the functional groups present in the biosorbent. FTIR spectra can provide information about the bonding nature of the biosorbent, including the presence of specific groups such as carboxylic, hydroxyl, and amino groups. Fourier-transformed infrared spectra (FTIR) using ATR (attenuated total reflection) mode were recorded on PerkinElmer Spectrum 2 FTIR spectrometer, 400 cm^{-1} - 4000 cm^{-1}

(ii) Field emission Scanning electron microscopy (FESEM): FESEM is used to visualize the surface morphology and microstructure of the biosorbent. It provides information on the size, shape, distribution, and presence of cracks, pores, and other surface features. FESEM, (Zeiss, Sigma 300) was used to obtain the surface morphology; Elemental confirmation was done by EDS (dispersive energy scattering) software available on the FESEM instrument.

(iii) X-ray diffraction (XRD): XRD is used to identify the crystal structure and composition of the biosorbent. It provides information on the degree of crystallinity, the crystallites' size, and the crystal plane's orientation. The powder X-ray diffraction pattern (PXRD) of dried biosorbent was studied in a Powder X-ray diffractometer (Rigaku, SmartLab) at a diffraction angle (2θ) ranging from 5° to 80° with 0.02° step size.

(iv) Brunauer, Emmett and Teller (BET) surface area analysis: This method is used to measure the surface area and porosity of the biosorbent. It provides information on the specific surface area, pore volume, and pore size distribution of the biosorbent. Surface area analyzer (Quantachrome, Autosorb-IQ MP) instrument.

(v) Thermogravimetric analysis (TGA): TGA is used to determine the thermal stability and decomposition behavior of the biosorbent. It provides information on the weight loss,

thermal degradation, and thermal stability of the biosorbent. Thermogravimetric measurement of the materials was analyzed on TGA analyzer Netzsch (STA449F3A00). Samples were heated from ambient temperature to 800°C at 10°C/min under nitrogen flow.

(vi) High-resolution transmission electron microscopic (HRTEM) images of carbon dots were acquired on HRTEM (JEOL 2100-F)

(vii) Dynamic light scattering : The synthesized CDs' zeta potential and particle size were measured using a particle size analyzer (Litesizer 500, Anton Paar).

(viii) Atomic absorption spectrometer: Experimental analysis of heavy metal adsorption was analyzed in Atomic absorption spectrophotometer, Varian AA240.

(ix) X ray photoelectron spectroscopy (XPS): X-ray photoelectron spectroscopy (XPS) of NCD was carried out to investigate the chemical state and elemental composition (Thermo Fisher Scientific Pvt. Ltd, UK, Model: ESCALAB Xi+).

(x) TRPL: The time-resolved photoluminescence (TRPL) spectra were recorded with a LifeSpec II Edinburgh instrument.

(xi) The Raman spectra were recorded in Laser Micro Raman System (Make: Horiba Jobin Vyon, Model: LabRam HR).

Carbon nanoparticles were synthesized using a hydrothermal reactor purchased from AntsLabs, India, and were applied to study toxic metal sensing applications..

2.3 Synthesis of raw and activated biochar (RCS, CES, RCSB & CESB) :

Ricinus communis (RCS) and *Colocasia esculanta(CES)* stems were collected from the Indian Institute of Technology, Guwahati. Stems were washed thoroughly with distilled water, cut into small pieces, and dried under sunlight for 3 to 4 days, followed by a hot air oven at 100°C for 12 h. The stem were crushed in a mixer grinder and then separated into different sizes using sieves of various sizes (500 µm, 300 µm, 150 µm, 50 µm, and 25 µm) and stored in an oven at 50˚C for further use. 150 µm sieved dried powdered biosorbent has been used for different experiments. This is the preparation method for raw RCS and CES. Both powdered biosorbents (RCS and CES) were impregnated in potassium carbonate (1 gm of stem powder with 30 ml of 0.6 mol.L^{-1} K_2CO_3) for 4 hrs and then heated in a muffle furnace at 300˚C for 6 hrs. After cooling to room temperature, the activated biochar mixture was washed with deionized water until the conductivity of the wash liquor was less than 10 $mScm^{-1}$. The activated biochar (RCSB and CESB) was dried in a hot air oven at 100˚C for 3 hrs and then stored in an airtight plastic container for further experiments.

2.4 Synthesis of hydrochar:

Biochar prepared by using the hydrothermal method is called hydrochar. Generally, hydrochar has a low surface area and porosity than pyrolytic biochar because of the rich oxygen-containing functional groups on its surface [2.1] [2.2]. Hydrochar has more adsorption capability than pyrolytic biochar [2.3], which makes hydrochar a suitable adsorbent in toxic metal removal. *Colocasia esculanta(CES)* stems collected from the Indian Institute of Technology, Guwahati. Stems were washed thoroughly with distilled water, cut into small pieces, and dried under sunlight for 3 to 4 days, followed by a hot air oven at 100°C for 12 h. The stem were crushed in a mixer grinder. *Colocasia esculanta* stem hydrochar (CESH) was prepared by hydrothermal carbonization. 5 gm of stem were dispersed in 60 mL distilled water with constant stirring. Then it was transferred to 100 mL stainless steel hydrothermal autoclave (HTC) reactors. The HTC reactor was placed in a high-temperature oven and heated to 200° C for 8 hrs. After 8 hrs, the HTC reactor was cooled down to room temperature, and the materials were separated by filtration. CESH was washed thoroughly with distilled water and oven-dried at 100° C for 18 hrs. Then dried CESH was stored in airtight containers for further characterization and application in adsorption studies. The prepared hydrochars were characterized in detail as described in supporting information. The following equation was used to calculate the hydrochar yield:

$$\text{Hydrochar yield (\%)} = \frac{\text{Hydrochar weight}}{\text{Raw material weight}} \times 100$$

2.5 Synthesis of N-doped carbon nanoparticles:

Carbon dots were synthesized by the hydrothermal method. 1 gm of Powdered *Colocasia esculanta* stem was transferred to a hydrothermal autoclave (Ant Ceramics, India) containing 40 ml H_2O , and 2 ml of aqueous ammonia and heated at 200 °C for 8 hours. Subsequently, the hydrothermal autoclave was allowed to cool down to room temperature. The dark brown colored suspension was cooled to room temperature naturally. The green fluorescence nitrogen-doped carbon dots solutions were harvested using a 0.22 μM membrane filter. Finally, the synthesized NCD solution was kept at 4°C for further analysis.

2.6 Experimental methods :

2.6.1 Dye adsorption study using raw and activated biochar:

In the dye adsorption study, experiments were carried out with a single pollutant system for all experiments at 200 rpm using an incubator shaker. A dye stock solution of 500 mg L^{-1} was prepared using double distilled water. Successive dilutions of the stock solution were prepared (20 mg L^{-1} -100 mg L^{-1}), and a volume of 2 mL was taken for the spectrophotometric study. Various

experimental parameters such as pH, biosorbent dosages, contact time, initial dye concentration was analyzed. At first, the pH of the dye solutions was adjusted by adding 0.01 M hydrochloric acid and 0.01 M sodium hydroxide solution using a digital pH meter. Raw biosorbent (RCS, CES) and activated biosorbent (RCSB and CESB (0.5 g-2.5 g) were mixed with different dye concentrations in 50 ml centrifuge tubes and stirred in an orbital incubator shaker at 200 rpm. After a specific equilibrium time, the tubes were removed from the shaker, and 2 ml of supernatant was centrifuged at 10,000 rpm for 10 minutes to separate the solids from the aqueous solution. The dye concentration was determined using a double-beam UV-vis spectrophotometer (Agilent, Cary-100) at 664 nm and 617 nm for MB and MG, respectively. All the experiments were performed in triplicate for data consistency, and mean data was estimated in all experiments. Adsorption experiments were conducted by varying initial solution pH (3-9), contact time (15-180 min), adsorbent dose (0.5-2.5 gm L^{-1}), initial dye concentration (10-100 mg L^{-1}), particle size (150-1000 µm), RPM (100-200) and temperature (293-323 K). The effect of contact time (15 to 180 mins) was studied at fixed adsorbent dose, temperature, concentration, and solution pH to determine the biosorption kinetics. The adsorption isotherm was analyzed with the varying initial dye concentration (20 mg L^{-1} to 200 mg L^{-1} at 30 °C and pH 7. The amount of dye adsorbed per unit mass of adsorbent, i.e., the adsorbent capacity (q_e, mg g^{-1}) and % dye removal at equilibrium, was calculated according to the following equations.

$$q_e = \frac{(C_o - C_e)V}{m}$$

$$\% \text{ removal} = \frac{(C_o - C_e) \times 100}{C_o}$$

Where C_o and C_e are the initial and equilibrium dye concentration (mg L^{-1}), V is the volume of dye solution (L), and m is the amount (g) of the adsorbent added.

2.6.2 Toxic metal removal studies using activated biochar and hydrochar:

In this chapter, the toxic metal adsorption studies of activated biochar (RCSB & CESB) were carried out as batch experiments. Experimental parameters were performed for cadmium (Cd^{2+}) adsorption and lead (Pb^{2+}) metal ions. Both biochars (RCSB and CESB) were treated with 10 mg·L^{-1} of eight trace metal ions, *viz.* cadmium, lead, nickel, zinc, copper, mercury, arsenic, and chromium. Among these eight metal ions, cadmium and lead shows excellent adsorption capacity (~92–98%) than other metals. Hence cadmium and lead ions have been chosen for subsequent adsorption studies with RCSB and CESB to get an optimized result. 1000ppm of cadmium (Cd^{2+}) and lead (Pb^{2+}) metal ions stock solution were prepared for further detailed experiments. The metal solutions' initial experimental concentration (20 ppm) was prepared by diluting from the stock solutions. The adsorption optimization was carried out by varying experimental parameters such as adsorbent dose (0.2–1.5 g/L), pH (2 to 9), contact time (10 to 120 mins), and initial metal ion

concentration (10 to 100 ppm). All the experiments were performed in a 100 ml conical flask with a 50 ml working concentration of metals at room temperature with 200 rpm. The pH of the solutions was maintained by using 0.1 M HCl or 0.1 M NaOH solutions. All the experiments were performed twice to get an optimized result. Atomic absorption spectroscopy (AAS) was used for the experimental analysis by evaluating the initial and final concentration of cadmium (Cd^{2+}) and lead (Pb^{2+}) metals ions before and after the adsorption experiments using activated biochar (RCSB and CESB). The adsorption capacity (q_e) and percentage removal (% R) were determined using the following equations.

$$q_e = \frac{(C_o - C_e)V}{m} \quad (1)$$

$$\% \text{ removal} = \frac{(C_o - C_e) \times 100}{C_o} \quad (2)$$

Where C_o and C_e are the initial and equilibrium metal concentration (mg L^{-1}), V is the volume of metal solution (ml), and m is the amount (mg) of the adsorbent added.

2.6.3 Adsorption Kinetics Studies

Adsorption kinetics refers to the study of the rate and mechanism of the process of adsorption, which is the accumulation of molecules or particles on the surface of a solid or liquid material. The kinetics of adsorption involves studying the time-dependent process of adsorption, which can be described by mathematical models that relate the amount of adsorbate adsorbed per unit surface area to the adsorption time. These models consider factors such as the surface area and porosity of the adsorbent, the adsorbate properties, the temperature, and the adsorbate concentration in the bulk solution. To evaluate the kinetics mechanism for the adsorption of heavy metals, the adsorption can be explained by using the non-linear regression method of different kinetics models. The uptake rate of the adsorbate onto the adsorbent surface determines the equilibrium time for the adsorption of the system. The kinetics rate is required for selecting optimum operating conditions for the full-scale batch process [2.4]. The Lagergren pseudo-first-order kinetics model is employed to investigate the adsorption of the solid-liquid system based on adsorbent capacity [2.5], where one adsorbate reacts with one active site on the surface. The non-linearized form of the pseudo-first-order, pseudo-second-order, and intraparticle diffusion model can be explained by using the following Equations [2.6]

$$q_t = q_e(1 - exp(-k_1 t)) \quad (3)$$

$$q_t = \frac{{q_e}^2 K_2 t}{q_e K_2 t + 1} \quad (4)$$

Intraparticle diffusion is the most widely applied intraparticle diffusion equation for adsorption systems given by Weber and Morris [2.7]

$$q_t = k_i t^{\frac{1}{2}} + C \quad (5)$$

Where q_t (mg g^{-1}) and q_e (mg g^{-1}) are adsorption capacity at time t and equilibrium state respectively, K_1(g/(mg·min)) and K_2 (g/(mg·min)) and K_i (g/(mg·$min^{1/2}$)) are first order, second order, and intraparticle diffusion rate constants respectively. These models can be used to determine the adsorption process's rate constants, equilibrium constants, and diffusion coefficients. Understanding adsorption kinetics is essential for designing and optimizing adsorption processes in various applications, including environmental and industrial remediation.

2.6.4 Adsorption isotherm studies

Adsorption isotherm studies are fundamental for investigating and understanding the adsorption process. An adsorption isotherm is a relationship that describes the equilibrium between the concentration of the adsorbate in the bulk solution, and the amount of adsorbate adsorbed onto the surface of the adsorbent. Adsorption isotherms can be experimentally determined by measuring the amount of adsorbate adsorbed at different adsorbate concentrations in the solution and plotting the data as a function of the equilibrium concentration of the adsorbate in the bulk solution. The Langmuir and Freundlich isotherms are the most commonly used adsorption models [2.8]. The Langmuir isotherm assumes that the adsorption process occurs on a homogeneous surface with a finite number of identical adsorption sites and that there is a maximum adsorption capacity. The Freundlich isotherm assumes that the adsorption process occurs on a heterogeneous surface with different adsorption energies and that the adsorption capacity increases continuously with increasing concentration of the adsorbate[2.9]. Knowing the parameters involved in the adsorbate-adsorbent interaction is very important for designing a preferred sorption system. The adsorbent surface may be considered a monolayer or multilayer. Several isotherm models have been applied to fit the experimental data and evaluate the applicability to MG and MB dye adsorption.

2.6.4.1 Langmuir isotherm

The Langmuir model assumes that monolayer adsorption occurs on a surface with a finite number of identical sites. All the sites are energetically equivalent, and there is no interaction between the adsorbed molecules. The non-linear Langmuir equation is given by Eq. (6) [2.6].

$$q_e = \frac{q_m K_L C_e}{1 + K_L C_e} \quad (6)$$

Where C_e (mg L^{-1}) is the equilibrium concentration of adsorbate, q_e (mg g^{-1}) is the adsorbate amount per unit mass of the adsorbent. Q_m is the maximum monolayer uptake by the adsorbent, and b (L mg^{-1}) is the Langmuir constant reflecting the free energy of adsorption (mg L^{-1}). The slope and the intercept of the linear plot of C_e/q_e versus C_e give the values of b and Q_m, respectively. Another essential parameter, as described by Hall et al. [2.10], called the "constant separation factor" (R_L), is characteristic of Langmuir isotherm to determine the feasibility of the adsorption process. It is defined by Eq. 7.

$$R_L = \frac{1}{1+bC_o} \tag{7}$$

Where b is the Langmuir constant, and C_o is the initial dye concentration, respectively. On an excellent adsorption process, $0 < R_L < 1$; If $R_L = 0$, adsorption is irreversible, and $R_L > 1$ is favorable.

2.6.4.2 Freundlich isotherm

The Freundlich isotherm is an empirical equation derived by assuming that adsorption occurs on the heterogeneous surface through a multilayer adsorption mechanism and that adsorption capacity is related to the dye concentration at equilibrium. The Freundlich equation is expressed in a non-linear form, as shown in Eq. (8), [2.6]

$$q_e = K_F C_e^{\frac{1}{n}} \tag{8}$$

K_F in the above equation denotes the Freundlich constant related to bonding energy, and n represents the surface heterogeneity factor indicating adsorption intensity. The K_F is the reaction rate constant of Freundlich, and 1/n(dimensionless) is the affinity of adsorption. The value of 'n' is considered a measure to estimate the favorability of the sorption process. Values n > 1 represents favorable adsorption condition [2.11], [2.12].

2.6.4.3 Effect of Temperature on Adsorption and thermodynamics studies

The extent of adsorption depends on the temperature of the solid-liquid interface. Adsorption at different temperatures gives the feasibility of the adsorption system, which exhibits the thermodynamic characteristics of the adsorption. Thermodynamic parameters such as Gibbs free energy (ΔG°, kJ mol^{-1}), enthalpy change (ΔH° kJ mol^{-1}), and entropy change (ΔS° J mol^{-1}) were determined by using Van't Hoff equation as

$$\ln k_c = \frac{\Delta S^o}{R} - \frac{\Delta H^o}{RT} \tag{9}$$

$$\Delta G^\circ = -RT\ln(k_c) \tag{10}$$

$$\Delta G^\circ = \Delta H^\circ - T\Delta S^\circ \tag{11}$$

K_c is the thermodynamic equilibrium constant defined by q_e/C_e, where q_e is the dye concentration on the adsorbent at equilibrium and C_e is the remaining dye concentration in the solution at equilibrium [2.5]. R is the universal gas constant (8.314 J mol^{-1} K^{-1}), and T is the temperature in K.

2.7 Carbon dots synthesis and application in toxic metal ion sensing:

Hydrochar and nitrogen-doped carbon dots were synthesized using the *Colocasia esculanta* stem by hydrothermal method. 2 gm of dried *Colocasia esculanta* stem was transferred to a hydrothermal autoclave containing 40 ml H_2O, and 2.0 ml of ammonium hydroxide was added as a dopant. The autoclave was heated at 200 °C for 8 hours. Subsequently, the hydrothermal autoclave was allowed to cool down to room temperature. The mixture was filtered through a 0.22 µ membrane filter. The residue left over on the membrane filter was referred to as *Colocasia esculanta* stem hydrochar (CESH) and was used for toxic metal removal studies. The nitrogen-doped c-dots (NCD) solution emitting green fluorescence was separated using a 0.22 µ membrane filter followed by column chromatography. The filtrate was dried under vacuum in rota vapor and subsequently freeze-dried to obtain a solid brown NCD, which was used for toxic metal sensing applications. The synthesized NCDs were kept at 4°C for further analysis.

2.7.1 Stern Volmer equation:

The stern Volmer equation is widely used in fluorescence spectroscopy that relates the fluorescence intensity of a fluorophore to the concentration of a quencher molecule. The equation is named after Otto Stern and Max Volmer, who proposed it in 1919. The Stern-Volmer equation is expressed as

$$\left(\frac{Io}{I}\right) = Ksv(M) + 1 \qquad (12)$$

Where I_o is the initial FL intensity of the NCDs, I is the intensity after the addition of the metal ions, [M] represents the concentration of the metal ions, and K_{SV} denotes the Stern–Volmer constant. The Stern-Volmer equation assumes that the quenching occurs via a dynamic collision between the fluorophore and the quencher molecule, forming a non-fluorescence complex. However, the quencher mechanism may be more complex in some cases, involving energy or electron transfer. The stern-Volmer equation is commonly used in various applications, such as determining dissolved oxygen concentration in solutions, measuring enzyme activities, and detecting metal ions in biological samples. It is a simple and powerful tool for the quantitative

analysis of fluorescence quenching, providing valuable information on the nature and efficiency of the quenching process.

2.7.2 Quantum yield measurement

The quantum yield QY(Φ) was calculated by comparing it with the reference sample quinine sulfate. Both the reference material and sample material were excited at the same wavelength. QY(Φ) of CDs was calculated using the standard formula below. (Φ = 54% in 0.1 M H_2SO_4) at the excitation wavelength of 367 nm.

$$\Phi_S = \Phi_R \times \frac{I_S}{I_R} \times \frac{Abs_R}{Abs_S} \times \frac{\eta_S^2}{\eta_R^2} \quad (7)$$

Φ_R and Φ_S indicate the quantum yield of the reference and sample; I_s and I_R refers integrated fluorescence intensity of the sample, and reference A_S and A_R refer to the area under the emission peak of the sample and reference; Abs_R and Abs_S are the absorbance reading of the reference and sample, respectively; at an excitation wavelength of 345 nm at a slit width of 2 nm and η refers to the refractive index of the solvent (1.33 for both the sample and reference). The quantum yield (Φ) of quinine sulfate was 54%.

References:

[2.1] Y. Li *et al.*, 'Microwave-assisted hydrothermal preparation of rice straw hydrochars for adsorption of organics and heavy metals,' *Bioresour. Technol.*, vol. 273, no. August 2018, pp. 136–143, 2019, doi: 10.1016/j.biortech.2018.10.056.

[2.2] W. Li, X. Liao, L. Wang, and Z. Huang, 'Adsorption of cadmium and lead in wastewater by four kinds of biomass xanthates,' *Water Sci. Technol.*, vol. 79, no. 6, pp. 1222–1230, 2019, doi: 10.2166/wst.2019.124.

[2.3] H. S. Kambo and A. Dutta, 'A comparative review of biochar and hydrochar in terms of production, physicochemical properties, and applications,' *Renew. Sustain. Energy Rev.*, vol. 45, pp. 359–378, 2015, doi 10.1016/j.rser.2015.01.050.

[2.4] J. Saikia and G. Das, 'Framboidal vaterite for selective adsorption of anionic dyes,' *J. Environ. Chem. Eng.*, vol. 2, no. 2, pp. 1165–1173, 2014, doi: 10.1016/j.jece.2014.04.016.

[2.5] S. Banerjee, R. K. Gautam, A. Jaiswal, P. K. Gautam, and M. C. Chattopadhyaya, 'Study on adsorption behavior of Acid Orange 10 onto modified wheat husk', *Desalin. Water Treat.*, vol. 57, no. 26, pp. 12302–12315, 2016, doi: 10.1080/19443994.2015.1046151.

[2.6] A. R. P. Hidayat *et al.*, 'Linear and non-linear isotherm, kinetic and thermodynamic behavior of methyl orange adsorption using modulated Al2O3@UiO-66 via acetic acid', *J. Environ. Chem. Eng.*, vol. 9, no. 6, p. 106675, 2021, doi: 10.1016/j.jece.2021.106675.

[2.7] W. J. Weber Jr and J. C. Morris, 'Kinetics of adsorption on carbon from solution,' *J.*

Sanit. Eng. Div., vol. 89, no. 2, pp. 31–59, 1963.

[2.8] M. M. Majd, V. Kordzadeh-Kermani, V. Ghalandari, A. Askari, and M. Sillanpää, 'Adsorption isotherm models: A comprehensive and systematic review (2010- 2020)', *Sci. Total Environ.*, vol. 812, p. 151334, 2022.

[2.9] Y. Qiu, Z. Zheng, Z. Zhou, and G. D. Sheng, 'Effectiveness and mechanisms of dye adsorption on a straw-based biochar.', *Bioresour. Technol.*, vol. 100, no. 21, pp. 5348–5351, Nov. 2009, doi: 10.1016/j.biortech.2009.05.054.

[2.10] K. R. Hall, L. C. Eagleton, A. Acrivos, and T. Vermeulen, 'Pore- and Solid-Diffusion Kinetics in Fixed-Bed Adsorption Under Constant- Pattern Conditions,' *Ind. Eng. Chem. Res.*, vol. 5, no. 2, pp. 212–223, 1966, doi: 10.1021/i160018a011.

[2.11] H. Freundlich, 'Over the adsorption in solution,' *J. Phys. Chem.*, vol. 57, no. 385471, pp. 1100–1107, 1906.

[2.12] R.E. Treybal, *Mass transfer operations*, 3rd ed. McGraw Hill, New York, 1980.

Chapter 3

A comparative study of raw *vs.* activated biochar derived from "*Ricinus communis*" stem for preferential removal of cationic dyes

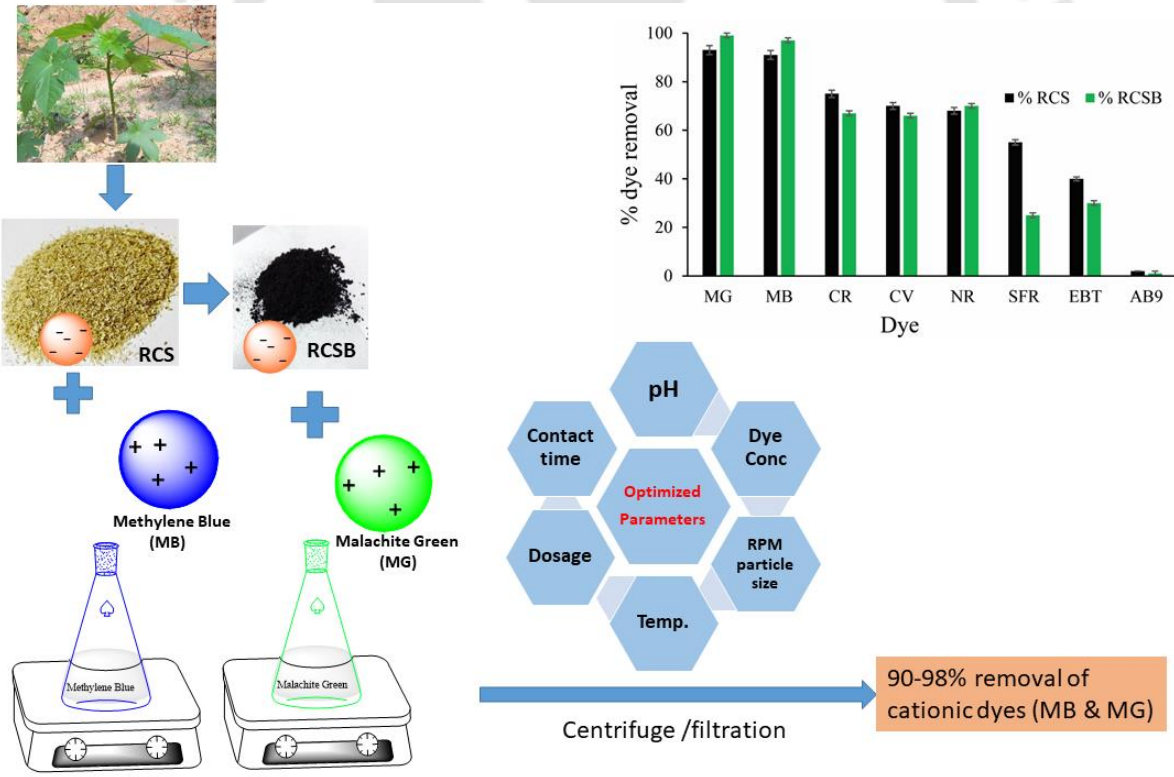

3.1. Background and focus of the chapter:

Urbanization and industrial development have led to enormous wastewater discharge into the environment, which includes organic and inorganic pollutants, pesticides, heavy metals, dye, etc. Organic pollutants include complex synthetic dyes, pharmaceuticals, processed petroleum, and oil derived from crudes. Synthetic dyes are one of the leading causes of water pollution. Dyes-containing industrial effluent from plastic, paint paper, textiles, pigment production, cosmetics, and food industries are discharged into the environment without efficient treatment [3.1]. The main feature of these effluents includes a higher amount of alkaline content, biological oxygen demand(BOD), chemical oxygen demand (COD), and total dissolved solids with a concentration of dye/dm^3 below 1 g [3.2]. Dyes are aromatic compounds resistant to light and non-biodegradable, causing detrimental effects on human health, animals, and aquatic biota. Textile industries are the largest user of dyes, and environmental regulations have been imposed to separate dyes from their discharged wastewater. However, managing the wastewater outflow has been difficult over time [3.3]. Various physical, chemical, photochemical, and biological methods have been established to remove dyes from wastewater[3.4]. High operational costs, toxic reagents, and long process time restrict these conventional methods at an industrial scale. Therefore, developing an eco-friendly process for removing dyes from industrial wastewater is essential. The adsorption method is better for water treatment due to its flexibility, ease of operation, high efficiency, insensitivity toward environmental pollutants, economic feasibility, and recyclability [3.5,3.6].

Biochar is charcoal produced by heating organic materials in the absence or a limited oxygen supply. It has been shown to have great potential for use in environmental applications, including removing pollutants from water. One area of interest is the use of biochar for the removal of cationic dyes from wastewater. In recent studies, raw and activated biochar has been used for cationic dye removal [3.7]. Raw biosorbent has not gone through any additional treatment. In contrast, activated biochar has been treated with a chemical or physical process to increase its surface area and enhance its adsorption properties. The use of raw biosorbent for cationic dye removal is effective, with high removal efficiencies observed in several studies. However, using activated biochar is even more effective, with significantly higher removal efficiencies observed due to its high surface area and enhanced adsorption properties.

Plant-derived biosorbents are proposed as low-cost alternative adsorbents due to the high content of cellulose and lignocellulose[3.8]. It has various advantages, such as ease of disposal, biodegradability, low cost, abundance, and ecological viability, and is technically feasible for long-term industrial use [3.9]. During the past decade, plant-derived biosorbents have been utilized for the removal of malachite green (MG) and methylene blue (MB) dyes and other impurities from wastewater, which includes rice husk, rice straw, chitosan, bagasse, orange peel, cauliflower leaves, kaolin clay, Carica papaya wood, cashew nut shell, sawdust, wood, pine needles, green grass, eucalyptus bark, peanut shell, coconut shell, and coir dust activated carbon, corn cob, walnut shell, many more [3.10]. A recent study shows hydrogel removes MG (97.5%) and MB (96.3%) dyes. The adsorption isotherm data were best fitted by Langmuir adsorption isotherm with maximum adsorption capacity of 51 mg/g, 68.71 mg/g for MG-RCS, MB-RCS, and 60.278 mg/g, 80.7 mg/g and MG-RCSB and MB-RCSB respectively, followed by pseudo-second-order kinetics for both dyes. The hydrogel can be recycled for up to ten cycles and is a proficient, reusable, and eco-friendly adsorbent for wastewater remediation [3.11]. MB and MG dye fall under cationic dyes; MB dyes are used in medicine, biotechnology, chemistry, biology, and printing and dye industries. Many physiological problems can arise from long-term exposure to dyes, including vomiting, nausea, anemia, and high blood pressure. On the other hand, malachite green (MG), a triarylmethane dye used as an antimicrobial and antifungal agent in the food industry, a curative agent in aquaculture, and very useful for dyeing wool, silk, jute, cotton, leather, etc. [3.12,3.13]**.** The MG dye is a toxic chemical to mammalian cells and functions as a tumor-enhancing agent. These dyes in the food chain could cause mutagenic, carcinogenic, and teratogenic effects on human cells[3.14].

In our study,plant-derived raw and activated biochar has been used to remove cationic dyes. Biochar is a black, carbon-based, highly porous structure with various functional compounds such as carboxyl, hydroxyl, and phenolic groups. It shows a strong affinity towards organic pollutants [3.15]. Biochars produced at low temperatures are energy-saving and more suitable for removing contaminants because they are rich in oxygen-containing functional groups [3.16]. Biochar can be formed by biomass pyrolysis (such as a leaf, straw, sawdust, etc.) under anaerobic conditions[3.17,3.18]. Biochar has been extensively used in wastewater treatment as an eco-friendly material [3.19] due to its porous surface and strong adsorption properties. Activated biochar has received more attention than natural raw biosorbents due to its well-developed porous structures, large surface area, and broad spectrum of surface functional groups. Biochar can be activated in two ways

one is physical activation, and another is chemical activation. Chemical activation is better since it combines both carbonization and activation, and it could transform into better porous structures than physical activation[3.20]. The most commonly used activating agents include H_3PO_4, $ZnCl_2$, NaOH, KOH, and K_2CO_3 [3.21,3.22].

Regarding the novelty of our work, the biochar reported in the present work was synthesized at a low temperature (300˚C) compared to other literature methods. As in most of the literature, the synthesis of biochar is generally carried out at higher temperatures (350-700˚C). Here we have used K_2CO_3 as activating agent for biochar synthesis since other alkali hydroxides are exorbitant, abrasive, and unsafe, creating discarding problems. However, K_2CO_3 is not hazardous as it is often added to foods as an additive. Therefore K_2CO_3 is used as an activating agent in the present study, which has not been used earlier. After K_2CO_3 activation and carbonization, our biochar's surface area and pore volume increased, which has been confirmed by BET surface area measurement[3.23].

Recent studies have described various adsorbents like a pomegranate [3.24], cactus fruit peel [3.25], olive -pomace [3.26], and sugar scum [3.27], which are used for the removal of cationic dyes. Our study plant, *Ricinus communis* (Castor plant), has three significant parts, i.e., leaves, seeds, and stem. Among these three, leaves are used as feed for Eri-silkworm [3.28], and seeds are used for biodiesel production [3.29], but the stem of this plant has no practical use. Hence we have used its stem for a heavy metal removal study. The most significant barrier of these biosorbents is their application by industries as a cost-effective adsorbent and the difficulties associated with regeneration [3.30], hence the main focus of this study is to develop K_2CO_3-activated biochar from renewable biomass waste RCSB as a low-cost biosorbent. Synthesized RCSB was tested for removing MB and MG dyes from the synthetic wastewater under optimized adsorption operational conditions such as solution pH, dye concentration, dosage, contact time, and temperature.

3.2. Result & Discussions

3.2.1 Adsorption experiments with different dyes

At first, 20mg of adsorbents RCS and RCSB were treated with 20 mg L^{-1} of nine different dyes, as shown in figure A3.1**.** These dyes were malachite green (MG), methylene blue (MB), congo Red (CR), crystal Violet (CV), neutral Red (NR), safranin (SFR), eriochrome Black T (EBT), acid Blue 9 (AB9) and bromophenol blue (BPB). Among these nine dyes, MG and MB show better adsorption capacity (~ 88-98%) than other dyes, as depicted in Figure 3.1; hence, MG and MB have been chosen

for subsequent RCS and RCSB adsorption studies to get an optimized result. MG and MB adsorb two dyes more than others, such as CR, CV, NR, SFR, EBT, AB9, and BPB, on the RCS and RCSB surfaces. Both biosorbents bind easily with the dyes containing N-methyl and amine group (i.e., MG, MB, CR, CV, and NR), which gives the higher adsorption efficiency of these dyes as compared to other which doesn't have these functional groups**.**

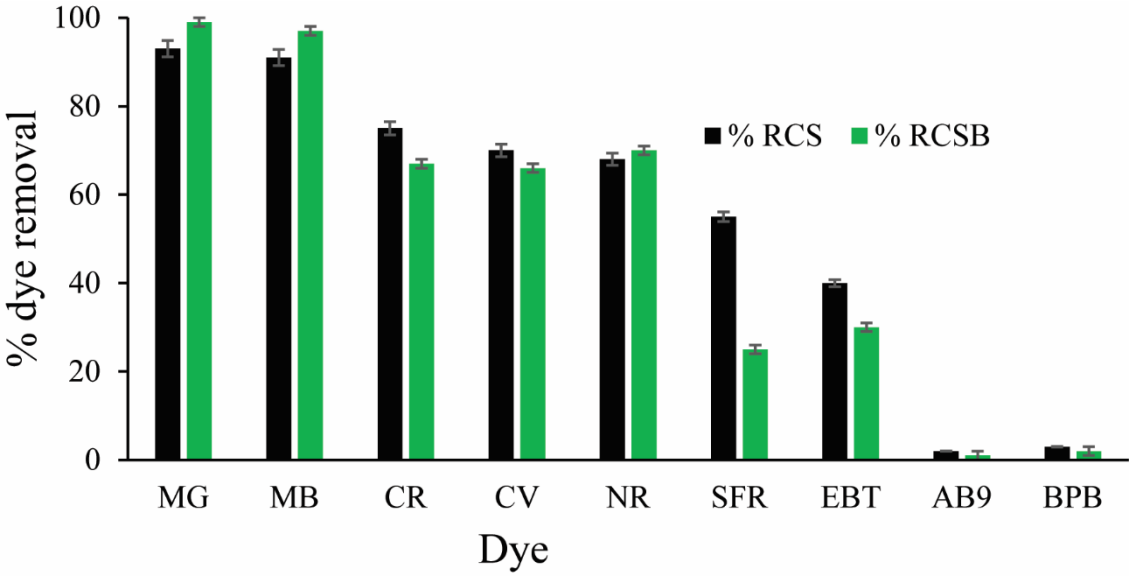

Figure 3.1 % dye removal of nine dyes on RCS and RCSB surfaces.

3.2.2 Characterization of RCS & RCSB

Fourier transforms infrared (FT-IR) spectroscopy was used to determine the changes in the type and number of functional groups on the surface of raw and activated FTIR-analyzed biochar. Figure 3.2(a-b) depicts the FTIR spectra of raw sample RCS taken before activation with K_2CO_3 solution in water and after its addition. In the case of RCS, spectral bands at 3323 cm^{-1} correspond to -OH groups. The spectral bands at 2900, 1599, 1425, 1370, 1307, 1231, 1145, and 871 cm^{-1} were assigned to asymmetrical stretching of C-H_2 [3.31,3.32]-, >C=O(1730 cm^{-1}) and -C-H bending (1425 cm^{-1}). The peaks at 1307 cm^{-1} (RCS) and 1370 cm^{-1} indicated C-H bending due to cellulose, hemicellulose, and lignin [3.33]. The peak at 1231 cm^{-1} (RCS) shows C-C and C-O stretching due to lignin [3.33]. Lignin starts to decompose slower over a broader temperature range (200-500˚C) than cellulose and hemicellulose components of biomass because various oxygen functional groups from its structure have different thermal stabilities, and their scission occurs at different temperatures, which can be seen from the FTIR spectra of RCSB [3.34]. In the FTIR spectra, the sharpness of the RCS peaks

between 1030 cm^{-1} -1425 cm^{-1} decreases to broader peaks at 1030 cm^{-1} and 1404 cm^{-1} after the addition of K_2CO_3 (300°C) to prepare RCSB. This may be due to the decomposition of lignin. It can be seen that the ester band signal at 1730 cm^{-1} disappeared after

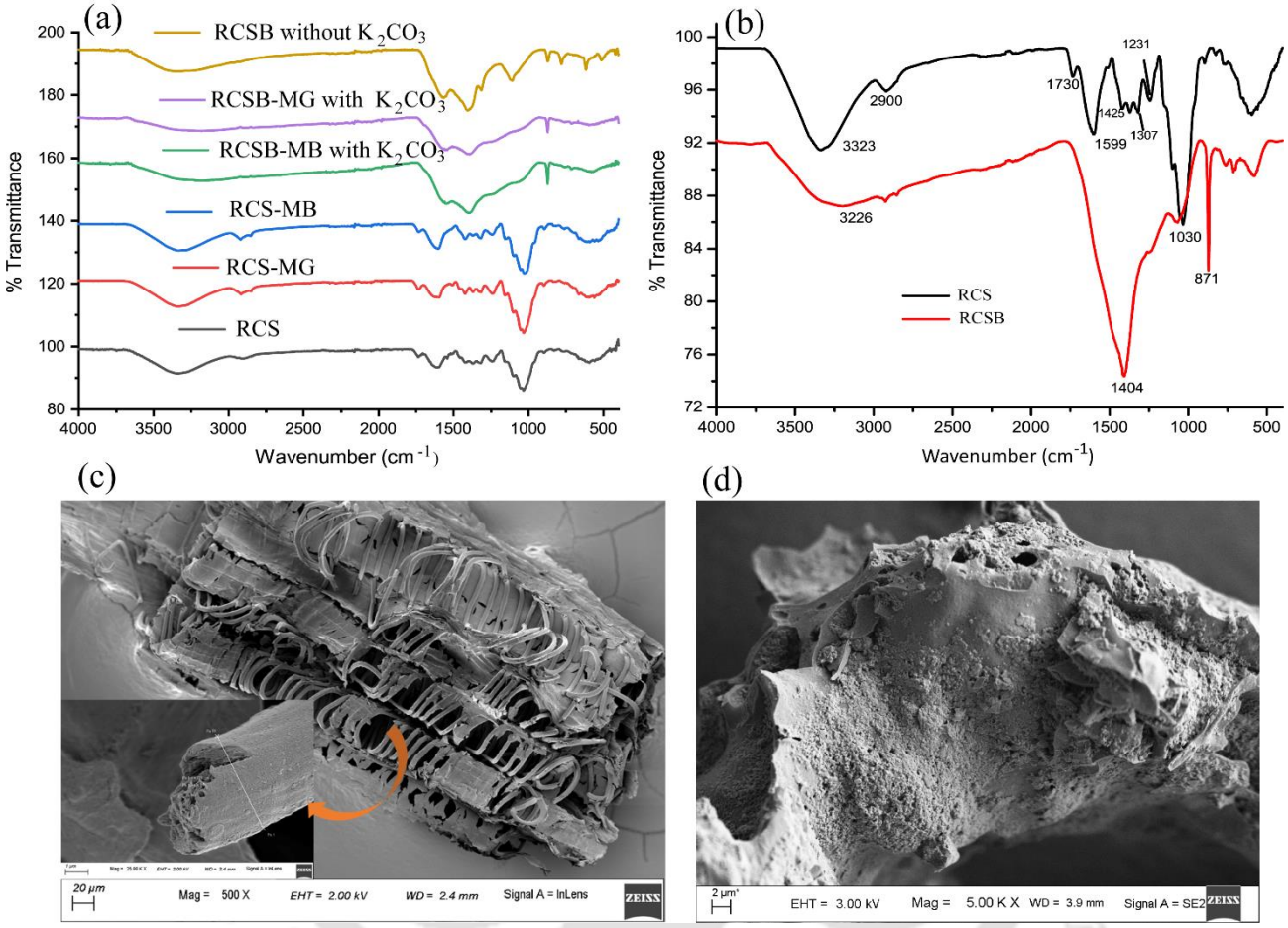

Figure 3.2 (a-b) FTIR spectra of RCS, RCSB in the presence and absence of dye and K_2CO_3 (c-d) FE-SEM image of RCS and RCSB

The impregnation of K_2CO_3. The possible reason is that the formed KOH further diffused into the interior of the *Ricinus communis* stem and disrupted the key ester linkages between lignin and carbohydrates. [3.35] . The syringyl lignin peak at 1323 cm^{-1} of RCS has decreased significantly in RCSB. In RCSB without K_2CO_3, 1112cm^{-1} peaks arise from C-OH skeletal vibration [3.36] stretching.The peaks at 1033cm^{-1} are attributed to the C-O-C stretching typical of xylan. The small sharp band at 898 cm^{-1} is due to predominant β- glycosidic linkages between the sugar units [3.37]. The infrared bands at 714 cm^{-1} ,872 cm^{-1} and 1412 cm^{-1} are assigned to the CO_3^{2-} stretching frequency

of K_2CO_3 [3.38].

$K_2CO_3+H_2O = KHCO_3+KOH$

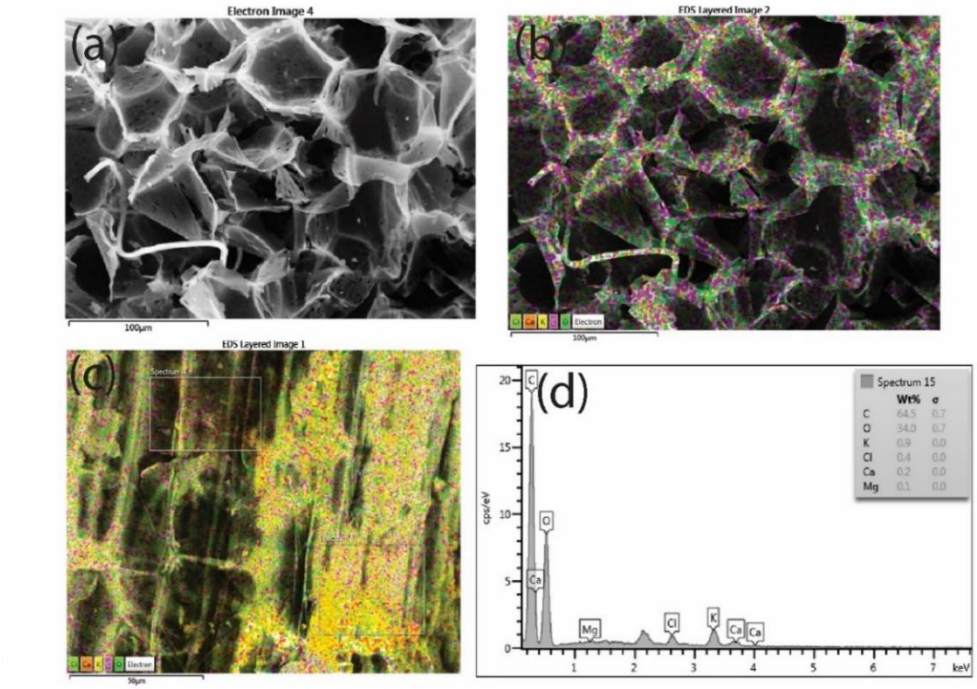

Figure 3.3 (a-d) EDX elemental mapping of RCS

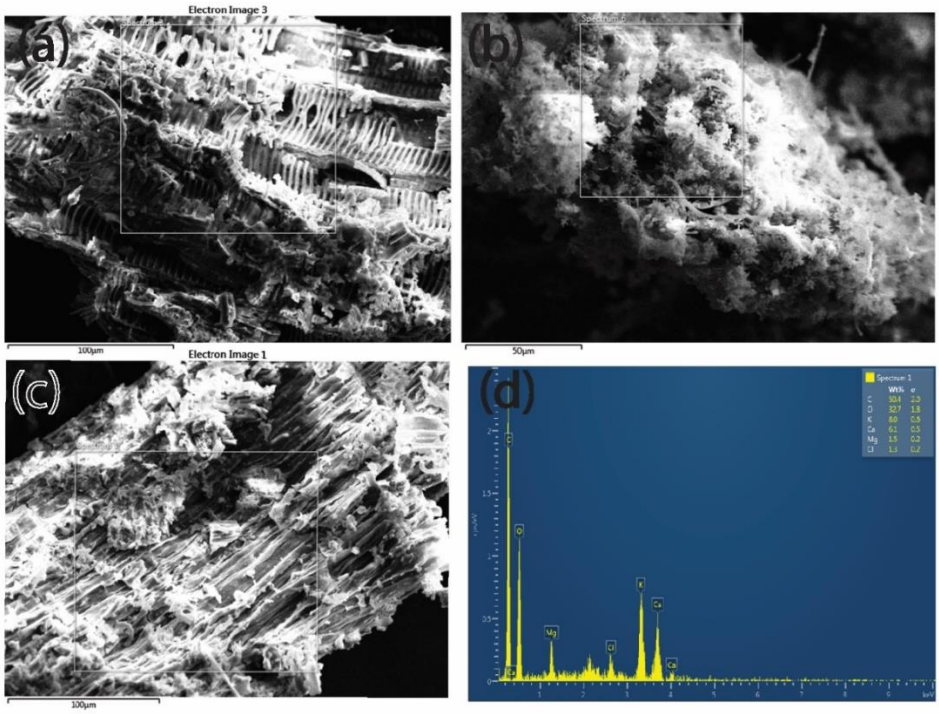

Figure 3.4 (a-d) EDX elemental mapping of RCSB

The addition of potassium carbonate and the formation of potassium hydroxide during the impregnation process would destroy the cellulose structure, weaken the hydrogen bonds between the cellulose molecules, and reduce the activation energy of the reaction so that the pyrolysis of high polymer molecules in a high-temperature conditions were more thorough. Therefore, it is possible that cellulose, hemicellulose, and lignin, having many OH groups in their structure, make up most of the absorbing layer[3.39]. The surface area was calculated via the BET method for RCS and RCSB; the specific surface area, pore volume, and pore diameter were found to be 0.963 m^2/g,0.006 cc/g,16.149 Å for RCS and 11.786 m^2/g, 0.048 cc/g and 3.616 nm for RCSB respectively. Figure 3.5 (a,b) shows the surface area and pore radius of RCS and RCSB, respectively, where we have seen an increase in the surface area and pore volume increased after chemical activation. MB and MG dyes are adsorbed at these macropores RCS and mesopores of RCSB. Thermogravimetric analysis (TGA) has been done to determine the change in weight with the temperature change. TGA data provides information about the temperature range over which the sample is stable or unstable. As shown in Figure A3.2, the thermogravimetric profile illustrates that the mass loss occurred in three stages. The first stage is at around 50°C-160°C (RCS) and 40°C-180°C (RCSB), with weight loss of 10 % and 20%, respectively, related mainly to loss of water present on the surface of the materials. The second stage degradation temperature at 160-240 ˚C (RCS) and 180-270˚C (RCSB) with a weight loss of 37% and 40%, respectively, due to loss of chemisorbed water. The last weight loss was determined above 240-600 ˚C (RCS) and 270-600˚C (RCSB), which was about 20 % due to the elimination of volatile material rich in functional groups. Hence, the TGA data indicates the thermal stability of the biosorbent at a temperature of 300°C. The surface morphology in Figure 3.2 (c-d) shows many orderly spiral-shaped pores, holes, and cave-type openings with heterogeneous porous surfaces. The micrograph indicates the external surface of RCSB is more porous than RCS. Elemental analysis with mapping of the adsorbents was carried out using Energy Dispersive X-ray Spectroscopy (EDX) Figure 3.4(a-d) for RCS and RCSB, Figure 3.4 (a-d). EDX spectra show that carbon and oxygen were the major components (C=64.5%, O=34% for RCS and C=50.4%, O=32.7% for RCSB). Before adsorption, the zeta potential(ζ) value of biosorbents (RCS, RCSB) was -60mV and -65mV at pH 6.0. After the adsorption of dyes, zeta potential values become between -24 mV to -40 mV, as depicted in Figure A3.3. At low pH values, the surface of the biosorbent was surrounded with hydrogen ions, and the cationic dyes (MG and MB) could not compete for adsorption sites[3.40]. At the same time, the activity of functional groups in RCS and RCSB (e.g., hydroxyl and carboxyl) was affected by pH.

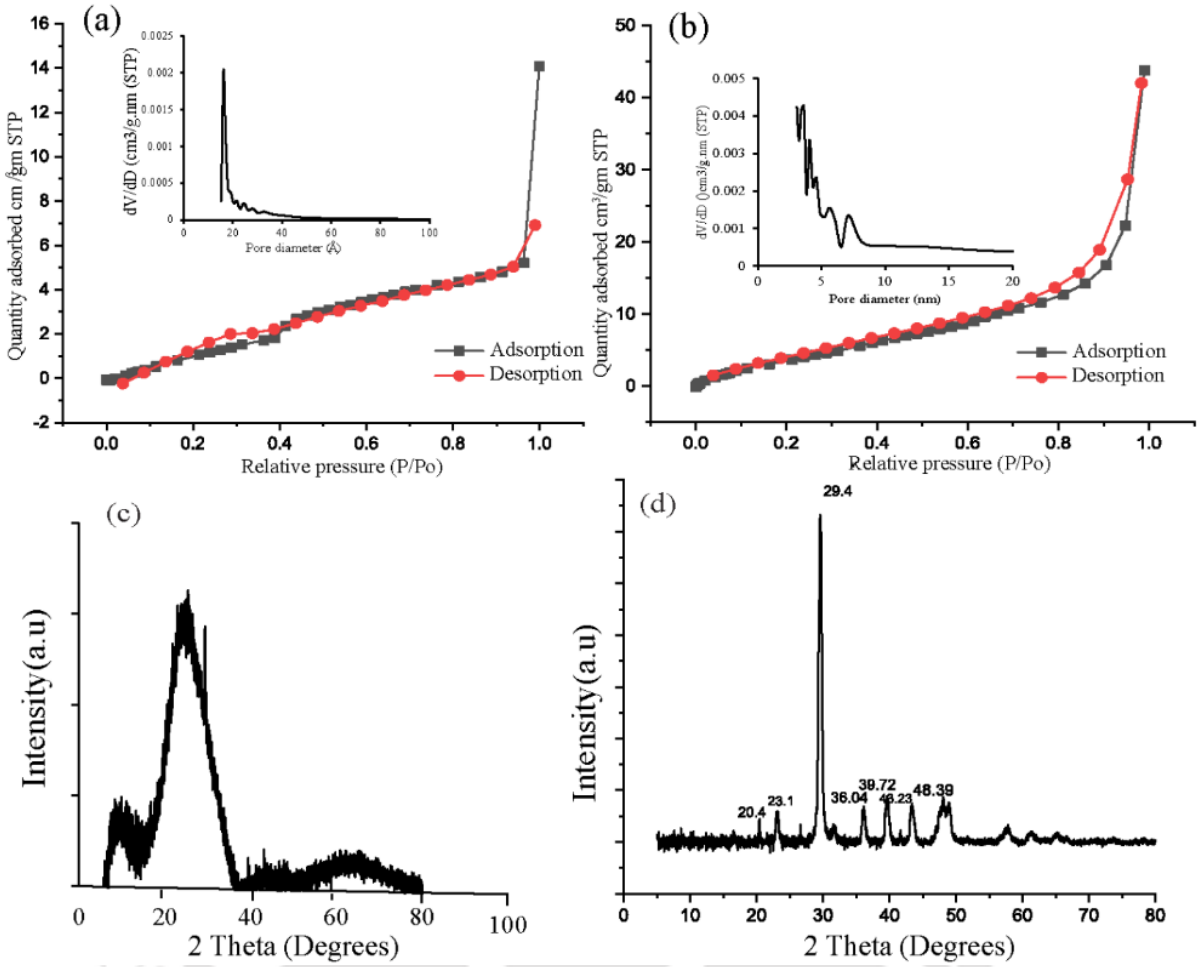

Figure 3.5 N adsorption-desorption isotherm (INSET: pore -size distribution curve) of **a** RCS, **b** RCSB and XRD data of **c** RCS, **d** RCSB

The interaction with the functional groups presents in RCS and RCSB could explain the change in the surface charge. The increased positive charge on RCS and RCSB functional groups at low pH values restricted the positively charged MG and MB approach. However, the repulsive force decreased from the increased pH of hydrogen ions, so more RCS and RCSB functional groups became negatively charged. Electrostatic repulsion decreased with the subsequent attraction of cationic and adsorption on the RCS and RCSB surface[3.41]. The effect of the solution pH on dye adsorption can be explained based on the adsorbent's pH zero-point charge or isoelectric point. The point of zero charges (pH_{pzc}) can be described as the pH at which the net charge of the total particle surface (i.e., absorbent's surface) is equal to zero. The solid addition method determined the zero surface charge of RCS and RCSB [3.42]. 50 mL of 0.1M KNO_3 solution in six separate 100 ml stoppered conical flasks. The pH

of the solution was adjusted from 2 to 12 by adding hydrochloric acid and sodium hydroxide, and 0.2 gm of RCS and RCSB were placed in six capped bottles, and 0.15 g of RCS and RCSB were then added to the KNO_3 solutions. The final pH was measured after stirring magnetically for 48 h at 30°C. The difference between the initial and final pH (pH_i-pH_f) was plotted against the initial pH (pH_i) (Fig. A3.4). The point of intersection of the resulting curve with abscissa gave the pH_{pzc} value. The value of pH_{pzc} for RCS and RCSB was found to be 6.65 and 6.5, respectively.

3.3 Adsorption study of dyes on RCS and RCSB

3.3.1 Effect of adsorbent dosage

The effect of adsorbent dosage has been studied at a range of 0.5-2.5 gL^{-1} in a 20 ml solution of 20 mg L^{-1} dye concentration. The study was conducted to find the minimum economic dose. Figure 3.6 (c-d) depicts the increase in dye removal efficiency as the adsorbent dose was increased from 0.5-2.5

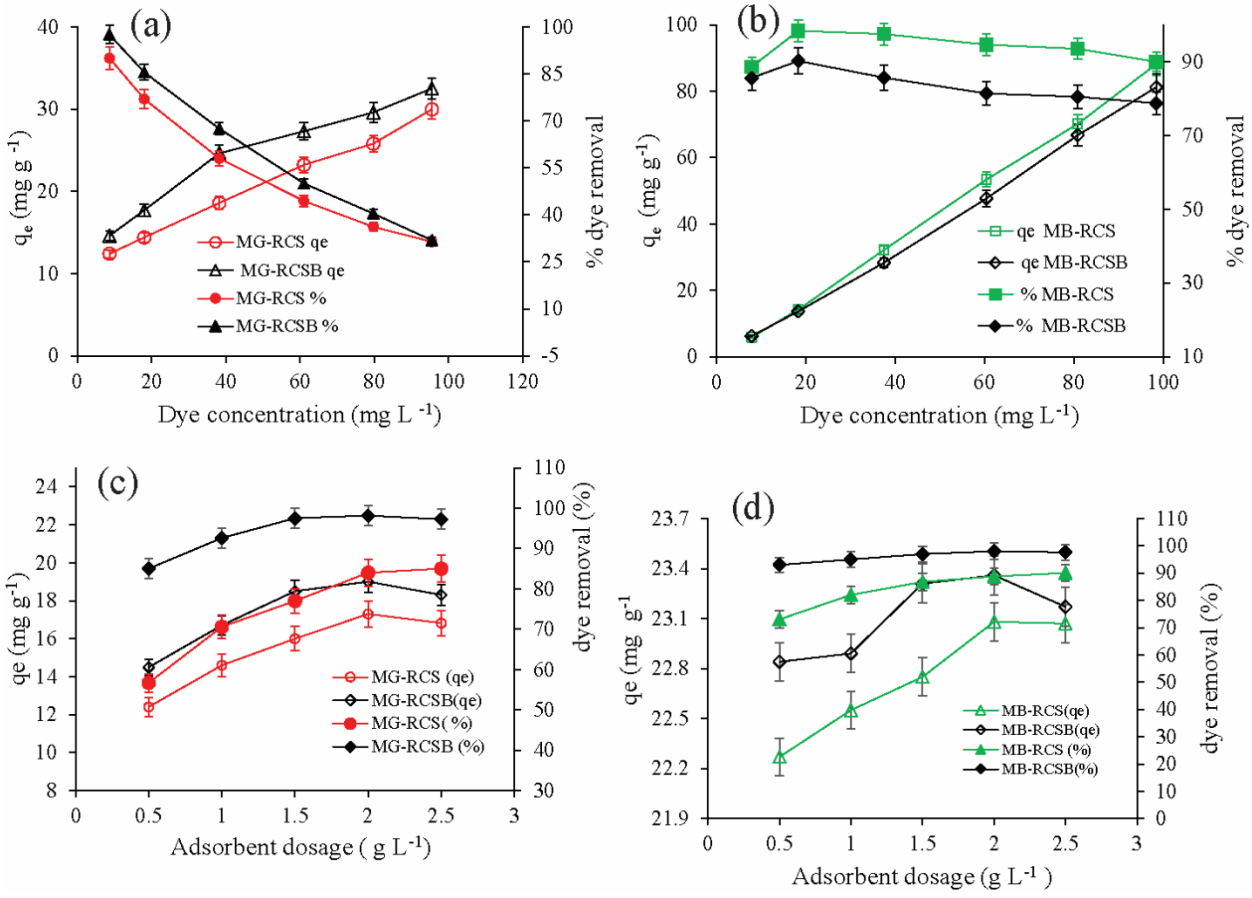

Figure 3.6 Effect of a–b initial dye concentration of MG, MB on RCS, RCSB, and c–d Adsorbent (RCS, RCSB) dosage on MG and MB dyes.

$gL^{-1,}$ and the curve comes to equilibrium after 1.5 $g.L^{-1}$ (RCSB) and 2.5 $g.L^{-1}$ (RCS) which is due to the saturation of the adsorption sites, with adsorbate. At equilibrium, the sorption efficiency remains unaltered due to the unavailability of sites for the adsorption of dye molecules. An optimum dose of 1.5 $g.L^{-1}$ for RCSB and 2.5 $g.L^{-1}$ for RCS has been considered for further adsorption studies. The adsorption capacity has an inverse relationship with the adsorbent dose. Therefore, the adsorbent capacity decrease decreases with an increase in the adsorbent dose.

3.3.2 Effect of solution pH on dye adsorption

The effect of solution pH on dye adsorption depends on the dye's nature and the adsorbent's surface chemistry. In general, the pH of the solution can influence the ionization state of both the dye molecules and the functional groups on the surface of the adsorbent, which can, in turn, affect the electrostatic interaction between them.

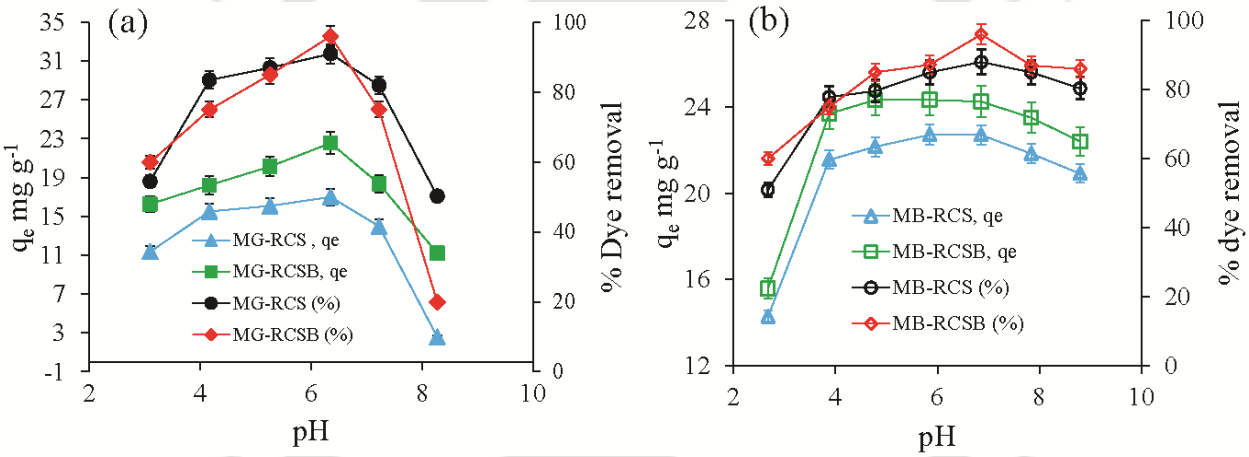

Figure 3.7 Effect of solution pH on dye removal (%), adsorption capacity (q_e, mg g^{-1}) of MG (a) and MB (b) on RCS, RCSB surface.

The effect of solution pH on the adsorption of dyes (MB, MG) was studied with varying pH (3-9) at an optimum dose of RCS and RCSB 20 mg/L working concentration. The results are depicted in Figure 3.7 (a,b). The adsorption capacity increases with pH increase; optimum adsorption was achieved at pH 6.3 for MG and 6.9 for MB and decreases after pH 7.5. Both biosorbents show good adsorption capacity in the pH range of 6.3-6.9. The extent of adsorption decreases below pH 4 and above pH 8 in the case of both biosorbents. Therefore, all the subsequent experiments were carried out at this pH range. The adsorption capacity of dyes can be described based on the adsorbate's pKa value and the adsorbent's pHpzc. pK_a values of MG and MB were reported as 6.9 and 5.8, respectively

[3.43], [3.44], due to which there is a possible existence of dye in the cationic form at pH>pKa and anionic form at pH<pK_a [3.5]. An increase in solution pH negatively charged adsorbent surface binds with the cationic dye molecules due to electrostatic attraction. At an acidic pH value, adsorption of dye shows lower adsorption, where cationic dyes compete with excess H^+ ions present in the dye solution [3.45].

3.3.3 Effect of initial dye concentration of MG and MB

The initial dye concentration is a significant factor in effectively removing dyes from wastewater [3.46]. Equilibrium studies were conducted with initial dye concentration from 10 mg L^{-1} to 100 mg L^{-1} at 298K, stirring speed 200 rpm, pH=6.3 for MG, pH=6.9 for MB, and contact time 120 min. Figure 3.6(a-b) depicts the effect of MG and MB dye concentrations on RCS and RCSB surfaces. After increasing the dye concentration, q_e increases from ~7 to ~30 mg $g^{-1.}$ The percentage of dye removal decreases from ~ 83% to ~31% and ~76 % to ~31% in the case of MG-RCS and MG-RCSB, respectively. However, in the case of MB dye, the adsorption capacity (q_e) and percentage of dye removal increase slowly with dye concentration. At higher dye concentrations, the surface of the adsorbents is saturated, and there are no available vacant sites for accommodating dye molecules. Hence dye removal (%) decreases with an increase in dye concentration [3.47]. However, in the case of adsorption capacity (q_e), its value increases with an increase in initial dye concentration because the interaction between the dye molecule and adsorbent rises with an increase in initial dye concentration [3.48].

3.3.4 Adsorption kinetics studies for MG and MB.

Kinetics studies were carried out at different time intervals using the nonlinear regression method of kinetics models to know the adsorption mechanism of dyes. The adsorption capacities obtained at various contact times were used to determine the nonlinear pseudo-first and pseudo-second order. Furthermore, intraparticle diffusion kinetic models were also studied. The non-linearized form of the pseudo-first-order, Eq. 3, nonlinear pseudo-second-order, Eq. 4, and intraparticle diffusion equations are given below Eq. 5 [3.49]

$$q_t = q_e(1 - exp(-k_1 t)) \quad (3)$$

$$q_t = \frac{{q_e}^2 K_2 t}{q_e K_2 t + 1} \quad (4)$$

Intraparticle diffusion is the most widely applied intraparticle diffusion equation for adsorption systems given by Weber and Morris [3.50]

$$q_t = k_i t^{\frac{1}{2}} + C \quad (5)$$

Where q_t (mg g^{-1}) and q_e(mg g^{-1}) are adsorption capacity at time t and equilibrium state respectively, K_1(g/(mg. min)) and K_2 (g/(mg. min)) and K_i (g/(mg.$min^{1/2}$)) are first order, second order, and intraparticle diffusion rate constants respectively. The equations' experimental and fitted linear regression coefficient (R^2) indicates the model's fitness.

Adsorption experiments were conducted at 30°C for both cationic dyes to know the equilibrium time. The kinetic experiments were conducted with an adsorbent dosage starting from 20 mg.L^{-1} at an initial dye concentration of 20 mg.L^{-1}. Contact time is one of the main parameters that influence the adsorption process. Figure A3.6 illustrates the sorption capacity of MG, MB by RCS, and RCSB at different contact times (20,40,60,80, and 100 mg.L^{-1}) and different initial MG and MB concentrations (20-100 mg.L^{-1}). It has been noticed that during the first 60 min, the dye adsorption process is much fast, and after that, its rate is slower, which may be due to the saturation of almost all the vacant adsorption sites after 60 min. The equilibrium stage was reached within 120 min with different dye concentrations from 20-100 mg.L^{-1}. After 120 min, no further increase in the adsorption capacity was observed, possibly due to repulsion between the dye molecules on the adsorbents and in bulk [3.51]**.** The kinetics data analysis has been done with pseudo-first-order (PFO), pseudo-second-order (PSO), and weber and morris intraparticle diffusion models. The nonlinear Pseudo-second order kinetic

Table 3.1 Non-linear kinetics parameters for pseudo-first-order, pseudo-second-order, and intraparticle diffusion

Model	**Kinetic parameters**	**RCS**		**RCSB**	
		MG	**MB**	**MG**	**MB**
Pseudo-first order	q_e	16.051	19.36	16.51	20.03
	K_1(L min^{-1})	0.018	0.019	0.055	0.001
	R^2	0.774	0.804	0.0794	0.91
Pseudo-second order	q_e	18.29	20.38	19.91	22.49
	K_2 (g $mg^{-1}min^{-1}$)	0.004	0.006	0.005	0.005
	R^2	0.918	0.913	0.916	0.902
Intraparticle diffusion	C	11.49	14.65	13.59	16.03
	K_i (mg g^{-1} $min^{-0.5}$)	0.094	0.077	0.083	0.091
	R^2	1	1	1	1

model curve fits were plotted for both dyes (Fig.3.8a-d). The correlation coefficients (R^2) and kinetic rate constant (k) values for three non-linearized forms of kinetic models were calculated (Table 3.1). The adsorption of both cationic dyes followed the pseudo-second-order kinetic model, as evident from a higher correlation coefficient (R^2) value compared to other kinetic models. The intraparticle

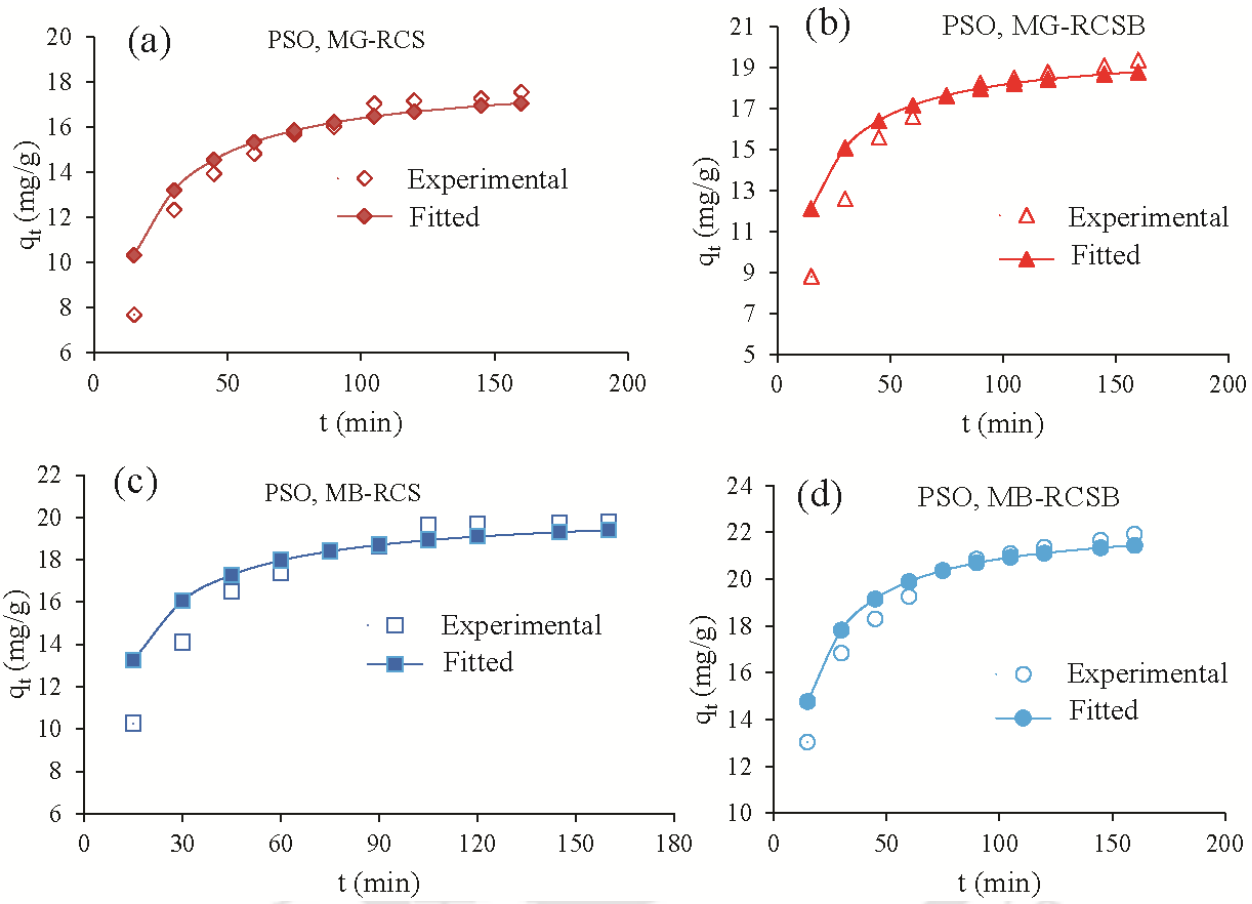

Figure 3.8. Nonlinear Pseudo-second order kinetics plot of (a) MG-RCS, (b) MG-RCSB, (c) MB-RCS, and (d) MB-RCSB

diffusion has been observed in a two-phase process. Phase I involves rapidly diffusing from the bulk solution to the surface-active sites. In phase II, slow diffusion of the dye molecules occurs from the surface sites to the inner pores of the biosorbent. The small value of the intraparticle diffusion rate constant in phase II (K_i = 0.077-0.094) is attributed to the slow diffusion of the MB and MG dyes until the equilibrium is attained [3.52]

3.3.5 Adsorption isotherm for MG and MB

The adsorption isotherm was studied by changing the initial dye concentration (10-100 $mg.L^{-1}$), keeping the adsorbent dose constant at 1.5 $g.L^{-1}$.The amount of dye (MB, MG) adsorbed at equilibrium was calculated from below equation 6.

$$q_e = \frac{(C_o - C_e)V}{m} \quad (6)$$

Where q_e is the equilibrium adsorption capacity($mg.g^{-1}$), C_o and C_e are the initial and equilibrium dye concentration in mg L^{-1}; V is the volume of dye solution (L), and m is the amount (g) of the adsorbent. The sorption isotherm refers to the relation between the equilibrium concentration of adsorbate in bulk and adsorbed amount of surface [3.53]. Knowing the parameters involved in the adsorbate-adsorbent interaction is essential for designing a preferred sorption system. The adsorbent surface may be considered a monolayer or multilayer. Several isotherm models have been applied to fit the experimental data and evaluate the applicability to MG and MB dye adsorption. Among them, Langmuir and Freundlich's isotherms are considered in this study.

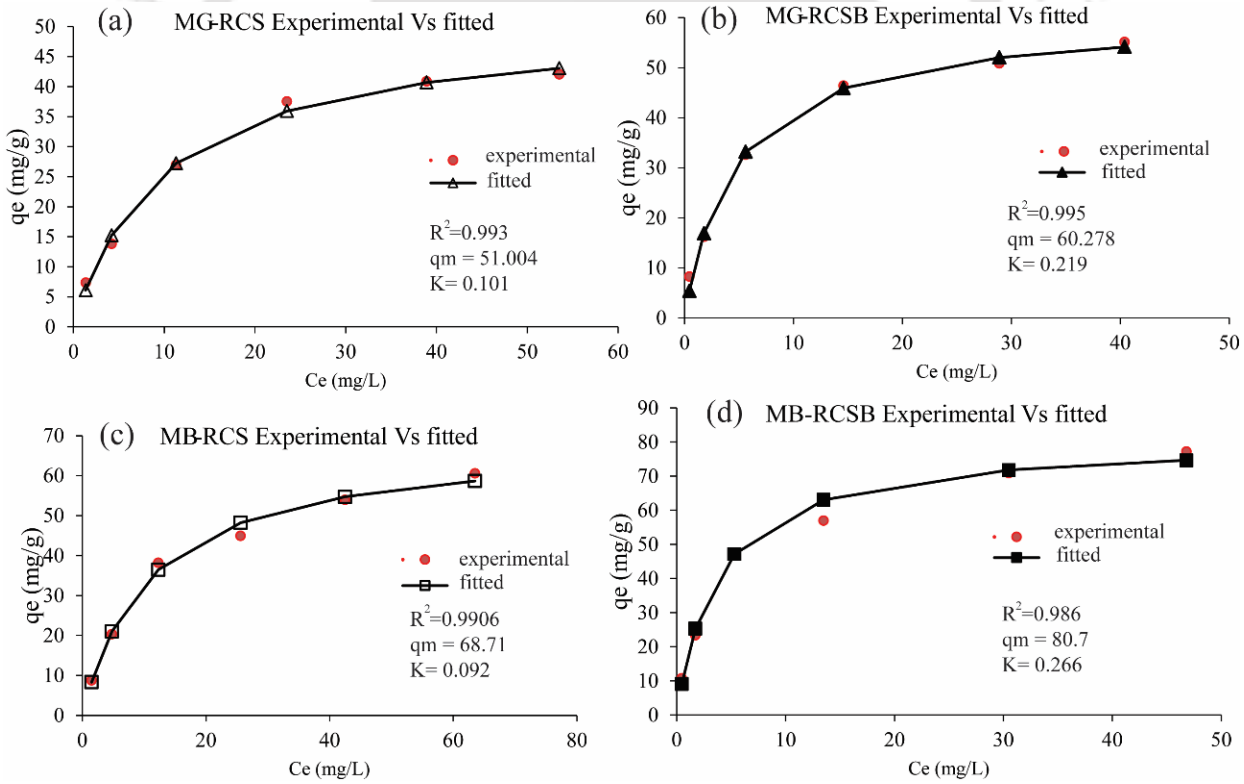

Figure 3.9 Nonlinear Langmuir isotherm plot for (a) MG-RCS, (b) MG-RCSB, (c) MB-RCS, and (d) MB-RCSB

Table 3.2 Nonlinear adsorption isotherm parameters for Langmuir and Freundlich

Isotherm model	Kinetic parameters	RCS		RCSB	
		MG	MB	MG	MB
Langmuir Isotherm	q_m (mg. g^{-1})	51.004	68.71	60.27	80.7
	K_L (L. mg^{-1})	0.111	0.092	0.291	0.266
	R^2	0.993	0.990	0.995	0.986
	R_L	0.35	0.69	0.71	0.68
Freundlich Isotherm	n	2.5	2.47	2.87	3.02
	K_F	9.26	11.75	16.03	22.72
	R^2	0.898	0.906	0.889	0.928

The Langmuir model assumes that monolayer adsorption occurs on a surface with a finite number of identical sites. All the sites are energetically equivalent, and there is no interaction between the adsorbed molecules. The nonlinear Langmuir equation is given by Eq. (6) [3.49].

$$q_e = \frac{q_m K_L C_e}{1+K_L C_e} \quad (6)$$

Where C_e (mg L^{-1}) is the equilibrium concentration of adsorbate, q_e (mg g^{-1}) is the adsorbent amount per unit mass. q_m is the maximum monolayer uptake by the adsorbent, and K_L (L mg^{-1}) is the Langmuir constant reflecting the free energy of adsorption (mg L^{-1}). The slope and the intercept of the linear plot of q_e vs. C_e give the value of K_L and q_m, respectively. The Langmuir model assumes monolayer adsorption and suggests a chemisorption process with uniform active sites for dye removal. To explain the favourability of dye adsorption, a dimensionless separation factor R_L of Langmuir isotherm was determined, which can be defined by Eq. 7.

$$R_L = \frac{1}{1+K_L C_o} \quad (7)$$

K_L is the Langmuir constant, and Co is the initial dye concentration, respectively, where R< 1 suggests favorable adsorption and R_L>1 means unfavorable adsorption.

The Freundlich isotherm is an empirical equation derived by assuming that the adsorption process takes place on the heterogeneous surface through a multilayer adsorption mechanism and that adsorption capacity is related to the concentration of Dye at Equilibrium [3.54]. The Freundlich equation is expressed in a nonlinear form, as shown in Eq. (8), [3.49]

$$q_e = K_F C_e^{\frac{1}{n}} \quad (8)$$

K_F in the above equation denotes the Freundlich constant related to bonding energy, and n represents the surface heterogeneity factor indicating adsorption intensity. The K_F is Freundlich's reaction rate constant, and 1/n(dimensionless) is the affinity of adsorption.

Isotherm studies play a significant role in determining the nature of the adsorption mechanism between the biosorbent and dye molecules. The nonlinear adsorption isotherm plot for Langmuir and Freundlich models has been shown in Figures 3.9 and A3.5. The nonlinear plot of specific sorption (q_e vs. C_e) against the equilibrium concentration denotes all the sorption of MG-RCS, MG-RCSB, MB-RCS, and MB-RCSB follows the Langmuir isotherm with the highest correlation coefficient (R^2 > 0.99). The Langmuir model assumes monolayer adsorption with homogeneous uniform surface active sites for MB and MG removal. The monolayer adsorption suggests a chemisorption process [3.55] which is clear from the higher correlation coefficient (R^2) value. The maximum dye adsorption capacity (q_m) was calculated and is close to the experimentally obtained value, depicted in Table 3.2. To explain the favourability of the dye adsorption, the dimensionless factor R_L has been calculated, and its value suggests a favorable adsorption process (R_L<1).

3.3.6 Thermodynamics studies for MG and MB

The extent of adsorption depends on the temperature of the solid-liquid interface. Adsorption at different temperatures gives the adsorption system feasibility, exhibiting the adsorption's thermodynamic characteristics. Thermodynamic parameters such as Gibbs free energy (ΔG˚, kJ mol^{-1}), enthalpy change (ΔH˚ kJ mol^{-1}), and entropy change (ΔS˚ J mol^{-1}) were determined by using Van't Hoff equation as

$$lnk_d = \frac{\Delta S^o}{R} - \frac{\Delta H^o}{RT} \quad (9)$$

$$\Delta G^\circ = -RT\ln(k_d) \quad (10)$$

Where K_d is the thermodynamic equilibrium constant (mol^{-1}) defined by Q_e/C_e **,** Qe is the dye concentration on the adsorbent at equilibrium, and Ce is the remaining dye concentration in the solution**.** R is the universal gas constant (8.314 J mol^{-1} K^{-1}), and T is the temperature in Kelvin**.**

The following eq. (11) relates the Gibbs free energy change (ΔG°) with the enthalpy (ΔH°), entropy change (ΔS°), and temperature (T) of the adsorption study.

$$\Delta G^\circ = \Delta H^\circ - T\Delta S^\circ \quad (11)$$

The effect of solution temperature on the adsorption of MG and MB dyes using RCS and RCSB adsorbents was investigated at different temperature ranges (293 K to 323 K) to know the adsorption process. The value of ΔH˚ and ΔS˚ were selected from the slope (-ΔH˚/R) and intercept (ΔS˚/R) from the plot of ln (K_d) vs. 1/T (Van't Hoff plot) using Eq. (9) which is shown in Figure 3.10 (a). Gibbs free energy, ΔG˚ values were calculated using Eq. (10). Negative values of ΔH˚ suggest the exothermic nature of adsorption. Negative ΔS˚ values indicate the decrease in randomness at the solid-liquid interface. The negative ΔG˚ value indicates that the adsorption of dyes on RCS and RCSB adsorbents is feasible and spontaneous. It was shown in a previous study that if the value of ΔG˚ comes in between 0 and -20, $kJmol^{-1}$ is a sign of physical adsorption, and if the value comes between -80 and -400 kJ mol^{-1}, then chemical adsorption. There is a decrease in the adsorption of MG and MB on the RCS and RCSB surface with an increase in solution temperature at optimum reaction conditions, indicating that the adsorption process is exothermic. With the temperature rise, the adsorption capacity of MG and MB dye on RCS and RCSB decreases, which suggests the adsorption process is favorable at a lower temperature. This may be due to the dye molecule's tendency to escape from the solid adsorbent surface to the solution phase with an increase in the temperature of the solution. The thermodynamic parameters determined at a temperature range are summarized in Table 3.3. The ΔS˚ and ΔH˚ values can be calculated by plotting the graph between lnKc vs. 1/T, indicating a decrease in randomness at the solid-solution interface and exothermic nature shown by both dyes MB and MG on RCS and RCSB surface.

The desorption efficiency of dyes on RCS & RCSB surfaces was done in five cycles, as shown in Figure 3.10 (b)

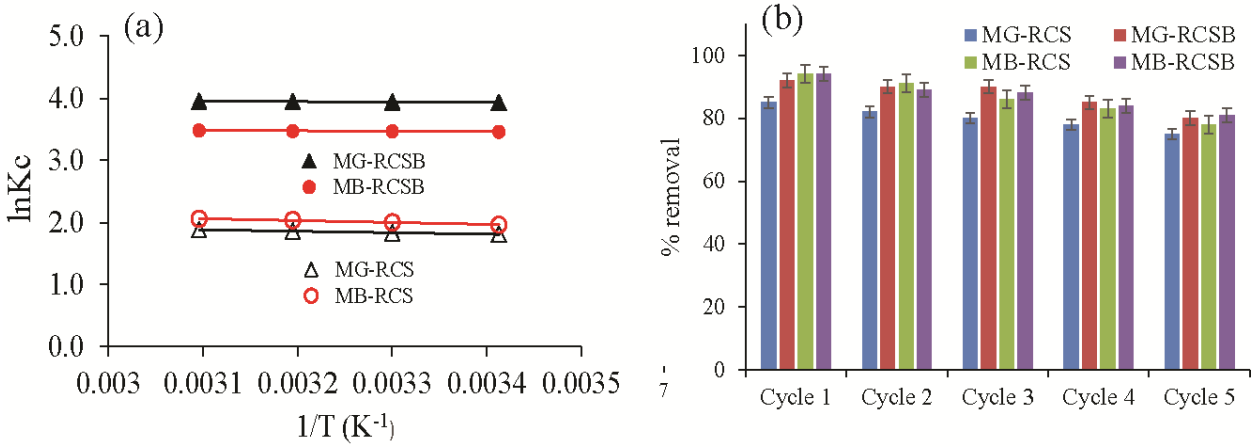

Figure 3.10 (a)Van't Hoff plot of ln(K_d) vs. 1/T and (b) desorption cycle

Table 3.3 Different thermodynamic parameters

Adsorbent	Temp (K)	Methylene Blue (MB)			Malachite Green (MG)		
		ΔG° KJ mol^{-1}	ΔH° KJ mol^{-1}	ΔS° J K^{-1} mol^{-1}	ΔG° KJ mol^{-1}	ΔH° KJ mol^{-1}	ΔS° J K^{-1} mol^{-1}
RCS	293	-4.7816	2.5936	25.1889	-4.4090	1.9712	21.7636
	303	-5.0415			-4.6165		
	333	-5.3017			-4.8428		
	323	-5.5333			-5.0594		
RCSB	293	-8.4342	0.5729	30.7335	-9.5837	0.7469	28.2884
	303	-8.7367			-9.9264		
	333	-9.0455			-10.2712		
	323	-9.3560			-10.6118		

3.3.7 Adsorption Mechanism for dye removal

The mechanism of cationic dye removal using raw and activated biochar involves electrostatic interaction between the positively charged dye molecules and negatively charged surface functional groups of the raw and activated biochar. This process is influenced by pH, contact time, and initial dye concentration. Our present study's experiments confirm that RCS and RCSB biosorbents were adequate for the preferential adsorption of cationic dyes MG and MB. Kinetics, isotherm, and thermodynamics data reveal that adsorption was by both physical adsorption and chemisorption. Chemisorption is achieved by the substantial sharing of electrons between the surface of the adsorbent and adsorbate to create a covalent or ionic bond, as the surface charge of biosorbent was found to be negatively charged.

In contrast, the dyes (MB and MG) were positively charged. Thus these dyes are readily adsorbed due to electrostatic interaction and ion exchange mechanism on the biosorbent surface. From the kinetics data, intraparticle diffusion is the rate-limiting step controlling adsorption. The intraparticle diffusion has been observed in a two-phase process. Phase I rapidly diffuses the MG and MB dye from the bulk solution to the surface-active sites/pores on the RCS and RCSB. In phase II, slow diffusion of the dye molecules occurs from the surface sites to the inner pores of the RCS, RCSB biosorbent. The surface area data of RCS and RCSB has various macropores and mesopores. The specific surface area, pore volume, and pore diameter were found to be 0.963 m^2/g,0.006 cc/g,16.149 Å for RCS and 11.786 m^2/g, 0.048 cc/g, and 3.616 nm for RCSB respectively. The dyes are diffused in these pores, making

them physical adsorption in nature. The adsorption mechanism of various organic pollutants by biochar in the aqueous medium is shown in Table 3.4. FTIR analysis shows functional groups C=O and –OH is present on the biosorbent surface, which plays a vital role in dye adsorption. From the thermodynamic study, ΔG° data shows that the adsorption process for all four systems was chemisorption nature, spontaneous, and favored at temperatures 293K to 303K.

3.3.8 Desorption and regeneration studies

It is crucial to regenerate the biosorbent material to make the process more cost-effective; accordingly, desorption studies were carried out. Similarly, this desorption study allows looking at mechanical aspects of the solute transfer process [3.60]. Experiments for desorption were carried out to investigate the possibility of regeneration and recycling of both adsorbents. 100 mg loaded dried adsorbent was

Table 3.4: Adsorptive removal mechanisms of various organic pollutants by biochar in the aqueous medium

Adsorbent	Biochar feedstock	Adsorption mechanism	Reference
Brilliant blue	Rice and wheat straw	Electrostatic attraction and intermolecular hydrogen bonds	[3.56]
Tetracycline	Rice husk	π–π interaction	[3.57]
Basic red 09	Coconut shell	Electrostatic attraction	[3.58]
Basic Blue 41	Rice husk	Electrostatic interaction	[3.59]

agitated (200 rpm) with 30 ml dye solution (298 K, pH 6.3 for MG and 6.9 for MB) for two hours. The mixture was centrifuged, filtered, and analyzed for the remaining dye concentration. The RCS and RCSB-loaded sorbents were collected and gently washed to remove unadsorbed material with double distilled water. The MB & MG dye-loaded RCS & RCSB biosorbents were separated from the dye solution by centrifugation and dried. The spent adsorbents were then stirred with 40 ml of acidic solutions (deionized water, 0.1M HCl, and 0.1 M H_2SO_4), and concentrations of MG and MB were measured. The desorption efficiency can be calculated from the following equation: [3.61]

$$Desorption\ efficiency = \frac{Amount\ of\ dye\ desorbed\ (\text{mg/L})}{Amount\ of\ dye\ adsorbed\ (\text{mg/L})} \times 100 \quad (12)$$

Table 3.5 Various types of adsorbents with their adsorption capacity

Adsorbent	Dye	Adsorption capacity (mg/g)	pH	Intial dye concentration (mg/ L)	Reference
Peels of *Solanum tuberosum*	Emerald green dye	2.61	3	5	[3.62]
Peels of *Musa acuminate*	Emerald green dye	10.75	6	5	[3.62]
Cucumis sativus peels	Methylene blue dye	21.45	8	25	[3.63]
Powder of white potato peels	Methyl red dye	30.48	2	50	[3.64]
Ricinus communis epicarp	Malachite Green	27.78	7	20	[3.39]
Powder of banana peels	Reactive Black 5 dye	211.8	3	100	[3.61]
Fibers of banana pseudostem	Methyl red dye	88.5	3	50	[3.65]
Saraca asoca	Methylene blue dye	90.9	7	100	[3.66]
Ricinus communis Stem	MB-RCSB	80.7	7	20	**This work**
	MG-RCSB	60	6.3		
	MB-RCS	68.7	7		
	MG-RCS	51	6.3		

3.3.9 Comparative study of the adsorbent

The adsorption capacities of MG and MB were compared with other reported adsorbents in the literature and presented in Table 3.5 . The adsorption capacity of MG-RCSB is the highest among all the reported adsorbents. Thus, MG-RCSB is better for removing MG from its aqueous solutions than any other adsorbent.

3.3.10 Cost estimation of the activated biochar (RCSB & CESB)

The cost estimation of the activated biochar can be determined by comparing the cost of the adsorbent per gram of the adsorbate removed considering the chemical purchase cost, energy cost and adsorption capacity. The cost of an adsorbent per gram of adsorbate can be used to determine the cost of the adsorption as shown below [3.67]

$$\text{Adsorption Cost } (₹/g_{adsorbate}) = \frac{\text{Chemical Purchase cost } \left(\frac{₹}{g}\right) + \text{Energy Cost } \left(\frac{₹}{g}\right) \text{kwh}}{\text{Adsorption capacity } \left(\frac{mg}{g}\right) \times 10^{-3} \left(\frac{g}{mg}\right)}$$

Where adsorption capacity is the amount of adsorbate removed per gram adsorbent used in mg/g. This equation can used for large-scale industrial applications. The determination of adsorbent cost with few reference has been mentioned in table 3.6.

Table 3.6 : The cost of different biochar for treating wastewater.

Adsorbent name	**Target Pollutant**	**Adsorption capacity (mg/g)**	**Cost (₹/g)**	**Reference**
Rice husk biochar	Basic red 9	44	13	[3.68]
Coconut Shell Biochar	Basic red 9	10	58	[3.68]
Cherry kernels biochar	Pb (II)	94.48	4	[3.69]
Ricinus Communis Stem Biochar	Methylene Blue	80.7	33	This study
Colocasia Esculanta stem Biochar	Pb(II)	208.3	12	This study

3.4 Conclusion

This study has explored the adsorption of *Ricinus communis* stem-derived raw and activated biochar to remove preferentially two dyes among nine dyes. Both biosorbents RCS and RCSB show excellent cationic dye (MB and MG) removal capacity, up to ~88% and ~98%, respectively. The optimized pH for the adsorption process is pH 6.3 and 6.9 with a temperature of 313K to remove MG and MB dye using RCS and RCSB. The experimental and fitted isotherm parameters are mentioned in all the sorption of MG-RCS, MG-RCSB, MB-RCS, and MB-RCSB following the Langmuir isotherm with the highest correlation coefficient ($R^2 > 0.99$) and the highest q_m value 242 mg. g^{-1} for MG-RCSB. Langmuir separation factor R_L <1 suggests favorable adsorption. The Langmuir model assumes monolayer adsorption with homogeneous uniform surface active sites for MB and MG removal. Monolayer adsorption is a chemisorption process. The pseudo-second-order kinetics model for all adsorption systems described the adsorption kinetics with R^2 =0.99. The thermodynamics parameters indicate that the adsorption was spontaneous and exothermic, and ΔG° value suggests physical adsorption. Regeneration studies exhibited that RCS and RCSB could be effectively utilized for the recovery of MG and MB dye and reused of adsorbent up to five adsorption–desorption cycles. The synthesized biochar RCSB at 300°C exhibits higher adsorption efficiency and demonstrates advantages, including cost-effective and environmentally eco-friendly nature. Cost estimation shows

1 g RCSB production is 33 ₹ and 1 gm CESB production is 12₹. Further research is needed to evaluate the technical feasibility of using the technology for large wastewater treatment plants. Although adsorbent can be recycled in up to five cycles, its disposal is a matter of concern and challenge. Overall, using raw and activated biochar for cationic dye removal shows excellent promise as an environmentally friendly and cost-effective solution for wastewater treatment. Further research is needed to optimize the biochar application conditions and explore its potential for other types of pollutants.

References:

[3.1] S. Bansal, P.K. Pandey, S. Upadhayay, Methylene Blue Dye Removal from Wastewater Using Ailanthus Excelsa Roxb as Adsorbent, Water Conserv. Sci. Eng. 6 (2021) 1–9. https://doi.org/10.1007/s41101-020-00097-3.

[3.2] N.R.J. Hynes, J.S. Kumar, H. Kamyab, J.A.J. Sujana, O.A. Al-Khashman, Y. Kuslu, A. Ene, B. Suresh Kumar, Modern enabling techniques and adsorbents based dye removal with sustainability concerns in textile industrial sector -A comprehensive review, J. Clean. Prod. 272 (2020) 122636. https://doi.org/10.1016/j.jclepro.2020.122636.

[3.3] S. Sutar, P. Patil, J. Jadhav, Recent advances in biochar technology for textile dyes wastewater remediation: A review, Environ. Res. 209 (2022) 112841. https://doi.org/10.1016/J.ENVRES.2022.112841.

[3.4] H.Y. Zhu, R. Jiang, Y.Q. Fu, J.H. Jiang, L. Xiao, G.M. Zeng, Preparation, characterization and dye adsorption properties of γ-Fe2O3/SiO2/chitosan composite, Appl. Surf. Sci. 258 (2011) 1337–1344. https://doi.org/10.1016/j.apsusc.2011.09.045.

[3.5] H. Singh, G. Chauhan, A.K. Jain, S.K. Sharma, Adsorptive potential of agricultural wastes for removal of dyes from aqueous solutions, J. Environ. Chem. Eng. 5 (2017) 122–135. https://doi.org/10.1016/j.jece.2016.11.030.

[3.6] A. Mittal, J. Mittal, A. Malviya, D. Kaur, V.K. Gupta, Adsorption of hazardous dye crystal violet from wastewater by waste materials, J. Colloid Interface Sci. 343 (2010) 463–473. https://doi.org/10.1016/j.jcis.2009.11.060.

[3.7] Y. Dai, N. Zhang, C. Xing, Q. Cui, Q. Sun, The adsorption, regeneration, and engineering applications of biochar for removal organic pollutants: a review, Chemosphere. 223 (2019) 12–27.

[3.8] J. Aguilar-Rosero, M.E. Urbina-López, B.E. Rodríguez-González, S.X. León-Villegas, I.E. Luna-Cruz, D.L. Cárdenas-Chávez, Development and Characterization of Bioadsorbents Derived from Different Agricultural Wastes for Water Reclamation: A Review, Appl. Sci. 12 (2022). https://doi.org/10.3390/app12052740.

[3.9] F. Amalina, A.S.A. Razak, S. Krishnan, A.W. Zularisam, M. Nasrullah, Dyes removal from textile wastewater by agricultural waste as an absorbent – A review, Clean. Waste Syst. 3 (2022) 100051. https://doi.org/10.1016/j.clwas.2022.100051.

[3.10] D. Sud, G. Mahajan, M.P. Kaur, Agricultural waste material as potential adsorbent for sequestering

heavy metal ions from aqueous solutions - A review, Bioresour. Technol. 99 (2008) 6017–6027. https://doi.org/10.1016/j.biortech.2007.11.064.

[3.11] P. Sharma, H. Laddha, M. Agarwal, R. Gupta, Selective and effective adsorption of malachite green and methylene blue on a non-toxic, biodegradable, and reusable fenugreek galactomannan gum coupled MnO2 mesoporous hydrogel, Microporous Mesoporous Mater. 338 (2022) 111982. https://doi.org/10.1016/j.micromeso.2022.111982.

[3.12] G.Y. Abate, A.N. Alene, A.T. Habte, D.M. Getahun, Adsorptive removal of malachite green dye from aqueous solution onto activated carbon of Catha edulis stem as a low cost bio-adsorbent, Environ. Syst. Res. 9 (2020) 1–13.

[3.13] A. Liu, W. Zhou, K. Shen, J. Liu, X. Zhang, One-pot hydrothermal synthesis of hematite-reduced graphene oxide composites for efficient removal of malachite green from aqueous solution, RSC Adv. 5 (2015) 17336–17342. https://doi.org/10.1039/c4ra15589k.

[3.14] S.J. Culp, F.A. Beland, Malachite Green: A Toxicological Review, Int. J. Toxicol. 15 (1996) 219–238. https://doi.org/10.3109/10915819609008715.

[3.15] Z. liang CHEN, J. qiang ZHANG, L. HUANG, Z. hui YUAN, Z. jun LI, M. chao LIU, Removal of Cd and Pb with biochar made from dairy manure at low temperature, J. Integr. Agric. 18 (2019) 201–210. https://doi.org/10.1016/S2095-3119(18)61987-2.

[3.16] J. Zhang, J. Liu, R. Liu, Effects of pyrolysis temperature and heating time on biochar obtained from the pyrolysis of straw and lignosulfonate, Bioresour. Technol. 176 (2015) 288–291. https://doi.org/10.1016/j.biortech.2014.11.011.

[3.17] M. Safaei Khorram, Q. Zhang, D. Lin, Y. Zheng, H. Fang, Y. Yu, Biochar: A review of its impact on pesticide behavior in soil environments and its potential applications., J. Environ. Sci. (China). 44 (2016) 269–279. https://doi.org/10.1016/j.jes.2015.12.027.

[3.18] N. Zhao, X. Yang, J. Zhang, L. Zhu, Y. Lv, Adsorption Mechanisms of Dodecylbenzene Sulfonic Acid by Corn Straw and Poplar Leaf Biochars, Materials (Basel). 10 (2017). https://doi.org/10.3390/ma10101119.

[3.19] M. Ahmad, A.U. Rajapaksha, J.E. Lim, M. Zhang, N. Bolan, D. Mohan, M. Vithanage, S.S. Lee, Y.S. Ok, Biochar as a sorbent for contaminant management in soil and water: a review., Chemosphere. 99 (2014) 19–33. https://doi.org/10.1016/j.chemosphere.2013.10.071.

[3.20] M.A. Yahya, Z. Al-Qodah, C.W.Z. Ngah, Agricultural bio-waste materials as potential sustainable precursors used for activated carbon production: A review, Renew. Sustain. Energy Rev. 46 (2015) 218–235. https://doi.org/https://doi.org/10.1016/j.rser.2015.02.051.

[3.21] I. Ali, M. Asim, T.A. Khan, Low cost adsorbents for the removal of organic pollutants from wastewater., J. Environ. Manage. 113 (2012) 170–183. https://doi.org/10.1016/j.jenvman.2012.08.028.

[3.22] M. Jibril, J. Noraini, L.S. Poh, A.M. Evuti, Removal of colour from waste water using coconut shell activated carbon (CSAC) and commercial activated carbon (CAC), J. Teknol. (Sciences Eng. 60 (2013) 15–19. https://doi.org/10.11113/jt.v60.1435.

[3.23] A. Garba, H. Basri, N.S. Nasri, R. Isma'il, synthesis and characterization of porous carbon from biomass using KOH and K2CO3 chemical activation, ARPN J. Eng. Appl. Sci. 11 (2016) 1613–1617.

[3.24] I. Akkari, Z. Graba, N. Bezzi, M. Vithanage, M.M. Kaci, New insights into the effective removal of Basic Red 46 onto activated carbon produced from pomegranate peels, Biomass Convers. Biorefinery. (2022). https://doi.org/10.1007/s13399-022-03401-4.

[3.25] I. Akkari, Z. Graba, N. Bezzi, M.M. Kaci, F.A. Merzeg, N. Bait, A. Ferhati, G.L. Dotto, Y. Benguerba,

Effective removal of cationic dye on activated carbon made from cactus fruit peels: a combined experimental and theoretical study, Environ. Sci. Pollut. Res. (2022) 3027–3044. https://doi.org/10.1007/s11356-022-22402-4.

[3.26] Z. Graba, I. Akkari, N. Bezzi, M.M. Kaci, Valorization of olive–pomace as a green sorbent to remove Basic Red 46 (BR46) dye from aqueous solution, Biomass Convers. Biorefinery. 46 (2022). https://doi.org/10.1007/s13399-022-03639-y.

[3.27] F. Atmani, M.M. Kaci, N. Yeddou-Mezenner, A. Soukeur, I. Akkari, J.A. Navio, Insights into the physicochemical properties of Sugar Scum as a sustainable biosorbent derived from sugar refinery waste for efficient cationic dye removal, Biomass Convers. Biorefinery. (2022). https://doi.org/10.1007/s13399-022-02646-3.

[3.28] D. Tulu, M. Aleme, G. Mengistu, A. Bogale, K. Shifa, E. Mendesil, Evaluation of Castor (Ricinus communis L.) Genotypes and Their Feeding Values on Rearing Performance of Eri Silkworm (Samia cynthia ricini Boisduval) (Lepidoptera: Saturniidae) in Southwest Ethiopia, Psyche J. Entomol. 2022 (2022). https://doi.org/10.1155/2022/1556776.

[3.29] O.Y. Saribiyik, M. Özcanli, H. Serin, S. Serin, K. Aydin, Biodiesel production from ricinus communis oil and its blends with soybean biodiesel, Stroj. Vestnik/Journal Mech. Eng. 56 (2010) 811–816. https://doi.org/10.5545/sv-jme.2009.054.

[3.30] F.K. Yuen, B.H. Hameed, Recent developments in the preparation and regeneration of activated carbons by microwaves, Adv. Colloid Interface Sci. 149 (2009) 19–27.

[3.31] M. Li, H. Liu, T. Chen, C. Dong, Y. Sun, Synthesis of magnetic biochar composites for enhanced uranium(VI) adsorption, Sci. Total Environ. 651 (2019) 1020–1028. https://doi.org/10.1016/J.SCITOTENV.2018.09.259.

[3.32] F. Yuan, S. Li, Z. Fan, X. Meng, L. Fan, S. Yang, Shining carbon dots: Synthesis and biomedical and optoelectronic applications, Nano Today. 11 (2016) 565–586.

[3.33] F. Dowell, D. Wang, F. Xu, J. Yu, T. Tesso, F. Dowell, D. Wang, Qualitative and quantitative analysis of lignocellulosic biomass using infrared techniques : A, Appl. Energy. 104 (2013) 801–809. https://doi.org/10.1016/j.apenergy.2012.12.019.

[3.34] M. Brebu, C. Vasile, Thermal degradation of lignin—a review, Cellul. Chem. \& Technol. 44 (2010) 353.

[3.35] G.-H. Oh, C.-H. Yun, C.-R. Park, Role of KOH in the one-stage KOH activation of cellulosic biomass, Carbon Lett. 4 (2003) 180–184.

[3.36] X.F. Sun, R.C. Sun, P. Fowler, M.S. Baird, Isolation and characterisation of cellulose obtained by a two-stage treatment with organosolv and cyanamide activated hydrogen peroxide from wheat straw, Carbohydr. Polym. 55 (2004) 379–391.

[3.37] C. Mu, M. Jiang, J. Zhu, M. Zhao, S. Zhu, Z. Zhou, Isolation of cellulose from steam-exploded rice straw with aniline catalyzing dimethyl formamide aqueous solution, Renew. Energy. 63 (2014) 324–329.

[3.38] W. Xie, H. Peng, L. Chen, Transesterification of soybean oil catalyzed by potassium loaded on alumina as a solid-base catalyst, Appl. Catal. A Gen. 300 (2006) 67–74.

[3.39] T. Santhi, S. Manonmani, T. Smitha, Removal of malachite green from aqueous solution by activated carbon prepared from the epicarp of Ricinus communis by adsorption, J. Hazard. Mater. (2010). https://doi.org/10.1016/j.jhazmat.2010.02.076.

[3.40] M. Karatas, Removal of Pb (II) from water by natural zeolitic tuff: kinetics and thermodynamics, J.

Hazard. Mater. 199 (2012) 383–389.
[3.41] W. Wei, Q. Wang, A. Li, J. Yang, F. Ma, S. Pi, D. Wu, Biosorption of Pb (II) from aqueous solution by extracellular polymeric substances extracted from Klebsiella sp. J1: Adsorption behavior and mechanism assessment, Sci. Rep. 6 (2016) 1–10. https://doi.org/10.1038/srep31575.
[3.42] A. Kumar, B. Prasad, I.M. Mishra, Adsorptive removal of acrylonitrile by commercial grade activated carbon: Kinetics, equilibrium and thermodynamics, J. Hazard. Mater. 152 (2008) 589–600. https://doi.org/10.1016/j.jhazmat.2007.07.048.
[3.43] S. Banerjee, R.K. Gautam, A. Jaiswal, P.K. Gautam, M.C. Chattopadhyaya, Study on adsorption behavior of Acid Orange 10 onto modified wheat husk, Desalin. Water Treat. 57 (2016) 12302–12315. https://doi.org/10.1080/19443994.2015.1046151.
[3.44] G.A.P. M. Oz, D.E. Lorke, M. Hasan, Cellular and molecular actions of methylene blue in the nervous system, Med. Res. Rev. 31 (2011) 93–117.
[3.45] C.F. Iscen, I. Kiran, S. Ilhan, Biosorption of Reactive Black 5 dye by Penicillium restrictum: The kinetic study, J. Hazard. Mater. 143 (2007) 335–340. https://doi.org/https://doi.org/10.1016/j.jhazmat.2006.09.028.
[3.46] S. Chakraborty, S. Chowdhury, P. Das Saha, Adsorption of Crystal Violet from aqueous solution onto NaOH-modified rice husk, Carbohydr. Polym. 86 (2011) 1533–1541. https://doi.org/10.1016/j.carbpol.2011.06.058.
[3.47] S.L. C.F. Iscen, I. Krian, Biosorption of reactive blacks dyes by Fenicilliumrestrictum: the kinetic study, J. Hazard. Mater. 143 (2007) 335–338.
[3.48] A. Thakur, H. Kaur, Response surface optimization of Rhodamine B dye removal using paper industry waste as adsorbent, Int. J. Ind. Chem. 8 (2017) 175–186. https://doi.org/10.1007/s40090-017-0113-4.
[3.49] A.R.P. Hidayat, D.O. Sulistiono, I.K. Murwani, B.F. Endrawati, H. Fansuri, L.L. Zulfa, R. Ediati, Linear and nonlinear isotherm, kinetic and thermodynamic behavior of methyl orange adsorption using modulated Al2O3@UiO-66 via acetic acid, J. Environ. Chem. Eng. 9 (2021) 106675. https://doi.org/10.1016/j.jece.2021.106675.
[3.50] W.J. Weber Jr, J.C. Morris, Kinetics of adsorption on carbon from solution, J. Sanit. Eng. Div. 89 (1963) 31–59.
[3.51] S. Dawood, T.K. Sen, C. Phan, Adsorption removal of Methylene Blue (MB) dye from aqueous solution by bio-char prepared from Eucalyptus sheathiana bark: kinetic, equilibrium, mechanism, thermodynamic and process design, Desalin. Water Treat. 3994 (2016) 1–17. https://doi.org/10.1080/19443994.2016.1188732.
[3.52] H. Atallah, M.El. Mahmoud, A. Jelle, A. Lough, M. Hmadeh, A highly stable indium based metal organic framework for efficient arsenic removal from water, Dalt. Trans. 47 (2018) 799–806.
[3.53] H. Zheng, D. Liu, Y. Zheng, S. Liang, Z. Liu, Sorption isotherm and kinetic modeling of aniline on Cr-bentonite, J. Hazard. Mater. 167 (2009) 141–147. https://doi.org/10.1016/j.jhazmat.2008.12.093.
[3.54] H. Freundlich, Over the adsorption in solution, J. Phys. Chem. 57 (1906) 1100–1107.
[3.55] H. Cai, L. Xu, G. Chen, C. Peng, F. Ke, Z. Liu, D. Li, Z. Zhang, X. Wan, Removal of fluoride from drinking water using modified ultrafine tea powder processed using a ball-mill, Appl. Surf. Sci. 375 (2016) 74–84.
[3.56] Y. Qiu, Z. Zheng, Z. Zhou, G.D. Sheng, Effectiveness and mechanisms of dye adsorption on a straw-based biochar., Bioresour. Technol. 100 (2009) 5348–5351. https://doi.org/10.1016/j.biortech.2009.05.054.

[3.57] P. Liu, W.-J. Liu, H. Jiang, J.-J. Chen, W.-W. Li, H.-Q. Yu, Modification of bio-char derived from fast pyrolysis of biomass and its application in removal of tetracycline from aqueous solution., Bioresour. Technol. 121 (2012) 235–240. https://doi.org/10.1016/j.biortech.2012.06.085.

[3.58] P. Saravanan, B.P. Thillainayagam, G. Ravindiran, J. Josephraj, Evaluation of the adsorption capacity of Cocos Nucifera shell derived biochar for basic dyes sequestration from aqueous solution, Energy Sources, Part A Recover. Util. Environ. Eff. 00 (2020) 1–17. https://doi.org/10.1080/15567036.2020.1800142.

[3.59] J. Jegan, S. Praveen, T.B. Pushpa, R. Gokulan, Biodecolorization of basic violet 03 using biochar derived from agricultural wastes: isotherm and kinetics, J. Biobased Mater. Bioenergy. 14 (2020) 316–326.

[3.60] R. Lakshmipathy, N.C. Sarada, Adsorptive removal of basic cationic dyes from aqueous solution by chemically protonated watermelon (Citrullus lanatus) rind biomass, Desalin. Water Treat. 52 (2014) 6175–6184. https://doi.org/10.1080/19443994.2013.812526.

[3.61] V.S. Munagapati, J.C. Wen, C.L. Pan, Y. Gutha, J.H. Wen, G.M. Reddy, Adsorptive removal of anionic dye (Reactive Black 5) from aqueous solution using chemically modified banana peel powder: kinetic, isotherm, thermodynamic, and reusability studies, Int. J. Phytoremediation. 22 (2020) 267–278. https://doi.org/10.1080/15226514.2019.1658709.

[3.62] R. Rehman, S. Farooq, T. Mahmud, Use of Agro-waste Musa acuminata and Solanum tuberosum peels for economical sorptive removal of Emerald green dye in ecofriendly way, J. Clean. Prod. 206 (2019) 819–826. https://doi.org/10.1016/J.JCLEPRO.2018.09.226.

[3.63] S. Shakoor, A. Nasar, Adsorptive treatment of hazardous methylene blue dye from artificially contaminated water using cucumis sativus peel waste as a low-cost adsorbent, Groundw. Sustain. Dev. 5 (2017) 152–159. https://doi.org/10.1016/J.GSD.2017.06.005.

[3.64] C.K. Enenebeaku, N.J. Okorocha, U.E. Enenebeaku, I.C. Ukaga, Adsorption and Equilibrium Studies on the Removal of Methyl Red from Aqueous Solution Using White Potato Peel Powder, Int. Lett. Chem. Phys. Astron. 72 (2017) 52–64. https://doi.org/10.18052/www.scipress.com/ILCPA.72.52.

[3.65] M.R.H. Mas Haris, K. Sathasivam, The removal of methyl red from aqueous solutions using banana pseudostem fibers, Am. J. Appl. Sci. 6 (2009) 1690–1700. https://doi.org/10.3844/ajassp.2009.1690.1700.

[3.66] L. Cavas, Z. Karabay, H. Alyuruk, H. Do\ugan, G.K. Demir, Thomas and artificial neural network models for the fixed-bed adsorption of methylene blue by a beach waste Posidonia oceanica (L.) dead leaves, Chem. Eng. J. 171 (2011) 557–562.

[3.67] Ighalo, J. O., Omoarukhe, F. O., Ojukwu, V. E., Iwuozor, K. O., & Igwegbe, C. A. (2022). Cost of adsorbent preparation and usage in wastewater treatment: a review. Cleaner Chemical Engineering, 100042.

[3.68] Praveen, S., Gokulan, R., Pushpa, T. B., & Jegan, J. (2021). Techno-economic feasibility of biochar as biosorbent for basic dye sequestration. Journal of the Indian Chemical Society, 98(8), 100107.

[3.69] Vukelic, D., Boskovic, N., Agarski, B., Radonic, J., Budak, I., Pap, S., & Sekulic, M. T. (2018). Eco-design of a low-cost adsorbent produced from waste cherry kernels. Journal of Cleaner Production, 174, 1620-1628.

Annexure-3

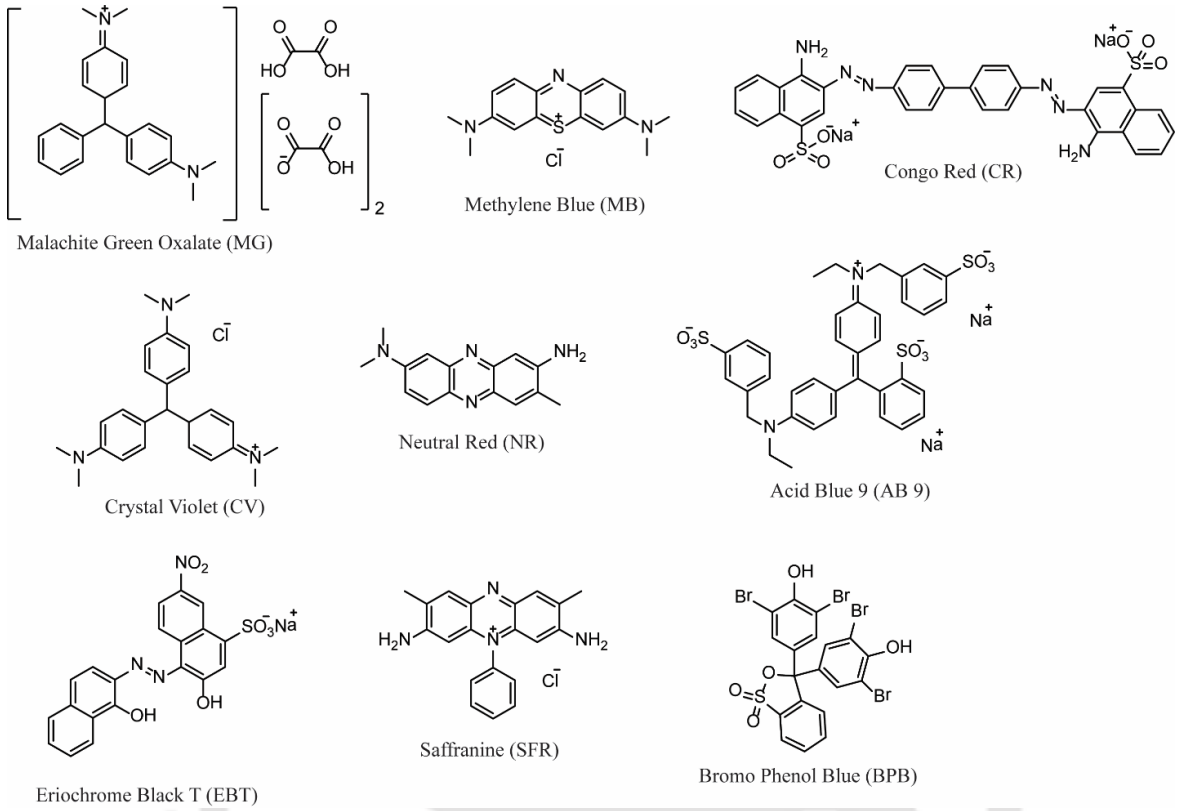

Figure A3.1 . Structure of different dyes used in adsorption experiments.

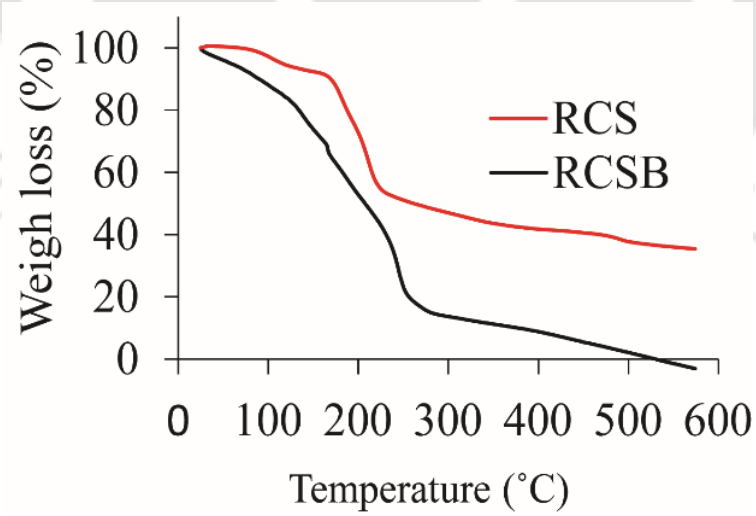

Figure A3.2 : Thermogravimetric analysis(TGA) data of RCS and RCSB

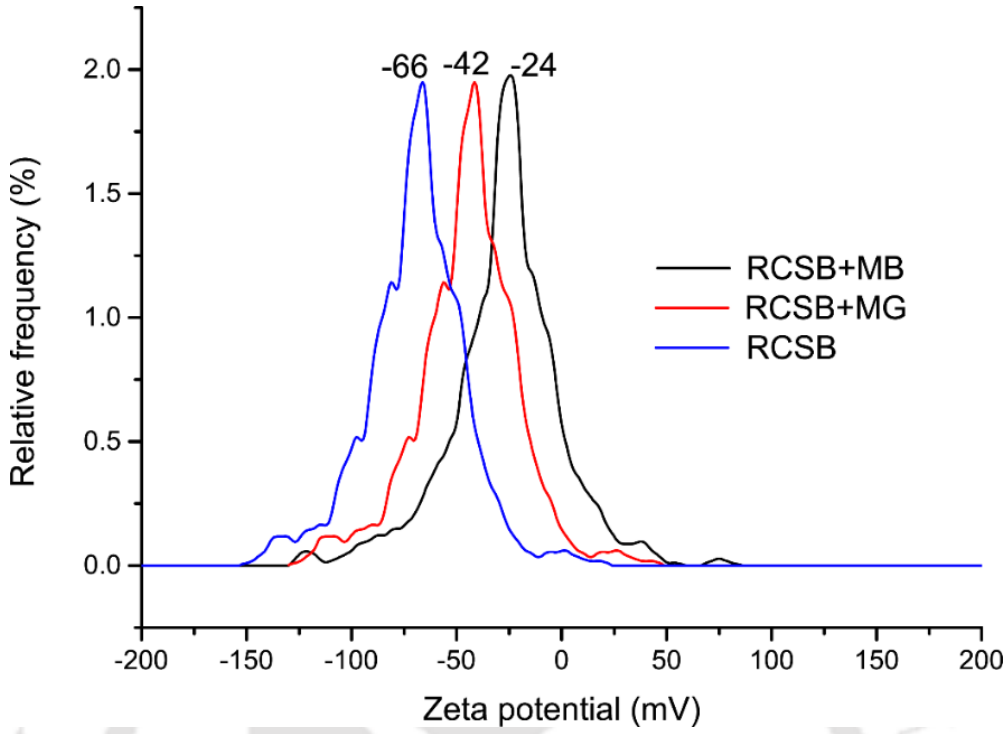

Figure A3.3 Zeta potential changes of RCSB after addition of dye MG and MB

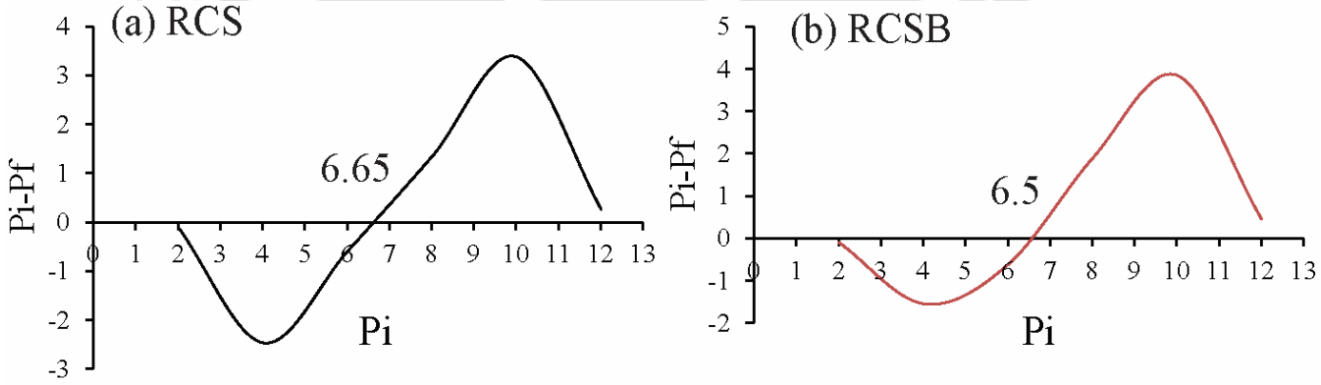

Figure A3.4 Plot for point of zero charge value of (a) RCS and (b) RCSB surface at neutral pH

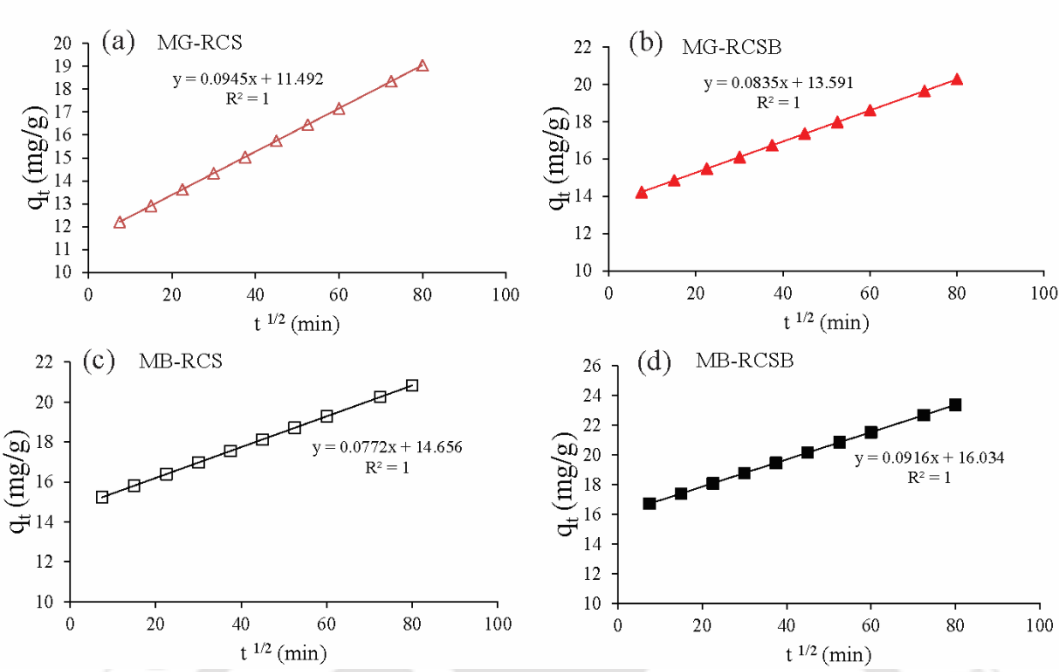

Figure A 3.5 Linear Intraparticle diffusion model of (a) MG-RCS, (b) MG-RCSB, (c) MB-RCS and (d) MB-RCSB

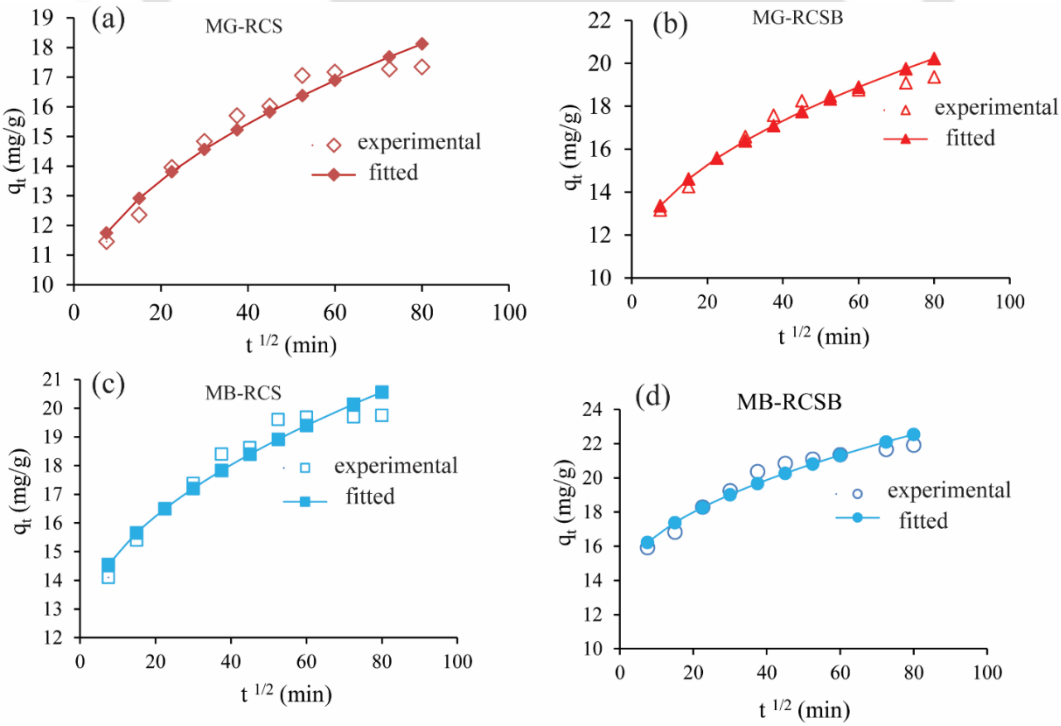

Figure A 3.6 Nonlinear Intraparticle diffusion model of (a) MG-RCS, (b) MG-RCSB, (c) MB-RCS and (d) MB-RCSB

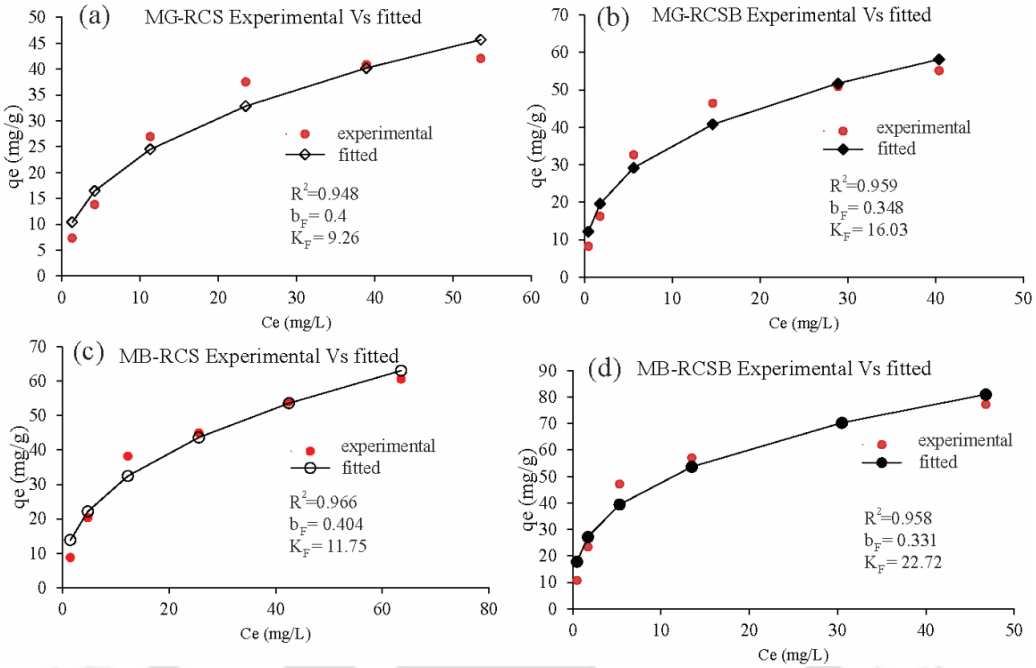

Figure A 3.7 Non linear Freundlich isotherm plot for (a) MG-RCS, (b) MG-RCSB, (c) MB-RCS and (d) MB-RCSB

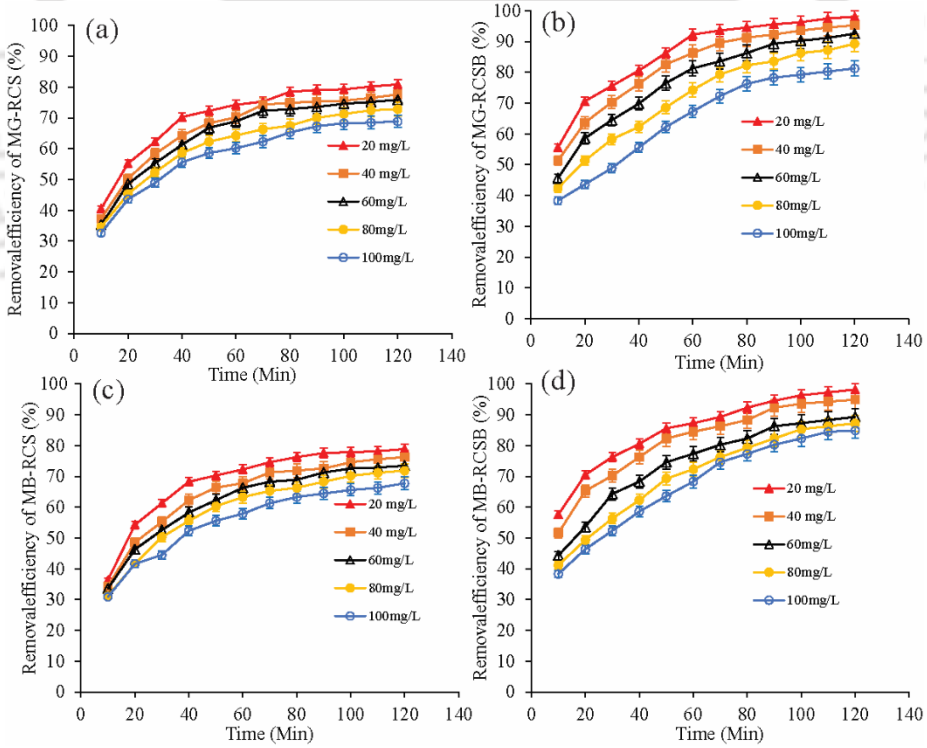

Figure A3.8 Effect of contact time on the removal % of (a) MG-RCS, (b) MG-RCSB, (c) MB-RCS and (d) MB-RCSB

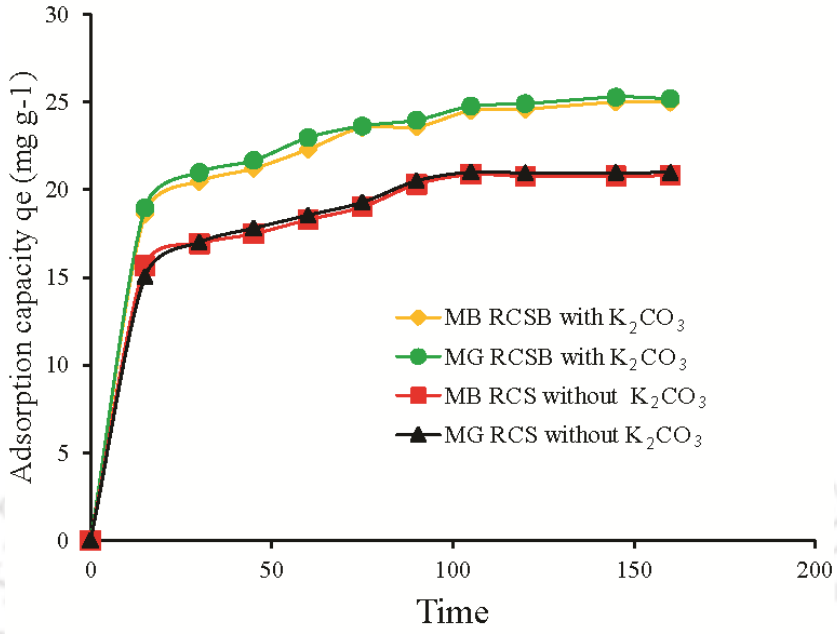

Figure A3.9 Adsorption capacity vs time of MB-RCSB with K_2CO_3, MG-RCSB with K_2CO_3, MB-RCS without K_2CO_3 and MG-RCS without K_2CO_3

Chapter 4

Biochar Derived from the Stem of *Ricinus communis* and *Colocasia esculanta*: Efficient Adsorbent for the Removal of Cd(II) and Pb(II) Ions from an Aqueous Environment

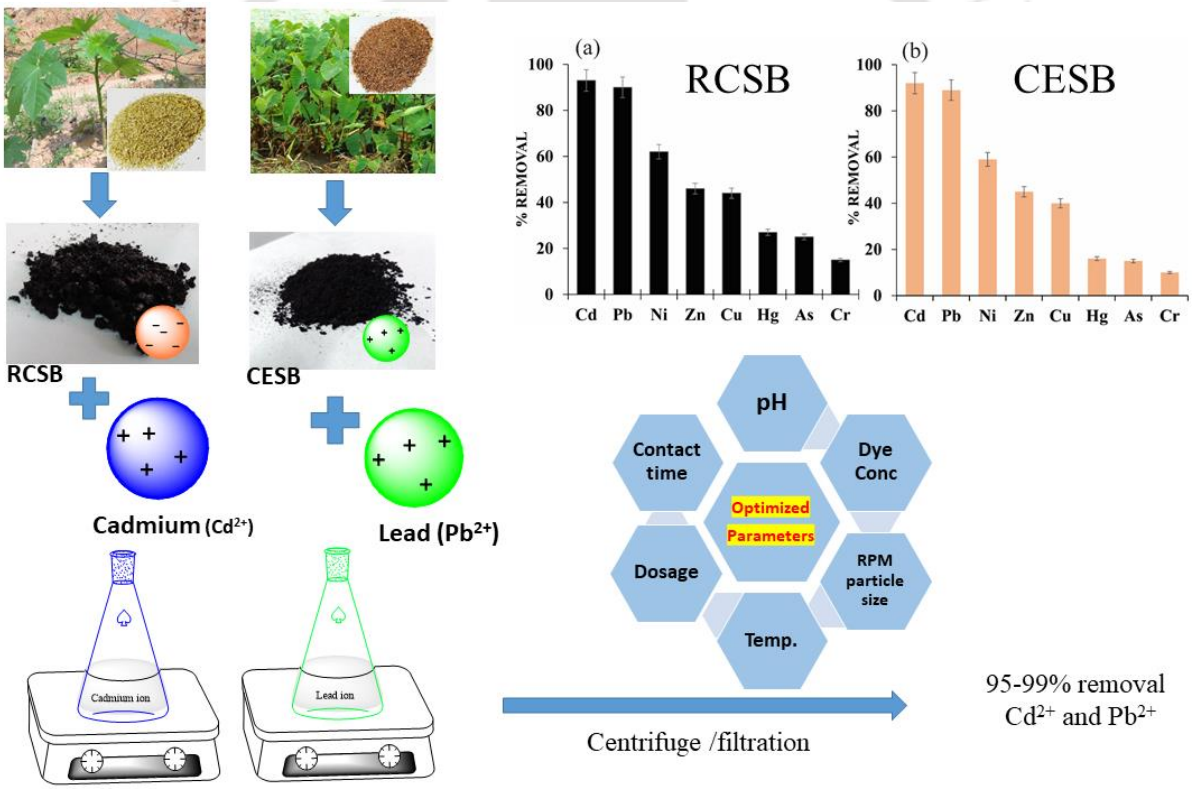

4.1 Background and Focus of the Chapter:

Water is a fundamental necessity for the survival of all living organisms on earth. It is the basis of life and is essential for the existence and growth of all life forms [4.1]. Water plays a vital role in maintaining bodily functions and overall health, from the smallest microorganism to the largest animals. Organic and inorganic contaminants are substances released into the environment and can cause significant harm to the ecosystem. Organic contaminants include chemicals such as pesticides, herbicides, and petroleum products, while inorganic contaminants include heavy metals, acids, and alkalis [4.2]. Heavy metals are toxic, non-biodegradable, and bioaccumulated in the food chain. Their presence in waters or soil may lead to a long-term risk to ecology and human health at moderate concentrations. Heavy metal ions harm human health and the environment as they store in the food cycle and cause harm to the brain, kidneys, nervous system, and liver [4.3]. Therefore other possible options are being explored for the cost-effective elimination of contaminants from the wastewater [4.4]. Biochar can be considered a sound and economical alternative instead of activated carbon because of its lower synthesis cost. Various methods have been developed to treat Pb and Cd pollution, including electroplating, ion exchange, reverse osmosis, precipitation, and membrane processes [4.5]. But due to high running costs and large volumes of toxic sludge, these treatment methods are unsuitable for extensive-scale application [4.6]. Adsorption is a widely preferred method for removing heavy metals from wastewater due to its high efficiency, cost-effectiveness, and wide availability of different adsorbents. Appropriately modified agricultural waste can be an effective adsorbent for removing heavy metal ions from wastewater [4.7].

Chemical activation of biochar in pollution control received increasing attention in recent years because it combines carbonization and activation simultaneously. Chemically activated biochar could develop better porous structures than physical activation [4.8]. The most commonly used chemicals employed as activating agents include H_3PO_4, $ZnCl_2$, NaOH, KOH, and K_2CO_3 [4.9,4.10]. Alkali hydroxides such as KOH are exorbitant, abrasive, and unsafe, creating discarding problems. However, K_2CO_3 is not hazardous as it is often added to foods as an additive [4.11]. Our study plant, *Ricinus communis* (Castor plant), has three significant parts, i.e., leaves, seeds, and stem. Among these three, leaves are used as feed for Eri-silkworm[4.12], and seeds are used for biodiesel production [4.13], but the stem of this plant has no practical use. Hence we have used its stem for a heavy metal removal study. The most significant barrier of these biosorbents is their application by industries as a cost-effective adsorbent and the difficulties associated with regeneration [4.14], hence the main focus of

this study is to develop K_2CO_3-activated biochar from renewable biomass waste RCSB as a low-cost biosorbent. Synthesized RCSB and CESB were tested for removing Cd^{2+} and Pb^{2+} ions from the synthetic wastewater under optimized adsorption operational conditions such as solution pH, dye concentration, dosage, contact time, and temperature.

Colocasia esculanta (CES), commonly known as "Taro," is a partially aquatic immerse plant widely found in waterlogged areas, lakes, and ponds [4.15]. Although little literature is available where RCS and CES stem were reported for removing heavy metal ions, detailed analysis with these biochar has not been studied.

Figure 4.1. (a) Small pieces of stems were dried in sunlight followed by the oven, (b) Grinding and sieved into small particles of 150–300 µm, and (c) Soaked into 0.01M K_2CO_3 solution and heated in a muffle furnace at 300 °C for 4 h

4.2 Results and Discussions

4.2.1 Characterization of biochar

Before exploring the adsorption capacity of the biochar, the surface morphologies of the RCSB and CESB biochar were studied using Field Emission Scanning Electron microscopy (FESEM). Figure 4.2 (a), (b) depicts that both biochar surfaces are porous, heterogeneous, and ideal for adsorption. The FTIR spectrum (Figure. 4.2 (f) and A4.2 (a)) showed –OH stretching peak at 3293, and 3363 cm^{-1},

C=O stretching frequency at ~1420 $cm^{-1,}$ and peak at 1062 cm^{-1} corresponds to C–O of cellulose. The presence of –OH and –COOH groups are responsible for the adsorption of metal ions [4.16]. PXRD

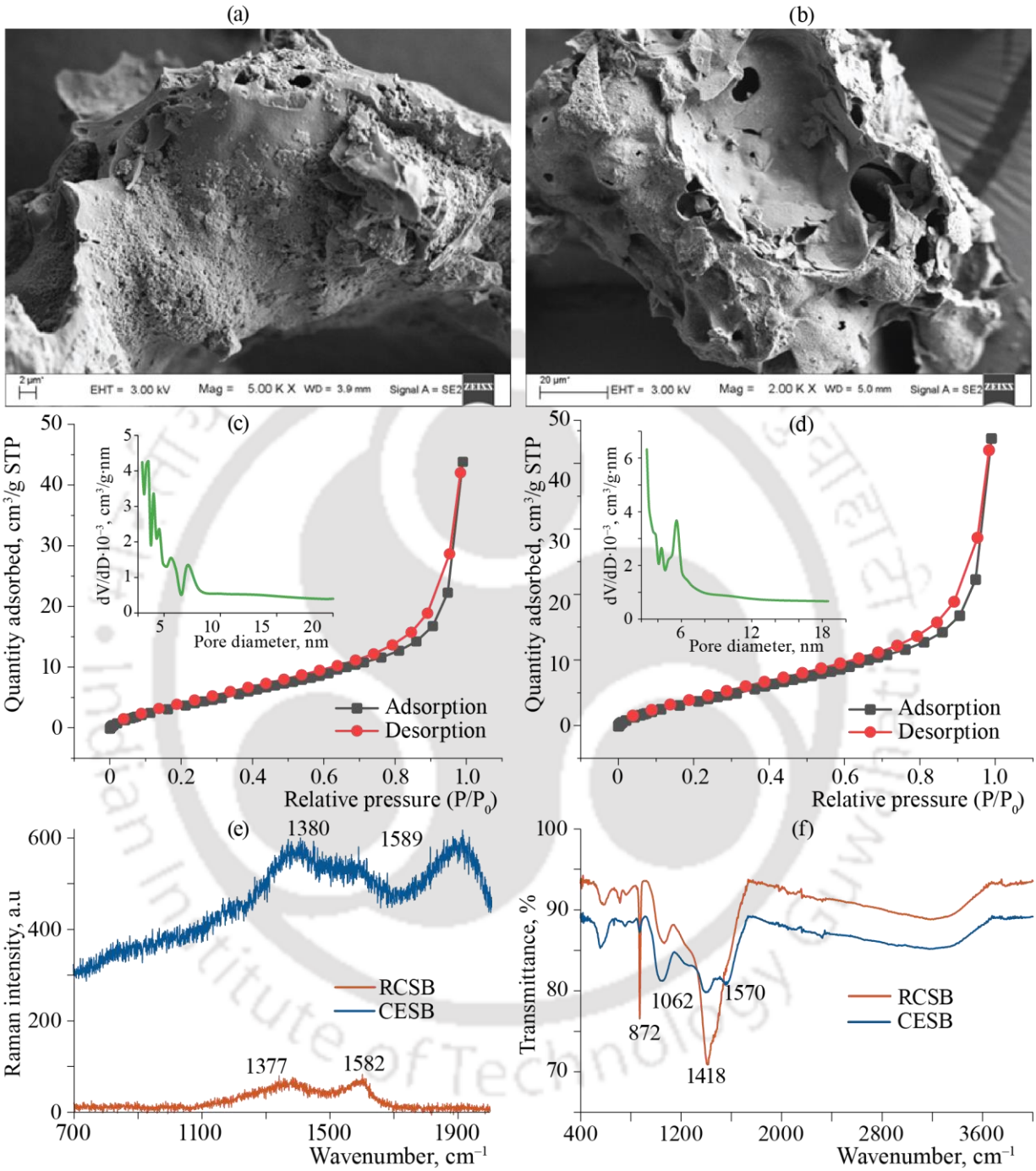

Figure 4.2 FESEM images of (a) RCSB, (b) CESB, (c), (d) BET pattern of RCSB, CESB with pore diameter, (e) Raman spectra of RCSB and CESB, and (f) FTIR spectra of RCSB and CESB

(Powder X-ray diffraction) data provide insights into the arrangement of the carbon atoms in the material and the degree of crystallinity or disorder present. Diffraction peaks at 2θ = 20.4; 23.1; 29.4; 36.1; 39.7; 43.2; 48.4 (for RCSB) and 2θ = 8.1; 25.1 (for CESB) attributed to the amorphous or disorder nature of the carbon structure (Fig. A4.3 (b)).In the case of RCSB, additional peaks were observed at higher angles, which may indicate the presence of crystalline or ordered carbon structures. The thermogravimetric analysis has been carried out to analyze the thermal stability of RCSB and CESB (Figure A4.3 (c)). In the case of RCSB, the first weight loss was observed at a range of 110 °C), which suggested eliminating the moisture contents. The second notable loss in the weight of the biochar indicated the removal of the volatile matters and increased the fixed carbon percentage in the biochar. Elemental analysis with the mapping of the adsorbents was carried out using Energy Dispersive X-ray Spectroscopy (EDX). It has been found that carbon and oxygen were the main components, and adsorbed metal ions were also seen in the EDX spectra (Figure A4.4). The zeta potential is an essential indicator of colloidal steadiness; it gives the degrees of electrostatic attraction or repulsion between charged particles in the solution. The surface charge of biochars was found to be −14 mV (RCSB) and −21 mV (CESB), and after the adsorption of heavy metal ions, its zeta potential value becomes −1.5 mV and −8 mV, respectively (Figure A4.5). This implies the adsorption of positively charged metal ions and a decrease in the surface charge of the adsorbent. Large functional groups at the biochar surface are accountable for the negative surface charge, specifying the electrostatic attraction with the positively charged heavy metal ions.

The BET (Brunauer−Emmett−Teller) isotherms examined the surface area by nitrogen adsorption-desorption as shown in Figure 4.2 (c-d). The specific surface area, pore volume, and pore radius were found to be 14.712 m^2/g, 0.048 cm^3/g, 3.616 nm for RCSB and 18.520 m^2/g, 0.067 cm^3/g, 3.053 nm for RCSB, CESB respectively. Although biochar's surface area is low, the high adsorption capacity of the biochar is due to electrostatic interaction between the opposing surface of the biochar and heavy metal ions. The Raman analysis is an excellent tool for seeing the structure of biochars at a microscopic level [1.17]. RCSB and CESB show peaks at 1377 cm^{-1} , 1582 cm^{-1}, and 1380 cm^{-1}, 1589 $cm^{-1,}$ respectively, corresponding to the D and G bands (Figure 4.2 (e). D-type bands indicate the biochar has a defective or disordered graphitic or carbon-like structure, while the G band is related to stretching SP^2 hybridized carbon atoms. The ratio of the intensity of the D-band to the G-band (i.e., the D/G ratio) is often used to indicate the degree of disorder or defects in the carbon structure of biochar. The high D/G ratio has been linked to an increased adsorption capacity of biochar for specific

contaminants, such as heavy metals and organic compounds. This is thought to be due to the greater availability of surface sites and functional groups on the biochar surface that can bind to these contaminants.

4.2.2 Heavy metal adsorption on biochar from an aqueous medium

Both biochars (RCSB and CESB) were treated with 10 mg. L^{-1} of eight heavy metal ions: cadmium, lead, nickel, zinc, copper, mercury, arsenic, and chromium. Among these eight metal ions, cadmium and lead show an excellent adsorption capacity (~92–98%) than other metals (Figure A4.1). Hence cadmium and lead ions have been taken for subsequent adsorption study with RCSB and CESB to get an optimized result.

4.2.2.1 Effect of time and adsorption dose on removal efficiency

Both the adsorbents show maximum absorption efficiency in 120 min (Figure 4.3 (a), (b)). Adsorption dosage is one of the critical factors affecting the adsorption capacity (q_e, mg. g^{-1}) and the percentage removal of heavy metal ions. A variable amount of adsorbent (0.2–1.5 g/L) was mixed with a fixed amount of adsorbate. The solution pH (~ 6.9), temperature (30°), and shaking speed (200 rpm) were kept constant during the experiment. The effect of RCSB and CESB dosage on Cd^{2+} and Pb^{2+} removal percentage increases with an increase in adsorbent dosage until it reaches a saturation point (Figure 4.3 (c), (d)). Among the different dosages used, 1.5 g/L of adsorbent was the suitable minimum adsorbent dosage for the maximum removal of Cd^{2+} and Pb^{2+} ions. After an equilibrium time, % removal doesn't increase, which can be explained by the partial assembly of the adsorbent particles at the surface of the adsorbent in higher concentrations.

4.2.2.2 Effect of solution pH on metal ion adsorption

The Effect of solution pH on metal ion adsorption is an important factor to consider when studying the adsorption behavior of metal ions onto solid surfaces. The pH of the solution can affect the surface charge of both the metal ions and adsorbent, which can, in turn, affect the adsorption process. The pH is the deciding factor for the adsorption of heavy metals for biochar, as adsorption occurs primarily through electrostatic attraction. At first, the adsorption increases with the pH from 2.0 to 6.8 and then decreases from 7.2 to 9 (Figure 4.3 (e), (f)). The optimal pH for the adsorption of Pb^{2+} and Cd^{2+} is between 6.8 to 7.2. The reduction of adsorption below pH 6.8 is due to excess hydrogen ions, causing

competition with the positively charged metal ions for the same place on the adsorption surface. Removal also decreases when pH is above 7.2, where the increase in pH encourages the formation of anionic hydroxide complexes that reduce the concentration of free metal ions [4.16]. The adsorption behavior of the biochar estimated in this study represents an excellent possibility for drinking water,

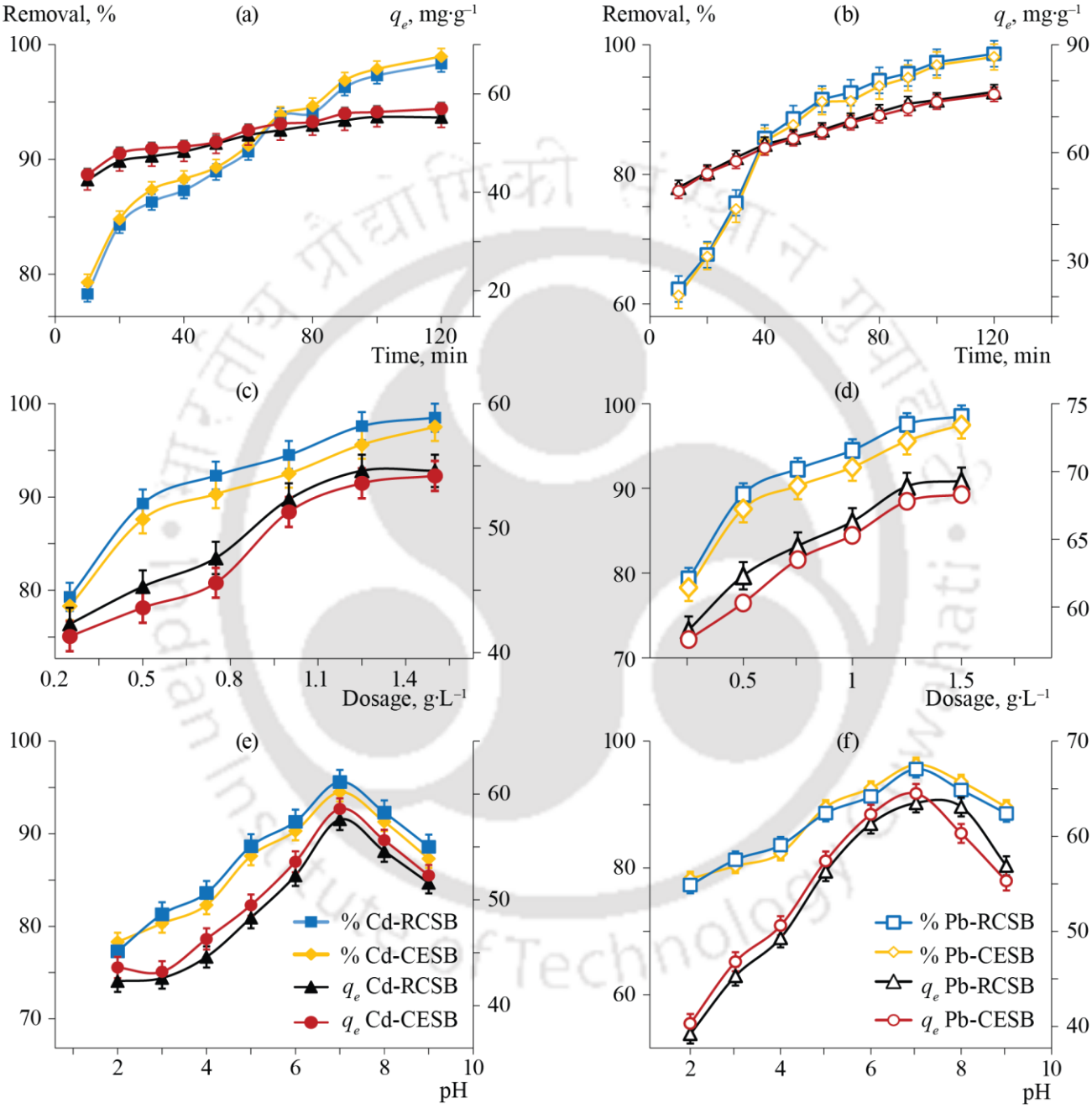

Figure 4.3. Effect of (a,b) contact time, (c,d) adsorbent dosage, and (e,f) pH on removal efficiency of Cd and Pb, respectively

, treatment with a pH value between 6.8 and 7.2. The effect of solution pH on metal ion adsorption is complex and depends on several factors, including the surface charge of the adsorbent, the type of metal ions, and the chemical form of the metal ion in the solution. Understanding these factors is essential for designing effective adsorption processes for metal ion removal from aqueous solutions.

4.2.2.3 Adsorption kinetics of Pb^{2+} and Cd^{2+} ions

Predicting when contaminants were separated from the aqueous solutions is essential to design suitable sorption treatment plants. The kinetics studies were conducted at different times to know the detailed adsorption mechanism. 100 $mg \cdot L^{-1}$ of metal ions (Pb^{2+} and Cd^{2+}) at pH 7.0 and 30 °C for RCSB and CESB were described by the pseudo-second-order kinetics model. The studies were carried out at different time intervals; equilibrium was reached at 120 min for Pb^{2+} and Cd^{2+} ions, respectively. Two kinetic models were used to show the experimental results: pseudo-first-order and pseudo-second-order models, which can represent by linear mathematical Eqs (1) and (2)[4.18,4.19].

$$\ln(q_e - q_t) = \ln q_e - k_1 t \quad (1)$$

$$\frac{t}{q_t} = \frac{1}{k_2 q_e^{\,2}} + \frac{t}{q_e} \quad (2)$$

Where q_e (mg. g^{-1}) is the amount of metal contaminant adsorbed at equilibrium, q_t (mg. g^{-1}) is the amount of metal contaminant adsorbed per gram of biosorbent at time t, t is the adsorption time (min), and k_1 ($g.mg^{-1} \cdot min^{-1}$) and k_2 ($g.mg^{-1}.min^{-1}$) is the pseudo-first-order and pseudo-second-order rate constants respectively. The intercept and slope of $\ln(q_e - q_t)$ vs. time have been used to calculate the q_e and K_1 values and plot t/q_t vs. time for evaluating q_e and K_2, respectively. The equation's linear regression coefficient (R^2) value gives the proper adsorption kinetics model. The R^2 values (≥ 0.99) from Table 4.1 indicate a suitable kinetics model in the case of heavy metal ions. The pseudo-second-order kinetics model explains that chemisorption was the primary rate-limiting step in the adsorption of heavy metal ions. Earlier literature confirms valence forces involve the sharing or exchanging of electrons between [4.20] heavy metal ions and biochar.

4.2.2.4 Adsorption isotherm of Cd^{2+} and Pb^{2+} ions

The adsorption isotherm is the relation between the equilibrium concentration of adsorbate in bulk and adsorbed amount on the surface. The parameters involved in the adsorbate-adsorbent interaction

Table 4.1 Kinetics parameters for pseudo-first-order and pseudo-second-order kinetics

Model	Kinetic parameters	RCSB		CESB	
		Cd^{2+}	Pb^{2+}	Cd^{2+}	Pb^{2+}
Pseudo-first-order	q_e	7.75	19.47	18.28	13.36
	K_1(L min^{-1})	-0.0003	-0.0003	-0.0002	-0.0002
	R^2	0.799	0.9399	0.9624	0.9862
Pseudo-second-order	q_e	44.64	45.66	45.04	44.44
	K_2 (g.mg^{-1}.min^{-1})	0.006	0.005	0.003	0.004
	R^2	0.999	0.999	0.999	0.999

are essential for designing a preferred sorption system. The adsorbent surface may be considered a monolayer or multilayer. Langmuir and Freundlich are the isotherm models [4.19] were used to describe the relationship between adsorbate-adsorbent interaction, which can be explained by using the following Eq. (3) and (4): [4.21-4.22]

$$\frac{C_e}{q_e} = \frac{C_e}{q_m} + \frac{1}{K_L q_m} \quad (3)$$

$$lnq_e = lnK_F + \frac{1}{n} logC_e \quad (4)$$

$K_{L.}$ (L·mg^{-1}) and $K_{F.}$ (L·mg^{-1}) are the Langmuir and Freundlich constant; 1/*n* is the nonlinearity exponent, *Ce* is the concentration of metal ions at equilibrium, q_e (mg·g^{-1}), and q_{max} is the adsorption capacity at equilibrium and maximum adsorption capacity at equilibrium. The isotherm parameters such as $K_{L.}$, $K_{F.,}$ $q_{max,}$ and R^2 are listed in Fig. 4.3 (a), (b) and table 4.2. Isotherm experiments were carried out to determine the maximum adsorption capacity by changing the metal ion concentration, as shown in Fig. 4.4 (a), which indicates the experimental data fitted with the Freundlich isotherm model and R^2 values were 0.992; 0.99; 0.99 and 0.99 for Cd^{2+}-RCSB, Pb^{2+}-RCSB, Cd^{2+}-CESB, and Pb^{2+}-CESB, respectively. These data show that the Freundlich isotherm model describes heavy metal removal using biochar as it has heterogeneous adsorption. Since the Freundlich coefficient (*n*) value was more than 1, it indicates favorable heavy metal adsorption.

Table 4.2 Adsorption isotherm parameters for Langmuir and Freundlich

Isotherm model	Kinetic parameter	RCSB		CESB	
		Cd^{2+}	Pb^{2+}	Cd^{2+}	Pb^{2+}
Langmuir	q_{max} ($mg \cdot g^{-1}$)	204.08	204.08	200	208.33
	K_L	17.24	21.32	18.24	23.81
	R^2	0.870	0.882	0.877	0.8615
Freundlich	1/n	0.489	0.564	0.512	0.587
	K_F	3.08	3.66	3.25	3.86
	R^2	0.991	0.996	0.996	0.994

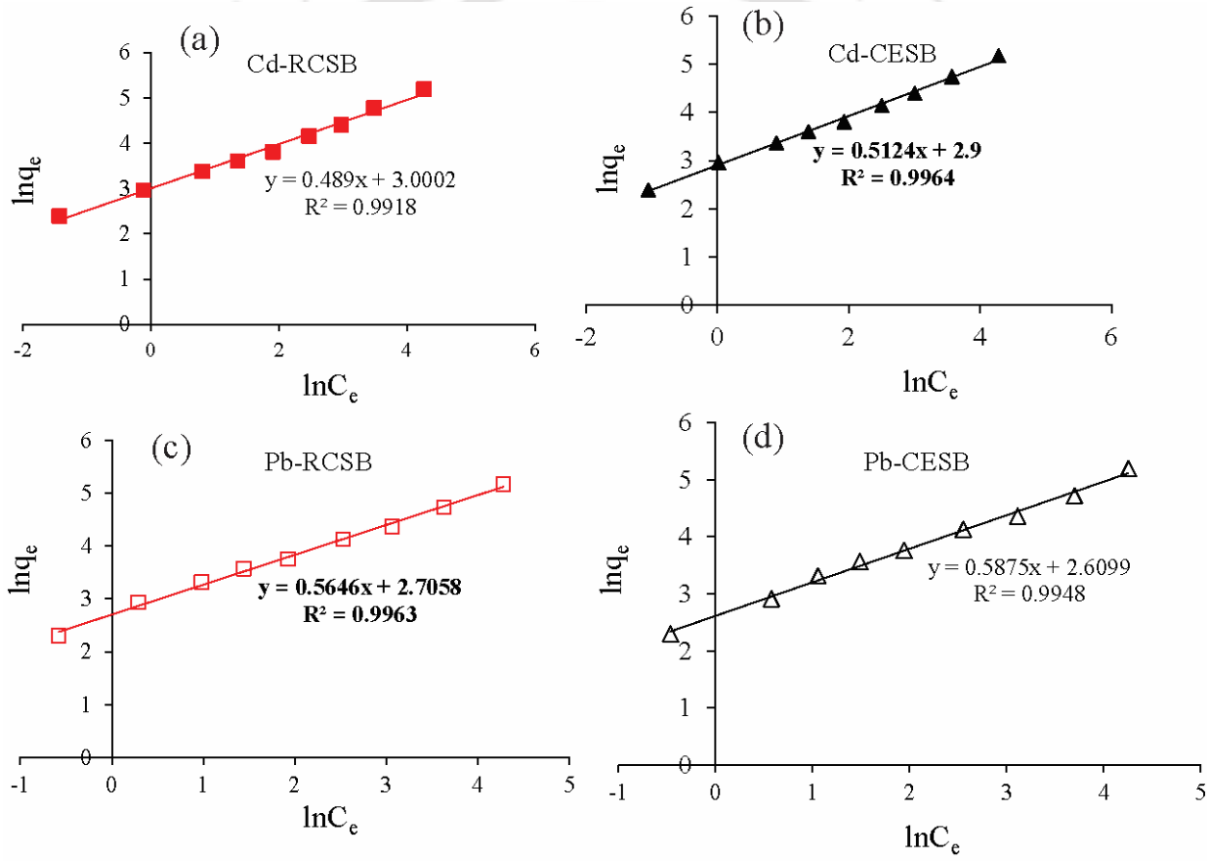

Figure 4.3 Freundlich isotherm of (a) Cd^{2+}-RCSB, (b)Cd^{2+}-CESB and (c) Pb^{2+}-RCSB and (d) Pb^{2+}-CESB

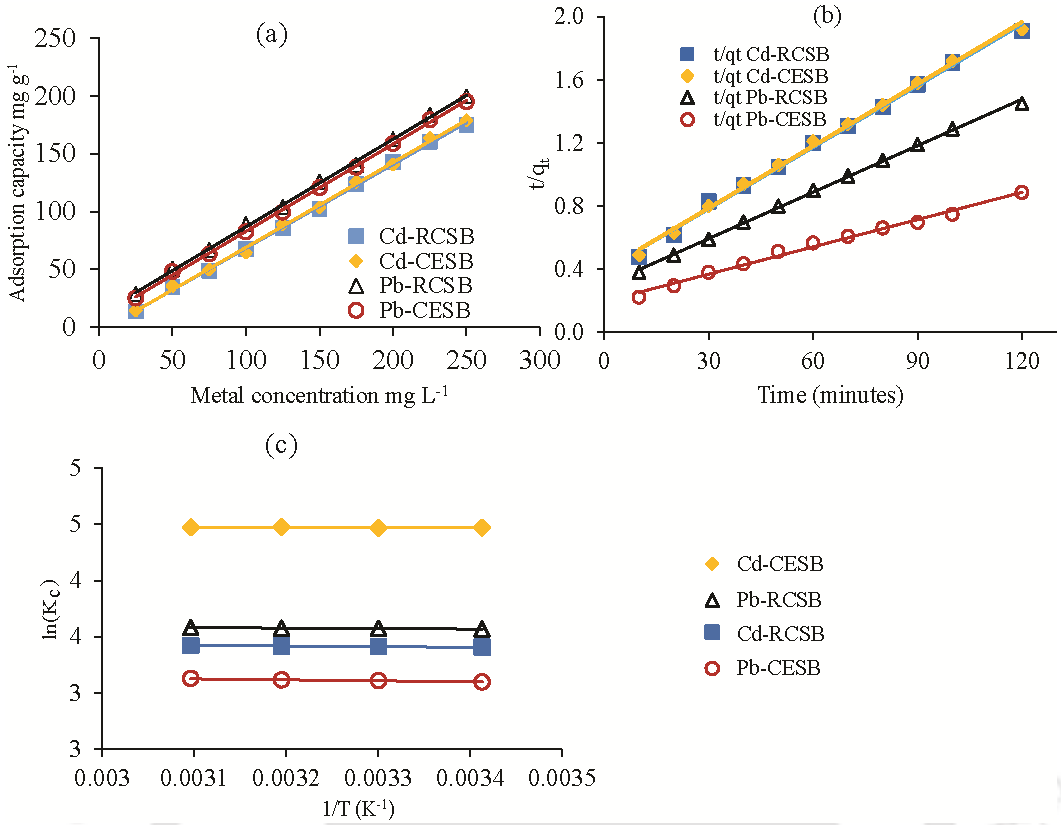

Figure 4.4 (a) Effect of initial metal ion concentration, (b) pseudo-second-order kinetics, and (c) thermodynamics curve of RCSB and CESB biosorbent on adsorption of Pb^{2+} and Cd^{2+}

4.2.2.5 Thermodynamics studies of Cd^{2+} and Pb^{2+} ions

The degree of adsorption depends on the temperature of the solid-liquid interface. Adsorption at different temperatures gives the adsorption feasibility of the system, which exhibits thermodynamic properties. Thermodynamic parameters such as Gibbs free energy (ΔG°, kJ.mol^{-1}), enthalpy change (ΔH° kJ.mol^{-1}), and entropy change (ΔS° J.mol^{-1}) were determined by using the Van't Hoff Eq. as [4.21,4.22]

$$\ln K_c = \frac{\Delta S^o}{R} - \frac{\Delta H^o}{RT} \quad (5)$$

$$\Delta G^{\circ} = -RT\ln(K_c) \quad (6)$$

$$\Delta G^{\circ} = \Delta H^{\circ} - T\Delta S^{\circ} \quad (7)$$

K_c is the equilibrium constant defined by q_e/C_e, qe is the metal ion concentration on the adsorbent at equilibrium, and C_e is the remaining metal ion concentration in the solution. R is the universal gas constant (8.314 J·mol^{-1}·K^{-1}), and T is the temperature in Kelvin (K).

The effect of solution temperature on the adsorption of Cd^{2+} and Pb^{2+} using RCSB and CESB adsorbents was investigated at a temperature range of 293, 298, 303, 308, 313, and 318K, which were summarized in Table 4.3. With the increase in temperature, the adsorption capacity of Cd^{2+} and Pb^{2+} on RCSB and CESB decreases, which suggests the adsorption process is favorable at a lower temperature. This may be due to the heavy metal molecule's tendency to escape from the solid adsorbent surface to the solution phase with an increase in the temperature of the solution [4.23]. The value of ΔH° and ΔS° were determined from the slope ($-\Delta H^{\circ}/R$) and intercept ($\Delta S^{\circ}/R$) from the plot of ln (K_c) vs. 1/T (Van't Hoff plot) using Eq. (6). Gibbs free energy, ΔG° values were calculated using Eq. (6). The positive ΔH° values suggests that the removal of the metal ion by biochar was endothermic, i.e., the adsorption process reached equilibrium by consuming energy from the system itself. The positive ΔS° values indicate good affinity between heavy metal ions and biochars and the increase in randomness at the solid-liquid interface. The negative ΔG° value indicates that the adsorption of heavy metal ions on RCSB and CESB adsorbents is feasible and spontaneous. Earlier studies show that if the ΔG° value comes between 0 and –20 $kJ \cdot mol^{-1,}$ adsorption is physical, and if values come between –80 and –400 $kJ \cdot mol^{-1,}$ then the adsorption system is chemical adsorption [4.24]. Hence in all cases, the adsorption of heavy metal ions is physical adsorption.

Table 4.3 Thermodynamic parameters for heavy metal adsorption on RCSB and CESB

Adsorbent	Temperature (K)	Cd^{2+}			Pb^{2+}		
		ΔG° KJ mol^{-1}	ΔH° KJ mol^{-1}	ΔS° J K^{-1} mol^{-1}	ΔG° KJ mol^{-1}	ΔH° KJ mol^{-1}	ΔS° J K^{-1} mol^{-1}
RCSB	293	-8.2950	0.4121	29.7142	-8.6844	0.3582	30.8616
	303	-8.5907			-8.9958		
	333	-8.8896			-9.3014		
	323	-9.1860			-9.6113		
CESB	293	-10.8837	0.0970	37.4712	-7.5430	0.7469	28.2884
	303	-11.2578			-7.8247		
	333	-11.6329			-8.1011		
	323	-12.0079			-8.3943		

4.2.2.6 Adsorption Mechanism for metal ion removal

The zeta potential measurement was done before and after the adsorption of heavy metal ions to know the adsorption mechanism. The zeta potential of both RCSB and CESB was measured after adding 10 mL (20 ppm) of both heavy metal ions. Before adding metal ions onto RCSB and CESB, the zeta potential values are –14 mV and –21 mV, respectively; after adding Cd^{2+} and Pb^{2+}, the zeta potential values become –1.5 m and –8 mV. The zeta potential value decreases due to the surface's electrostatic interaction and ion exchange mechanism. The positively charged metal ions bind with the negatively charged biochar surface, caused by the C=O and –OH groups on the biochar surface. Although the BET surface area analysis of RCSB and CESB is low (14.712 and 18.520 m^2/g), it was not a limiting factor for heavy metal removal [4.24]**.** The probable mechanism of interaction of biochar with the heavy metal ions is via electrostatic attraction, porous diffusion, surface complexation, and ion exchange, as shown in Figure 4.5 (a).

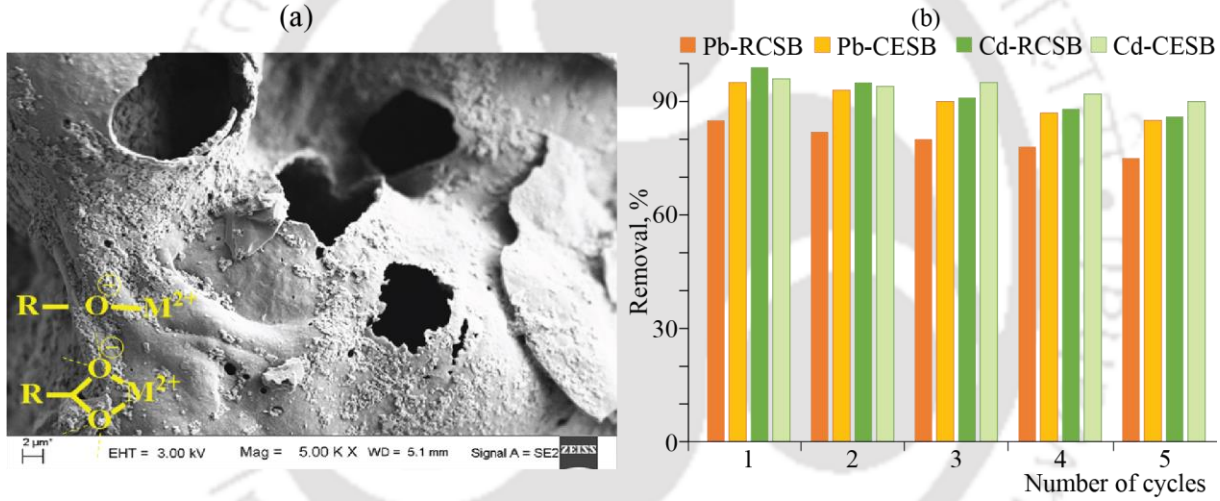

Figure 4.5 (a) Mechanism of biochar adsorption with heavy metal ions, (b) Desorption efficiency of RCSB and CESB on Cd^{2+} and Pb^{2+} dyes after five cycles

4.2.2.7 Desorption and recycling studies

Recycling the adsorbents makes the process eco-friendlier and more cost-effective; desorption studies were carried out to regenerate biochar. The Cd^{2+} and Pb^{2+} heavy metal-loaded RCSB and CESB biochar were mixed with deionized water, 0.1M HCl, and 0.1 M H_2SO_4, and concentrations of Cd^{2+} and Pb^{2+} were measured. The desorption efficiency of Cd^{2+} and Pb^{2+} on RCSB and CESB was calculated from the following equation [4.25]

$$\text{Desorption efficiency} = \frac{\text{Amount of dye desorbed (mg/L)}}{\text{Amount of dye adsorbed (mg/L)}} \times 100 \quad (8)$$

In the first cycle of heavy metal ions, in the case of Pb^{2+}, more than 85–90.0% removal was obtained after the fifth cycle, while in the case of Cd^{2+}, 92–98% removal occurs after the fifth cycle, Fig. 4.5 (b). Heavy metal ions are desorbed using 0.1 M HCl and 0.1 M H_2SO_4.

4.3 Conclusions

In batch mode experiments, biochar RCSB and CESB show excellent adsorption capacity for heavy metal ions (Cd^{2+} and Pb^{2+}). Various experimental parameters such as pH, adsorbent dosage, contact time, initial metal concentration, and temperature were used to get the optimized result. pH studies have shown that adsorption capacity is highest at neutral pH, which is a good characteristic of biochar. The adsorption isotherm studies indicate that heavy metal ion biosorption follows the Freundlich isotherm. Kinetics studies showed that biosorption parameters are best fitted with a pseudo-second-order kinetic model, and the adsorption mechanism is physical adsorption. A comparison of the maximum adsorption capacity of various adsorbents is shown in Table 4.4. All these results can be summed up that RCSB and CESB have good potential for removing heavy metal ions (particularly Cd^{2+} and Pb^{2+}) from an aqueous environment up to 99%.

Table 4.4 Comparison of the maximum adsorption capacity of various adsorbents is shown in the table.

Adsorbents	Heavy metals	Adsorption capacity ($mg\ g^{-1}$)	Reference
Apricot stone-activated carbon	Cd	33.57	[4.25]
Bagasse activated carbon	Cd	38.03	[4.26]
Ricinus communis Stem Biochar	Cd	204.08	This study
Colocasia esculanta Stem Biochar	Cd	200	This study
Coconut shell-activated carbon	Pb	26.50	[4.27]
Tamarind wood-activated carbon	Pb	134.22	[4.28]
Ricinus communis Stem Biochar	Pb	204.08	This study
Colocasia esculanta Stem Biochar	Pb	208.33	This study

REFERENCES

[4.1] Karatacs, A.; Karatacs, E. Environmental education as a solution tool for the prevention of water pollution. *J. Surv. Fish. Sci.* **2023**, 61–70.

[4.2] Ghaffar, I.; Hussain, A.; Hasan, A.; Deepanraj, B. Microalgal-induced remediation of wastewaters loaded with organic and inorganic pollutants: An overview. *Chemosphere* **2023**, 137921.

[4.3] Medhi, H.; Chowdhury, P.R.; Baruah, P.D.; Bhattacharyya, K.G. Kinetics of Aqueous Cu(II) Biosorption onto Thevetia peruviana Leaf Powder. **2020**, doi:10.1021/acsomega.9b04032.

[4.4] Suganya, S.; Kayalvizhi, K.; Kumar, P.S.; Saravanan, A.; Kumar, V.V. Biosorption of Pb(II), Ni(II) and Cr(VI) ions from aqueous solution using Rhizoclonium tortuosum: extended application to nickel plating industrial wastewater. *Desalin. Water Treat.* **2016**, *57*, 25114–25139, doi:10.1080/19443994.2016.1149111.

[4.5] Inyang, H.I.; Onwawoma, A.; Bae, S. The Elovich equation as a predictor of lead and cadmium sorption rates on contaminant barrier minerals. *Soil Tillage Res.* **2016**, *155*, 124–132, doi:https://doi.org/10.1016/j.still.2015.07.013.

[4.6] Bordoloi, N.; Goswami, R.; Kumar, M.; Kataki, R. Biosorption of Co (II) from aqueous solution using algal biochar: Kinetics and isotherm studies. *Bioresour. Technol.* **2017**, *244*, 1465–1469, doi:10.1016/j.biortech.2017.05.139.

[4.7] CHEN, Z. liang; ZHANG, J. qiang; HUANG, L.; YUAN, Z. hui; LI, Z. jun; LIU, M. chao Removal of Cd and Pb with biochar made from dairy manure at low temperature. *J. Integr. Agric.* **2019**, *18*, 201–210, doi:10.1016/S2095-3119(18)61987-2.

[4.8] Yahya, M.A.; Al-Qodah, Z.; Ngah, C.W.Z. Agricultural bio-waste materials as potential sustainable precursors used for activated carbon production: A review. *Renew. Sustain. Energy Rev.* **2015**, *46*, 218–235, doi:https://doi.org/10.1016/j.rser.2015.02.051.

[4.9] Ali, I.; Asim, M.; Khan, T.A. Low cost adsorbents for the removal of organic pollutants from wastewater. *J. Environ. Manage.* **2012**, *113*, 170–183, doi:10.1016/j.jenvman.2012.08.028.

[4.10] Jibril, M.; Noraini, J.; Poh, L.S.; Evuti, A.M. Removal of colour from waste water using coconut shell activated carbon (CSAC) and commercial activated carbon (CAC). *J. Teknol. (Sciences Eng.* **2013**, *60*, 15–19, doi:10.11113/jt.v60.1435.

[4.11] Garba, A.; Basri, H.; Nasri, N.S.; Isma'il, R. synthesis and characterization of porous carbon from biomass using KOH and K2CO3 chemical activation. *ARPN J. Eng. Appl. Sci.* **2016**, *11*, 1613–1617.

[4.12] Tulu, D.; Aleme, M.; Mengistu, G.; Bogale, A.; Shifa, K.; Mendesil, E. Evaluation of Castor (Ricinus communis L.) Genotypes and Their Feeding Values on Rearing Performance of Eri Silkworm (Samia cynthia ricini Boisduval) (Lepidoptera: Saturniidae) in Southwest Ethiopia. *Psyche J. Entomol.* **2022**, *2022*, doi:10.1155/2022/1556776.

[4.13] Saribiyik, O.Y.; Özcanli, M.; Serin, H.; Serin, S.; Aydin, K. Biodiesel production from ricinus communis oil and its blends with soybean biodiesel. *Stroj. Vestnik/Journal Mech. Eng.* **2010**, *56*, 811–816, doi:10.5545/sv-jme.2009.054.

[4.14] Yuen, F.K.; Hameed, B.H. Recent developments in the preparation and regeneration of activated carbons by microwaves. *Adv. Colloid Interface Sci.* **2009**, *149*, 19–27.

[4.15] Banerjee, S.; Mukherjee, S.; LaminKa-ot, A.; Joshi, S.R.; Mandal, T.; Halder, G. Biosorptive uptake of Fe2+, Cu2+ and As5+ by activated biochar derived from Colocasia esculenta: Isotherm, kinetics, thermodynamics, and cost estimation. *J. Adv. Res.* **2016**, *7*, 597–610, doi:10.1016/j.jare.2016.06.002.

[4.16] Repo, E.; Warchoł, J.K.; Bhatnagar, A.; Sillanpää, M. Heavy metals adsorption by novel EDTA-modified chitosan--silica hybrid materials. *J. Colloid Interface Sci.* **2011**, *358*, 261–267.

[4.17] Escribano, R.; Sloan, J.J.; Siddique, N.; Sze, N.; Dudev, T. Raman spectroscopy of carbon-containing particles. *Vib. Spectrosc.* **2001**, *26*, 179–186, doi:https://doi.org/10.1016/S0924-2031(01)00106-0.

[4.18] Shakoor, S.; Nasar, A. Adsorptive decontamination of synthetic wastewater containing crystal violet dye by employing Terminalia arjuna sawdust waste. *Groundw. Sustain. Dev.* **2018**, *7*, 30–38.

[4.19] Tavana, M.; Hajipour, V.; Oveisi, S. IoT-based enterprise resource planning: Challenges, open issues, applications, architecture, and future research directions. *Internet of Things* **2020**, *11*, 100262, doi:https://doi.org/10.1016/j.iot.2020.100262.

[4.20] Alqadami, A.A.; Naushad, M.; ALOthman, Z.A.; Alsuhybani, M.; Algamdi, M. Excellent adsorptive performance of a new nanocomposite for removal of toxic Pb(II) from aqueous environment: Adsorption mechanism and modeling analysis. *J. Hazard. Mater.* **2020**, *389*, 121896, doi:10.1016/J.JHAZMAT.2019.121896.

[4.21] Jawed, A.; Pandey, L.M. Application of bimetallic Al-doped ZnO nano-assembly for heavy metal removal and decontamination of wastewater. *Water Sci. Technol.* **2019**, *80*, 2067–2078.

[4.22] Regti, A.; El Kassimi, A.; Laamari, M.R.; El Haddad, M. Competitive adsorption and optimization of binary mixture of textile dyes: A factorial design analysis. *J. Assoc. Arab Univ. Basic Appl. Sci.* **2016**, *24*, 1–9, doi:10.1016/j.jaubas.2016.07.005.

[4.23] Kushwaha, A.K.; Gupta, N.; Chattopadhyaya, M.C. Adsorption behavior of lead onto a new class of functionalized silica gel. *Arab. J. Chem.* **2017**, *10*, S81–S89, doi:10.1016/J.ARABJC.2012.06.010.

[4.24] Sachan, D.; Ghosh, A.; Das, G. Valorization of aquatic weed Salvinia minima to value-added eco-friendly biosorbent: preferential removal of dye and heavy metal. *Int. J. Environ. Sci. Technol.* **2022**, doi:10.1007/s13762-022-04126-7.

[4.25] Kobya, M.; Demirbas, E.; Senturk, E.; Ince, M. Adsorption of heavy metal ions from aqueous solutions by activated carbon prepared from apricot stone. *Bioresour. Technol.* **2005**, *96*, 1518–1521.

[4.26] Mohan, D.; Singh, K.P. Single-and multi-component adsorption of cadmium and zinc using activated carbon derived from bagasse—an agricultural waste. *Water Res.* **2002**, *36*, 2304–2318.

[4.27] Sekar, M.; Sakthi, V.; Rengaraj, S. Kinetics and equilibrium adsorption study of lead (II) onto activated carbon prepared from coconut shell. *J. Colloid Interface Sci.* **2004**, *279*, 307–313.

[4.28] Singh, C.K.; Sahu, J.N.; Mahalik, K.K.; Mohanty, C.R.; Mohan, B.R.; Meikap, B.C. Studies on the removal of Pb (II) from wastewater by activated carbon developed from Tamarind wood activated with sulphuric acid. *J. Hazard. Mater.* **2008**, *153*, 221–228.

Annexure 4

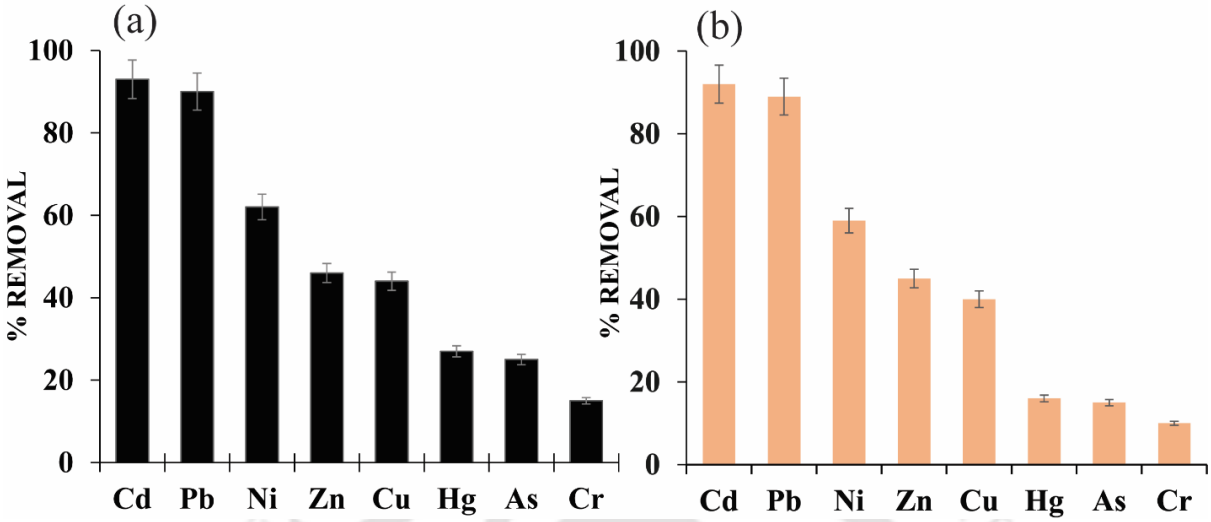

Fig: A4.1 Removal % of metal ions by RCSB and CESB.

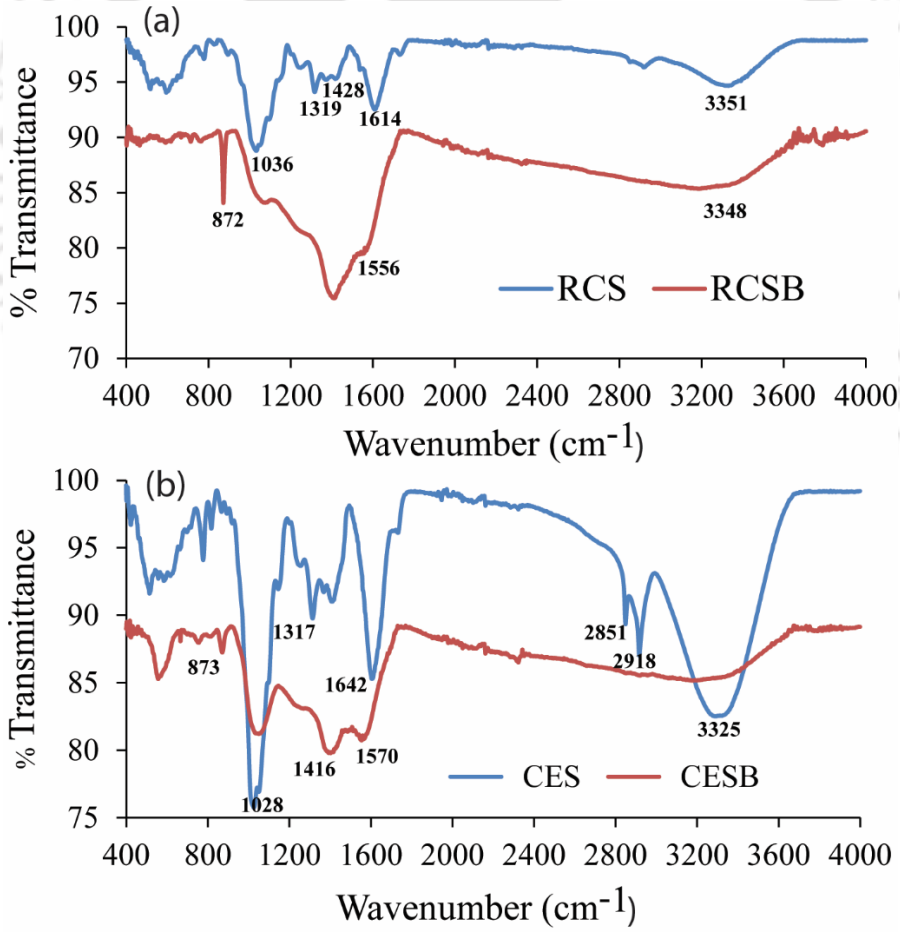

Fig. A4.2. FTIR Spectra of (a) RCS, RCSB and (b) CES, CESB

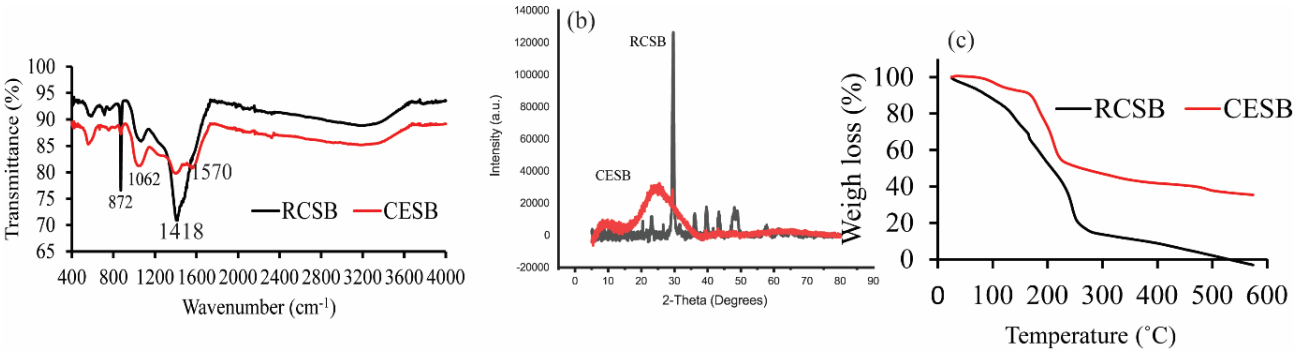

Fig. A4.3. FTIR spectra of (a) RCSB, CESB (b) PXRD of RCSB, CESB (c) TGA of RCSB, CESB

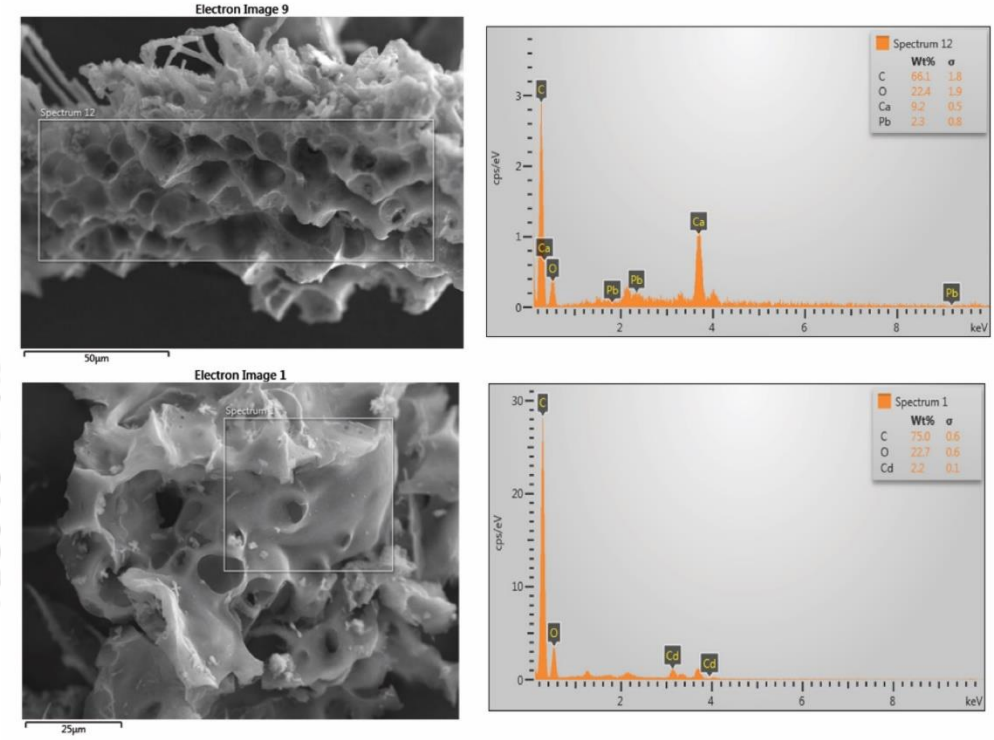

Fig. A4.4. FESEM image of RCSB after adsorption of Cd^{2+} and Pb^{2+}

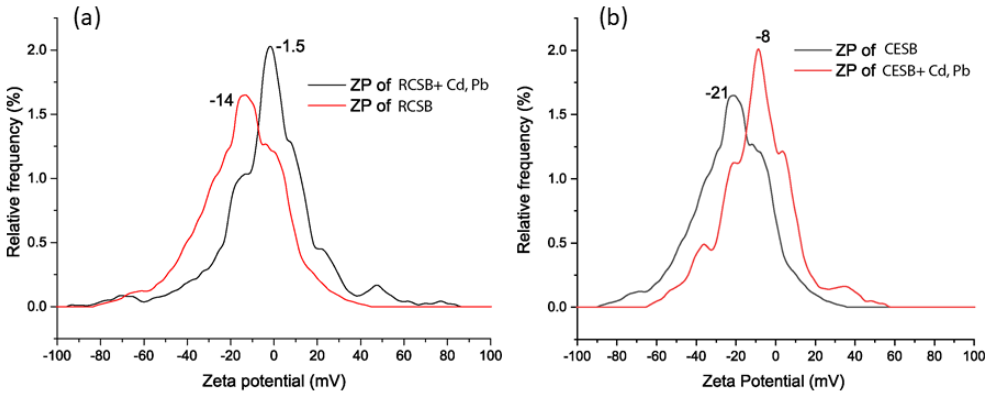

Fig: A4.5 . Zeta potential value of RCSB, CESB (before and after adsorption)

Chapter 5

Hydrochar and NCDs derived from *Colocasia esculanta* stem for effective removal and sensing of toxic metal ions

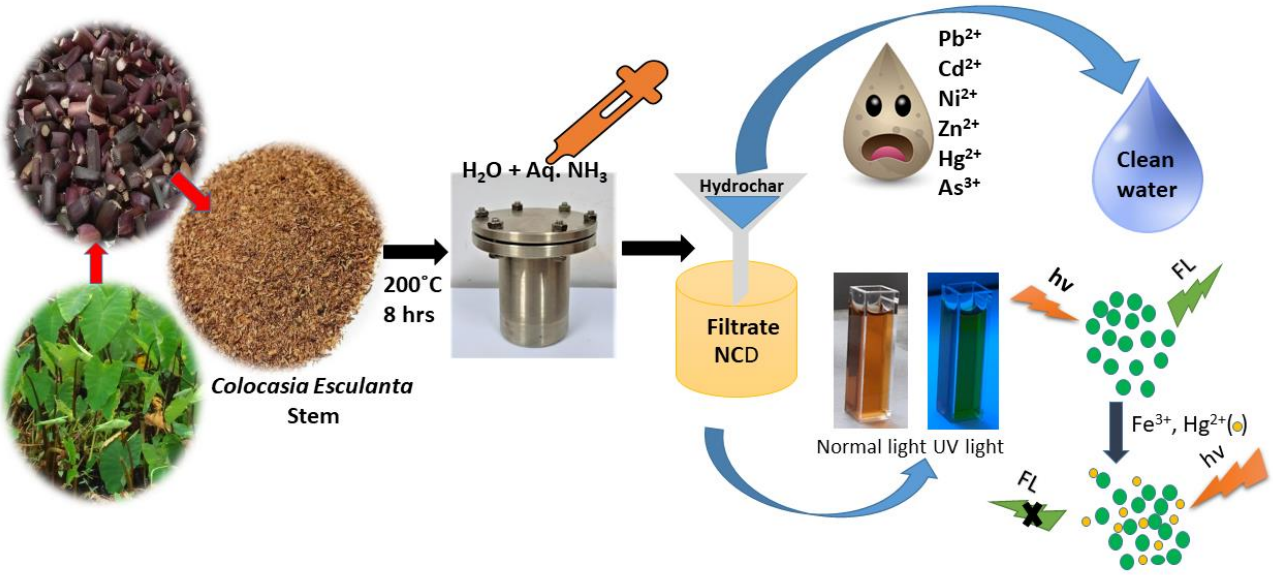

5.1 Background and Focus of the Chapter

Heavy metal pollution is a significant environmental concern due to its adverse impact on human health and ecosystems. Industrial wastewater, mining, and agricultural runoff are among the primary sources of heavy metal contamination in water bodies. These toxic metals can accumulate in the food chain and cause severe health problems, such as cancer, kidney damage, and neurological disorders[5.1]. Several techniques have been developed to remove heavy metals from contaminated water, but most are costly, energy-intensive, and produce toxic by-products. Thus, there is an urgent need for an eco-friendly, cost-effective, and efficient method for heavy metal removal. Various removal methods are available such as precipitation, flocculation, membrane separation, ion exchange, evaporation, and adsorption. All these removal methods have advantages and disadvantages regarding efficiency, sensitivity, specificity, and selectivity [5.2]. Among these removal methods, adsorption is often used because of its simple design, low cost, ease of operation, and high removal efficiency from low concentration [5.3]. The adsorption method uses biosorbents such as fiber, peat, wool, and living plants and bacteria [5.4]. Plants consist of lignin, cellulose, hemicellulose, and a minute quantity of pectin and extractives (fat, fatty acid, fatty alcohol, phenols, terpenes, steroids, resin acids, rosin, and waxes). Metal ions primarily adsorb to carboxylic (mainly present in pectin and hemicellulose but also extractives and lignin), phenolic (lignin and extractives), hydroxylic (cellulose, hemicellulose, lignin, and extractives) and carbonyl groups (lignin) [5.5–5.7]. The association of ion exchange and complexation is related to the binding of toxic metal ions by carboxylic, hydroxylic, and phenolic groups [5.4]. Hydrochar, a carbon-rich material derived from the hydrothermal treatment of biomass, has recently gained attention as an alternative material for heavy metal removal due to its unique properties, including a high adsorption capacity and low toxicity.

Furthermore, carbon dots (CDs) are another class of carbon-based material that has gained considerable interest in recent years. CDs are fluorescence nanoparticles with excellent optical properties, including high photostability, biocompatibility, and low toxicity. They have various applications, including bioimaging, drug delivery, and sensing. The CD was first discovered in 2004 during the purification of single-wall carbon nanotubes [5.8]. CDs are carbon nanoparticles with an average size of less than 10 nm and contain SP^2 hybridized carbon with a crystalline or amorphous core [5.9]. It has an oxidized carbon surface with a large number of carboxyl (-COOH) [5.10] and hydroxyl (-OH) [5.11] groups with SP^3 hydrocarbons($-CH_3$) [5.12]. It is a competitor in place of traditional semiconductor quantum dots. It is applied in nanodevices due to their advantages of chemical inertness, water solubility, low toxicity, biocompatibility, easy functionalization, and photoluminescence properties [5.13]. These attributes have been used broadly in various fields, such as electrochemistry, wastewater treatment [5.14], photocatalysis

[5.15], bioimaging [5.16], light-emitting devices [5.17], sensing, etc. [5.18]. There are various types of methods to synthesize CDs, such as electrochemical [5.19], hydrothermal [5.18], microwave synthesis [5.20], simple heating techniques [5.21], etc. Among these synthesis methods, hydrothermal has been extensively used to synthesize CDs due to its simplicity, easy control of the reaction, low energy use, and green synthetic route [5.22]. Carbon dots can be classified into raw, passivated, and functionalized (5.23). Due to poor fluorescence properties and less quantum yield, natural CDs have drawbacks [5.24]. Therefore passivation and functionalization of CDs with heteroatoms (N, P, and S) play an essential role in stabilizing and increasing the fluorescence properties [5.25–5.27]. Hydrothermal treatment is the most extensively used method to synthesize CDs wherein the biomolecules in the natural carbon precursors converting into CDs may undergo dehydration, polymerization, and carbonization [5.28]**.** Starch, polysaccharide, and sugar are bioresources that are precursors for CD synthesis. Some bioresources that can be considered for producing non-toxic, low-cost CDs are orange juice [5.3] garlic, [5.22] grape juice, [5.23] and banana juice [5.29]. Hydrothermal carbonization (HTC) is a process that involves the conversion of biomass into carbon-rich material called hydrochar by subjecting it to high temperature and pressure in the presence of water. In recent years, HTC has gained attention as a promising method for producing hydrochar from various biomass materials, including agricultural residues, forestry, and municipal solid waste. Furthermore, the by-product of HTC during hydrochar synthesis can be used as a precursor for the synthesis of CDs which are fluorescence nanoparticles with various applications, including sensing, imaging, and drug delivery.

N-doped carbon dots (NCDs) are carbon nanoparticles that contain nitrogen atoms in their structure. These CDs have gained attention in recent years due to their unique properties and potential applications in various fields. One advantage of NCDs over regular carbon dots (CDs) is their improved fluorescence properties. The presence of nitrogen atoms in the carbon dot structure can create defects and trap states that result in enhanced fluorescence emission [5.30]. This means NCDs exhibit brighter fluorescence and higher quantum yields than normal CDs, making them more suitable for sensing and imaging applications. Moreover, the presence of nitrogen atoms in the carbon of structure can also lead to improving stability and biocompatibility.

In this Chapter, we aim to explore the potential of *Colocasia esculanta* stem hydrochar for heavy metal removal, and subsequently, nitrogen-doped carbon dots (NCDs) were prepared from the filtrate. The study presents the photophysical characterization of the NCDs and demonstrates their potential in sensing Hg^{2+} and Fe^{3+} ions through FL quenching efficiency.

The hydrochar synthesized from the *Colocasia esculanta* stem showed a high adsorption capacity for heavy metals, including Pb (II) and Cd (II). The adsorption data were fitted to the Langmuir

isotherm model, and the maximum adsorption capacity for Pb (II) and Cd (II) was found to be 84 $mg.g^{-1}$ and 94 $mg.g^{-1}$ respectively, which makes hydrochar a suitable adsorbent in toxic metal removal.

5.2 Results and discussion

5.2.1 Characterization of hydrochar and carbon dots

Hydrochar and carbon dots are two types of carbon-based materials with unique properties and potential applications in various fields, such as environmental remediation and metal sensing. Characterization of these materials is crucial for understanding their properties for specific applications. Hydrochar is a carbon-rich material produced by hydrothermal carbonization of biomass, which involves heating biomass in the presence of water under high pressure and temperature. To characterize hydrochar, several analytical techniques can be used. FTIR can be used to identify the functional groups present in hydrochar, XRD can be used to determine the crystalline or amorphous structure, and FESEM can be used to visualize the morphology of hydrochar. TGA can be used to study the thermal stability and decomposition behaviour of hydrochar.

Carbon dots, on the other hand, are small carbon particles with a diameter of less than 10 nm, which have unique optical properties such as strong fluorescence and high photostability. Uv-Vis and fluorescence spectroscopy can be used to measure the optical properties of carbon dots, while FTIR and XPS can be used to study their surface chemistry. FETEM can be used to visualize the morphology and size distribution of carbon dots.

Identification of the functional groups present at the surface of the hydrochar and NCDs was carried out using ATR-FTIR (Fig. 5.1(a),5.1(b). The FTIR profile of CESH revealed peaks at 3336 cm^{-1}, 2918 $cm^{-1,}$ and 2851 cm^{-1}, which can be attributed to the polymeric O-H stretch**,** C-H stretching, and asymmetric CH_2 stretch, respectively**.** A sharp peak at 1606 cm^{-1} indicated the presence of primary amine (N-H bend). Peaks at 1435 cm^{-1} and 1371 cm^{-1} showed methyl C-H asymmetric and symmetric bend, respectively, while the 1318 cm^{-1} peak was due to phenol or tertiary alcohol. Similar specific peaks were also observed in the case of NCDs, such as the peak at 3196 $cm^{-1,}$ which was due to polymeric OH stretch, another peak at 1574 cm^{-1} indicating secondary amine (N-H bend), and 1394 cm^{-1} for carboxylate. The surface morphology of the hydrochar revealed a porous surface, as depicted in the FESEM image of Fig. 5.2 (a), which perhaps facilitated the adsorption of the toxic metal ions at the surface. The EDAX analysis with elemental mapping of CESH and NCD shows primary elemental composition are carbon, oxygen, and nitrogen (Fig. A5.1 and A5.2).

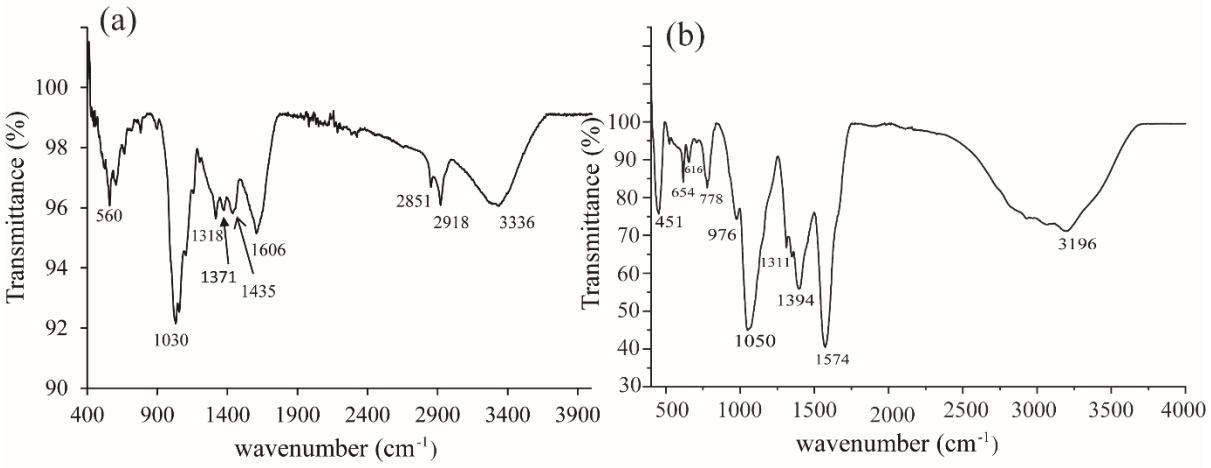

Figure 5.1 FTIR of (a) CESH and (b) NCD.

Fig. A5.3 shows the adsorption-desorption isotherm of CESH. The BET surface area of the hydrochar was 18.320 m^2/gm, the pore volume was 0.067 cm^3/g, and the pore diameter was 3.321 nm. The Zeta potential value of the hydrochar before metal ion adsorption was -26 mV. Following metal adsorption, the zeta potential was recorded as -5.0 mV, which indicated the adhesion of the positively charged metal ions to the CESH surface. Although the BET surface area of hydrochar is low, zeta potential data suggested that the high % removal of hydrochar was primarily due to the electrostatic interaction. Nitrogen-doped carbon dots (NCD) and bare carbon dots (CD) were characterized by X-ray photoelectron spectroscopy (XPS) (Fig. 5.3a-h). X-ray photoelectron spectroscopy is a powerful analytical technique used to determine elements' chemical composition and electronic state on a sample surface. The XPS spectrum of NCD revealed three peaks at 284.0, 400.0, and 532.0 eV, which are assigned to C_{1s}, N_{1s}, and O_{1s}, respectively. Survey scan XPS data of NCD (Fig. 5.3a) validated doping of nitrogen atoms into CDs, their surface composition, and the chemical state of the NCDs. The presence of nitrogen was also verified by EDAX analysis (Fig. A5.2). High-resolution scan of the C_{1s} region indicated the presence of peaks at 285, 285.8, and 284.32 eV (Fig. 5.3b), which are attributed to C-OH/C-O-C, C-N, and C=C, respectively. The peak at 400 eV (Fig. 5.3d) of the N_{1s} region was due to $C\text{-}N^+$/C-N(O). High-resolution O_{1s} peaks were observed at 531.54 eV (C=O), 532.9 eV (O-C=O), and 533.32 eV. These data suggested that NCDs have more functional groups on the surface, which provide lone pairs of electrons to coordinate toxic metal ions [5.31]. Besides, Raman spectroscopy confirmed the characteristic peaks of the CDs denoted by the D and G bands, which were observed at 1363 cm^{-1} and 1601 cm^{-1}, respectively (Fig. A5.8). A ratio of I_D/I_G intensities was calculated and observed to be 1.07, which denotes the purity of the NCDs [5.32]. FETEM analysis of NCD indicated that the average particle size was ~5.0 nm (Fig. 5.2c, 5.2d and A5.4). The SAED pattern's diffraction ring revealed the amorphous nature of the NCDs [5.33]. HRTEM image (Fig. A.5.5) indicated the presence of

clear lattice fringes with a d-spacing of 0.29, which corresponds to the (1 0 0) in-plane lattice of graphite[5.34,5.35]. (Fig. 5.2b) depicts the XRD diffraction peak at 24.04° indicates an amorphous carbon phase and partial graphitization of NCDs, which are attributed to large functional groups and graphitization of carbon atoms [5.36], respectively. The morphology of the NCD is further studied using atomic force microscopy (AFM) analysis. Fig.A5.6 represents the AFM image of a diluted solution of diluted NCD. The height profile indicates that the average height of the system is around 9 nm. These results further confirmed that a graphite structure exists in the carbon core of NCDs.

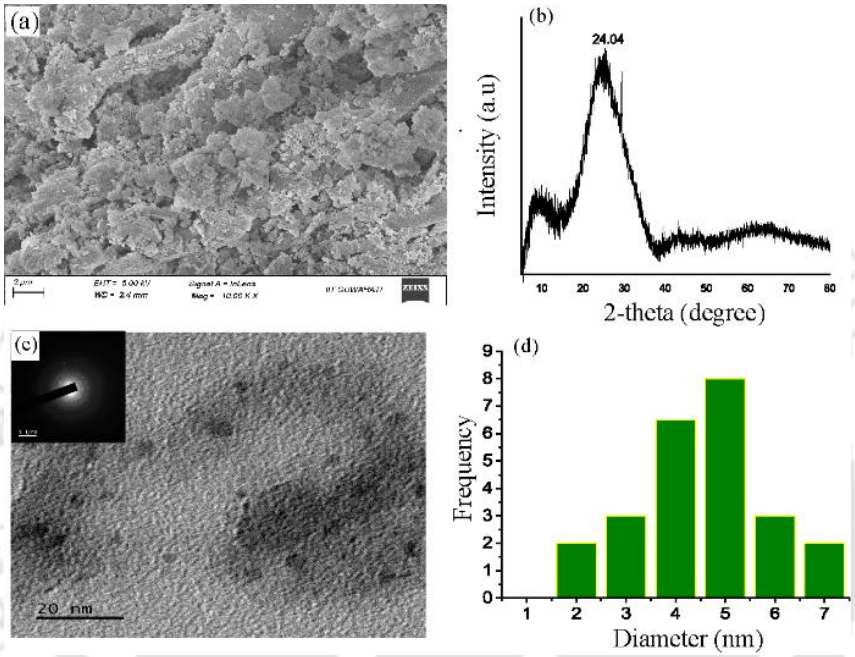

Figure 5.2 (a) FESEM image, (b) PXRD pattern, (c) FETEM image and SAED pattern of the N-CDs, and (d) particle size distribution histogram of N-CDs.

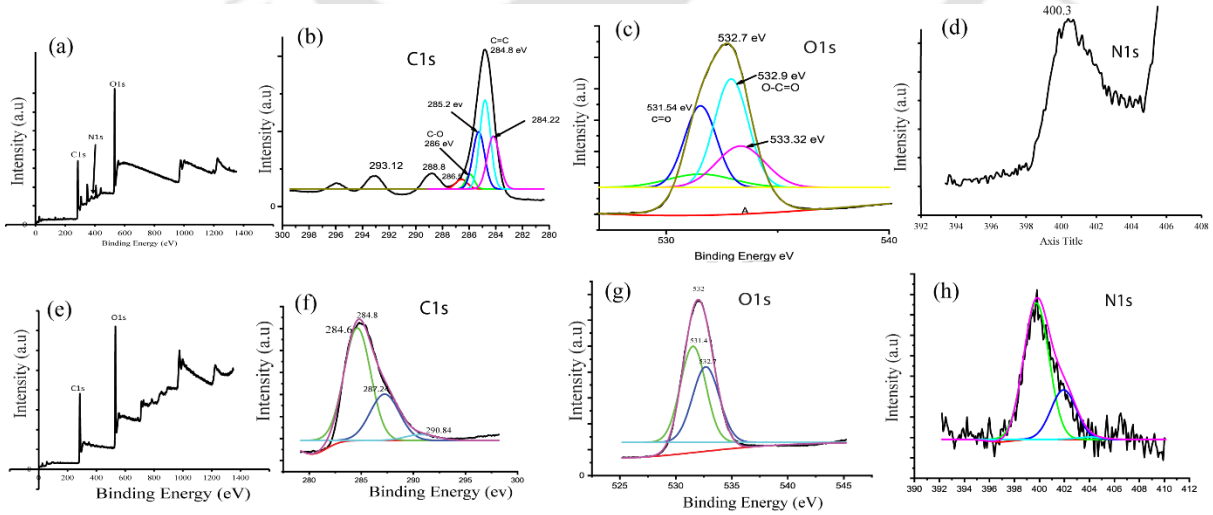

Figure 5.3. (a) XPS survey spectra of NCDs. (b), (c) and (d) are the high-resolution XPS spectra of C1s, O1s, and N1s, respectively, of NCD, and (e) XPS survey spectra of bare CD without nitrogen doping. (b), (c) and (d) are the high-resolution XPS spectra of C1s, O1s, and N1s, respectively, of CD.

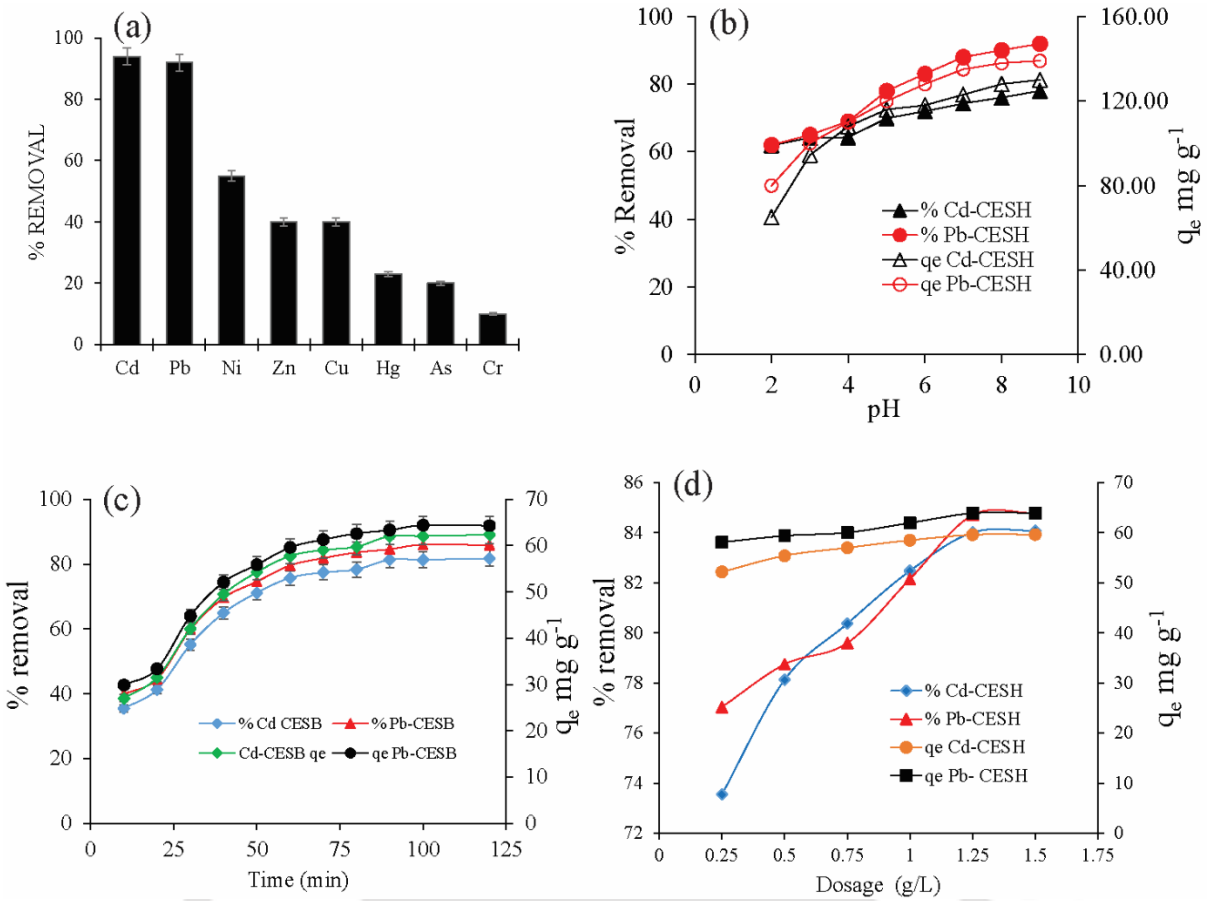

Figure 5.4 (a) % removal of toxic metals by CESH, (b) effect of pH using Cd^{2+} and Pb^{2+} on CESH surface, (c) Effect of contact time, (d) Effect of adsorbent dosage by CESH using Cd^{2+} and Pb^{2+}.

5.2.2 Adsorption experiments with *Colocasia esculanta* stem hydrochar (CESH)

At first, CESH was treated with eight toxic metal ions to ascertain its potential as an adsorbent for removing the selected metal ions as shown in Fig.5.4a. It has been observed that CESH could remove more than 90% of Cd^{2+} and Pb^{2+} than other metal ions. Therefore, further adsorption experiments were carried out with these metal ions.

5.2.3 Effect of pH of Cd^{2+} and Pb^{2+} on hydrochar surface

It is important to note that the effect of pH on the adsorption of heavy metals by hydrochar is complex and dependent on several factors, including the concentration of heavy metals, the type of functional groups present on the surface of the hydrochar, and processing conditions used to produce the hydrochar. The pH effect on the adsorption of heavy metals (Cd^{2+} and Pb^{2+}) was studied by varying pH (2-10) at an optimum dose of 20 mg/L working concentration of heavy metals. The result is shown in Fig. 5.4b. The adsorption % increases with the increase of pH, and high adsorption capacity was achieved at almost pH ~7.5. The probable reason was that the surface of CESH has more negative charge near pH ~7.5. The results show the ions Cd^{2+} or Pb^{2+} in the

solution for pH < 7.5, and for pH>7.5, it is noticeable that precipitation has a major effect on the removal of these ions due to the formation of $Cd(OH)_2$ or $Pb(OH)_2$. Experimental data shows that precipitation was formed at around pH 8-9. Therefore, all experiments have been done at pH≤7.5 [5.37]. Initially, the metal ions adsorption capacities of hydrochar increase with increasing pH due to functional groups on the adsorbent surface, which interact with the metal ions and improve the surface of hydrochar. The negatively charged functional groups had more affinity towards positively charged or neutral metal species due to electrostatic interaction. For pH < 3.0, the available active sites of the hydrochar are less for metal ions because of the protonation of the active zones at higher H^+ concentrations. At a pH range of 3.0–7.5, connected H^+ will be free from the active sites, and as a result, the adsorbed value of the metal ions will be enhanced. In this pH range, it is assumed that ion exchange and complex formation are the main mechanisms. And finally, at pH > 7.5, a combination of ion exchange and hydroxide formation may become dominant mechanisms for the adsorption of the metal ions. The pH reduction indicates either an increase in H^+ ions or a reduction in OH^- ions. Since hydrolysis occurred during hydrothermal treatment, a decrease in the OH^- ions occurs at the surface. After treatment with Cd^{2+} and Pb^{2+}, the adsorption capacity and removal % rendered by CESH were observed to be higher between pH 6.4 to 7 (Fig. 5.4b). After alkaline treatment, more surface functional groups were available, and the oxygenated functional groups provided a role in proton-donating exchange sites where Pb^{2+} and Cd^{2+} could be chemically adsorbed [5.38]. The pH effect study indicates that the hydrochar has a good possibility for the removal of toxic metal ions (Pb^{2+} and Cd^{2+}) at neutral pH.

5.2.4 Adsorption kinetics for Pb^{2+} and Cd^{2+} ions

The kinetics studies were conducted at different intervals to ascertain the adsorption mechanism. The equilibrium was reached at 120 min for Pb^{2+} and Cd^{2+} ions, respectively as shown in Fig. 5.4c. The non-linearized form of the pseudo-first-order, Eq. 3, non-linear pseudo-second-order, Eq. 4, and intraparticle diffusion equations are given below Eq. 5 [5.39]

$$q_t = q_e(1 - exp(-k_1 t)) \quad (3)$$

$$q_t = \frac{q_e^2 K_2 t}{q_e K_2 t + 1} \quad (4)$$

Intraparticle diffusion is the most widely applied intraparticle diffusion equation for adsorption systems given by Weber and Morris [5.40]

$$q_t = k_i t^{\frac{1}{2}} + C \quad (5)$$

Where q_t (mg g^{-1}) and q_e(mg g^{-1}) are adsorption capacity at time t and equilibrium state respectively, K_1(g/(mg. min)) and K_2 (g/(mg. min)) and K_i (g/(mg.$min^{1/2}$)) are first order, second order, and intraparticle diffusion rate constants respectively. The equations' experimental and fitted linear regression coefficient (R^2) indicates the model's fitness.

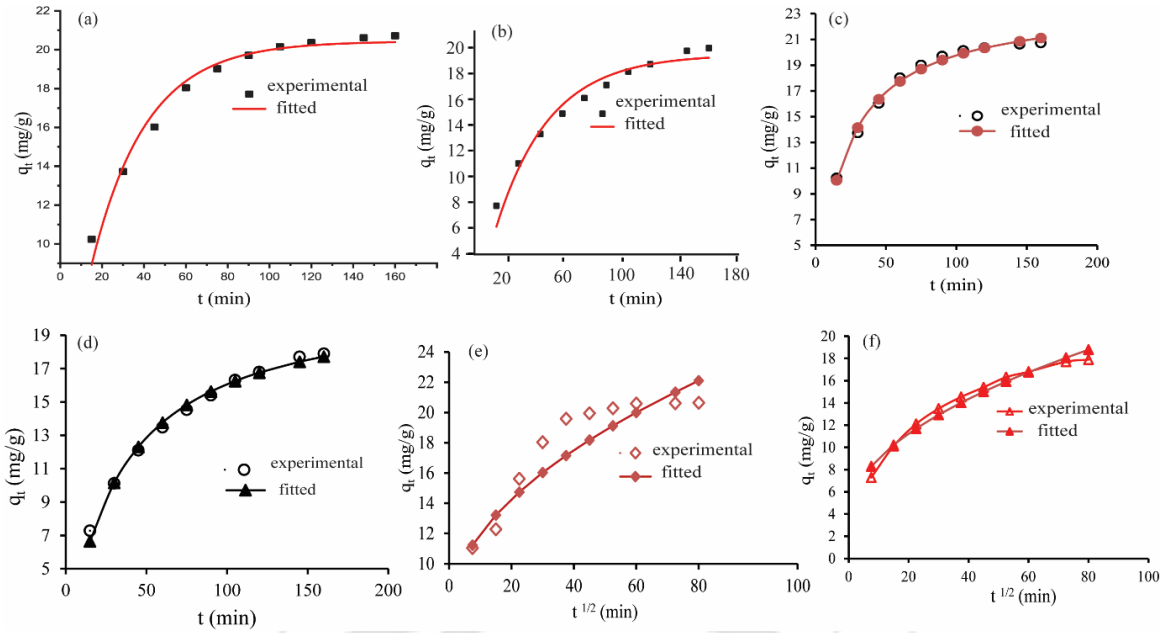

Figure 5.5 Pseudo-first order (a,b), Pseudo-second order (c,d), and Intraparticle discussion (e,f)

Table 5.1 Kinetics parameters for pseudo-first-order, pseudo-second-order, and intraparticle diffusion model.

Kinetics Model	**Kinetic parameters**	**CESH**	
		Cd^{2+}	**Pb^{2+}**
Pseudo First Order	q_e K_1 (L min^{-1}) R^2	20.43 0.038 0.975	17.45 0.027 0.962
Pseudo Second order	q_e K_2 (g $mg^{-1}min^{-1}$) R^2	23.81 0.002 0.992	21.39 0.001 0.993
Intraparticle diffusion	K_i C R^2	0.781 10.33 0.959	1.19 3.64 0.972

5.2.5 Adsorption isotherm

The adsorption capacity can be predicted by two primary methods known as the Langmuir and Freundlich isotherms, which can be explained by using the following two equations (6) and (7):

$$q_e = \frac{q_{max} K_L C_e}{1 + K_L + C_e} \quad (6)$$

$$q_e = K_F \times C_e^{\frac{1}{n}} \quad (7)$$

Where K_L (L mg^{-1}) and K_F (L mg^{-1}) are the Langmuir and Freundlich constant; 1/n is the nonlinearity exponent, C_e is the concentration of metal ions at equilibrium, q_e (mg.g^{-1}), and q_{max} is the adsorption capacity and maximum adsorption capacity at equilibrium, respectively. The isotherm parameters such as K_L, K_F, q_{max}, and R^2 obtained for the isotherm models are listed in Fig. 5.6(a-d) and Table 5.2. Adsorption isotherm experiments were carried out to determine the

maximum adsorption capacity by changing the metal ion concentration, as shown in Fig 5.5 (a), which indicates the experimental data fitted with both Langmuir isotherm and Freundlich isotherm models, respectively, with R^2>0.99. These data show that the Freundlich isotherm model describes toxic metal removal using biochar as it facilitates multilayer/heterogeneous adsorption. Since the Freundlich coefficient (*n*) value was more than 1 indicates favorable toxic metal adsorption.

Table 5.2 Adsorption isotherm parameters for CESH with Cd^{2+} and Pb^{2+}

Isotherm model	**Kinetic parameters**	**CESH**	
		Cd^{2+}	**Pb^{2+}**
Langmuir Isotherm	q_{max} (mg g^{-1})	93.85	84.65
	K_L	0.072	0.085
	R^2	0.975	0.967
Freundlich Isotherm	1/n	0.513	0.483
	K_F	11.32	12.19
	R^2	0.992	0.993

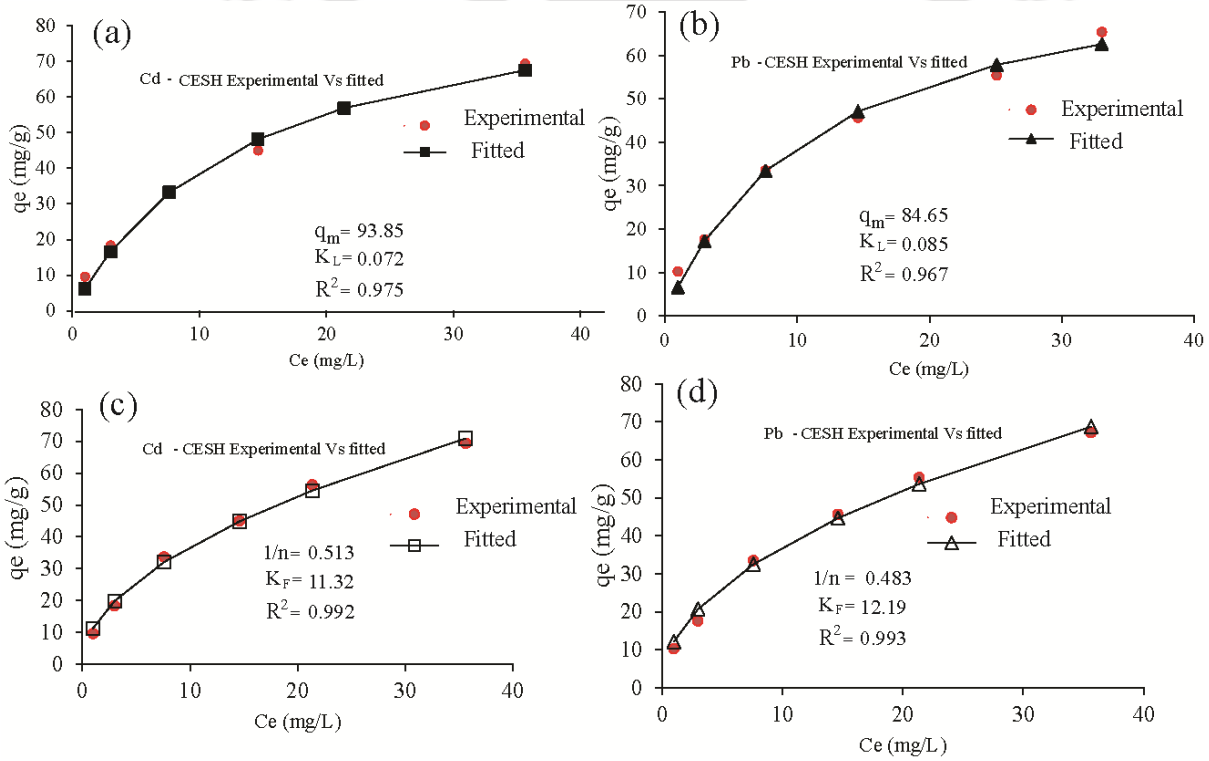

Figure 5.6: Langmuir isotherm of (a) Cd-CESH, (b) Pb-CESH and Freundlich isotherm of (c) Cd-CESH, (d) Pb-CESH

Effect of temperature on heavy metals ions (Cd^{2+} and Pb^{2+}) adsorption was determined at four Different temperature ranges (293-323 K). Thermodynamic studies were conducted to evaluate The feasibility of the process. Table. 5.3 represents the calculated value of ΔG°, ΔH°, and ΔS°. The exothermic adsorption was shown by ΔH°, the negative value of heavy metals ions (Cd^{2+} and Pb^{2+}). The negative value of ΔG° shown indicates that adsorption of heavy metal

is highly favorable and spontaneous, while the negative value of ΔS˚ represents the decrease in randomness with highly ordered reaction

The adsorption capacity depends on the temperature of the solid-liquid interface. Adsorption at different temperatures gives the adsorption feasibility of the system, which exhibits thermodynamic properties. Thermodynamic parameters such as Gibbs free energy (ΔG˚, kJ.mol^{-1}), enthalpy change (ΔH˚ kJ.mol^{-1}), and entropy change (ΔS˚ J.mol^{-1}) were determined by using the Van't Hoff Eq. as [5.41,5.42]

$$\ln K_c = \frac{\Delta S^o}{R} - \frac{\Delta H^o}{RT} \quad (8)$$

$$\Delta G^\circ = -RT\ln(K_c) \quad (9)$$

$$\Delta G^\circ = \Delta H^\circ - T\Delta S^\circ \quad (10)$$

K_c is the equilibrium constant defined by q_e/C_e, qe is the metal ion concentration on the adsorbent at equilibrium, and C_e is the remaining metal ion concentration in the solution. R is the universal gas constant (8.314 J·mol^{-1}·K^{-1}), and T is the temperature in Kelvin (K).

The effect of solution temperature on the adsorption of Cd^{2+} and Pb^{2+} on the CESH surface was investigated at a temperature range of 293K, 303K, 313K, and 323 K, which were summarized in Table 5.3. With the increase in temperature, the adsorption capacity of Cd^{2+} and Pb^{2+} on CESH increases, which suggests the adsorption process is favorable at a higher temperature. This may be due to the heavy metal molecule's tendency to escape from the solid adsorbent surface to the solution phase with an increase in the temperature of the solution [5.43]. The value of ΔH˚ and ΔS˚ were determined from the slope (–ΔH˚/R) and intercept (ΔS˚/R) from the plot of ln (K_c) vs. 1/T (Van't Hoff plot) using Eq. (6). Gibbs free energy, ΔG˚ values were calculated using Eq. (6). The positive ΔH˚ values suggests that the removal of the metal ion by biochar was endothermic, i.e., the adsorption process reached equilibrium by consuming energy from the system itself. The positive ΔS˚ values indicate good affinity between heavy metal ions and biochars and the increase in randomness at the solid-liquid interface. The negative ΔG˚ value indicates that the adsorption of heavy metal ions on RCSB and CESB adsorbents is feasible and spontaneous. Earlier studies show that if the ΔG˚value comes between 0 and –20 kJ.mol$^{-1,}$ adsorption is physical, and if values come between –80 kJ.mol^{-1} and –400 kJ.mol^{-1}, then the adsorption system is chemical adsorption [5.44]. Hence in all cases, the adsorption of heavy metal ions is physical adsorption.

Table 5.3 Thermodynamic parameters of Cd^{2+} and Pb^{2+}

Adsorbent	Temperature (K)	Cd^{2+}			Pb^{2+}		
		ΔG° KJ mol^{-1}	ΔH° KJ mol^{-1}	ΔS° J K^{-1} mol^{-1}	ΔG° KJ mol^{-1}	ΔH° KJ mol^{-1}	ΔS° J K^{-1} mol^{-1}
CESH	293	-8.0305	0.3560	28.6168	-8.4242	0.3811	30.0135
	303	-8.3136			-8.7260		
	333	-8.6026			-9.0253		
	323	-8.8882			-9.3262		

5.3. Fluorescence assay with NCDs

The filtrate obtained after hydrothermal treatment appeared light brown under daylight illumination. The NCDs exhibited a bright green color under UV light at a long wavelength (370 nm). Due to their excellent fluorescence properties, the NCDs were used to detect Hg^{2+} and Fe^{3+}. Hydrothermal treatment time duration, temperature, and weight of material are the synthetic conditions that affect the fluorescence properties of NCDs [5.45]. The optimum FL intensity of 4 gm CES powder was reached within 8 hrs at 200˚C. The extended hydrothermal treatment and the increase in temperature can produce more carbon nuclei and cause an increase of FL intensity. A short time duration and low temperature may lead to low reaction efficiency and inadequate precursor carbonization, thus causing low FL properties [5.22]. The fluorescence intensities were recorded at room temperature. Fluorescence experiments were carried out using 2.1 ml of NCDs solutions with 0.9 ml of toxic metal ions of As^{2+}, Co^{2+}, Cd^{2+}, Cr^{3+}, Hg^{2+}, Al^{3+}, Ni^{2+}, Pb^{2+}, Zn^{2+}, Fe^{3+}, and $Ag^{+,}$ respectively. The fluorescence emission intensity of (a) NCDs (Blank metal ions) under normal light and (b) NCDs (Blank metal ions) under UV light are shown in Fig.A5.11. The concentration of the metal ions was kept at 300 µM. After 2 minutes of addition, the fluorescence intensity of mixed solutions was measured with excitation at 370 nm.

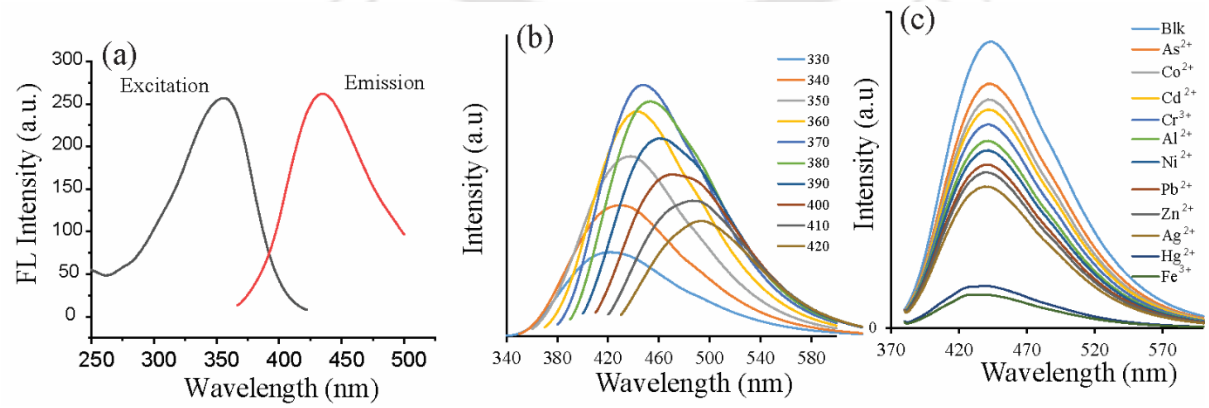

Figure 5.7 (a) FL excitation and emission spectra of NCDs, (b) FL spectra of NCDs at various excitation wavelengths from 330 to 420 nm with a 10 nm increase, and (c) FL intensity of NCD after the addition of different metal ions.

5.3.1 Optimizing experimental conditions

Experiments were performed at different temperatures (140, 160, 180, and 200 °C) and heating time durations (4, 8, 12, and 16 hrs) with *Colocasia esculanta* stem powder (0.25, 0.5, 1.0, and 1.5 gm) to get an optimized result (Fig. A5.9).

We have added 900 µL (300 µM) of Hg^{2+} and Fe^{3+} solutions into 2.1 mL of 20 µg/mL NCDs. After 2 min, the fluorescence intensity of the resulting solutions was measured with excitation wavelength at 367 nm; both excitation and emission slit widths were 5 nm.

5.3.2 Detection of Hg^{2+} and Fe^{3+} in environmental water sample

We have collected distilled water, tap water, and lake water from the IIT Guwahati campus. All samples were centrifuged at 10,000 rpm for 15 minutes and filtered through 0.22 µm membrane filter paper. N-doped CD (2.9 ml) solutions were mixed with 0.1 ml samples, and fluorescence emission intensity at λ_{em} = 445 nm was measured with an excitation wavelength λ_{ex}=360 nm.

5.3.3 Spectroscopic Studies

The UV-Vis spectra of NCDs exhibit a broad absorption band from 220 to 380 nm and a tail extended to the visible region. Two distinctive absorbance peaks were seen at 225 and 274 nm. The peak at 225 nm originated from the σ-σ* energy transition [5.46]. The sharp absorbance peak

Table 5.4: Comparison of the method in this work with reported methods

Materials	Analytes	LOD (µM)	Linear range (µM)	Response Time (min)	Ref.
NCDs	Fe^{3+}	0.31	3-60	1	[5.49]
F-CDs	Fe^{3+}	0.01	1-100	10	[5.50]
N-CDs	Hg^{2+}	0.05	20-50	-	[5.51]
CDs	Hg^{2+}	0.06	0.1-20	6	[5.51]
Nitrogen and sulfur co-doped carbon dots	Hg^{2+}	0–20	0.18		[5.52]
C-dots	Hg^{2+}	0.0028	0.07-7	4	[5.53]
NCQDs	Hg^{2+} Fe^{3+}	0.017 0.50	0-5 0-70	2 1	[5.54]
Rice straw	Fe^{3+}	0.2	0–9	-	[5.55]
Colocasia esculanta Stem CD	Hg^{2+} Fe^{3+}	0.012 0.35	0-10 0-10	2 2	This work

at 274 nm originated from the π-π* energy transition of the conjugated C=C bonds, confirming the existence of the aromatic π system in the core of N-CDs [5.47]. The FL intensities of NCDs were measured in the presence of metal ions As^{2+}, Co^{2+}, Cd^{2+}, Cr^{3+}, Hg^{2+}, Al^{3+}, Ni^{2+}, Pb^{2+}, Zn^{2+},

$Fe^{3+,}$ and Ag^{2+}respectively with the same concentration of 100 µM (Fig. 6c). NCDs' maximum fluorescence emission wavelength was 445 nm, with an excitation wavelength of 367 nm (Fig.5.7 a). The FL intensities decrease more than other metal ions after adding Hg^{2+} and Fe^{3+} ions. Moreover, a fluorescence titration experiment was performed with an increasing concentration (0.1–10 µM) of Hg^{2+} and Fe^{3+} ions to explain the fluorescence response of synthesized NCDs. The fluorescence intensity decreased after the incremental addition of Hg^{2+} and Fe^{3+} (Fig. 5.7c). The synthesized NCDs show an absorbance band at 274 nm (Fig. A5.7) attributed to the π-π* transition of the C=C band [5.48].

This selective effect can be assigned due to the stronger affinity of Hg^{2+} and Fe^{3+} ions and faster binding process with the NCDs' surface carboxylate and hydroxyl groups compared to the other metal cations. [5.56]. The Stern–Volmer (S–V) equation was used to investigate the relationship between the quenching effect of the NCDs with Hg^{2+} and Fe^{3+} [5.57].

$$\left(\frac{Io}{I}\right) = Ksv(M) + 1 \qquad (11)$$

Where I_o is the initial FL intensity of the NCDs, I is the intensity after the addition of the metal ions, [M] represents the concentration of the Hg^{2+} and Fe^{3+} ions, and K_{SV} denotes the Stern–Volmer constant. The Stern–Volmer plot indicated a linear relationship between the fluorescence quenching and the concentration of Hg^{2+} and Fe^{3+}. Using equation (5), a high correlation coefficient was recorded for the tested metal ions (R^2 = 0.993 for Hg^{2+} and R^2 = 0.995 for Fe^{3+}), and the K_{sv} value was found to be 15.5×10^3 mol^{-1} for Hg^{2+} and 13.5×10^3 mol^{-1} for Fe^{3+}. Determination of the limit of detection (LOD) is critical for the potential application of the synthesized NCD. Therefore, the below-mentioned equation was used to determine the LOD.

$$\text{LOD}= \frac{3\sigma}{m} \qquad (12)$$

Where σ is the standard deviation of the blank measurements and m is the slope determined for LOD measurement at a lower concentration. The detection limit of the synthesized NCDs for Hg^{2+} and Fe^{3+} ions was calculated as 55 nM and 35 nM, respectively. The NCDs' sensing potential is comparable with that of the previously reported CD-based probing systems for detecting Hg^{2+} and Fe^{3+}ions (Table 5.4).

5.3.4 Quantum yield measurement

The quantum yield QY(Φ) was calculated by comparing it with the reference sample quinine sulfate as shown in equation 13. Both the reference material and sample material were excited at the same wavelength. QY(Φ) of CDs was calculated using a standard formula shown below. (Φ = 54% in 0.1 M H_2SO_4) at the excitation wavelength of 360 nm.

$$\Phi_S = \Phi_R \times \frac{I_S}{I_R} \times \frac{Abs_R}{Abs_S} \times \frac{\eta_S^2}{\eta_R^2} \qquad (13)$$

Φ_R and Φ_S indicate the quantum yield of the reference and sample; I_s and I_R refers integrated fluorescence intensity of the sample, and reference A_S and A_R refer to the area under the emission peak of the sample and reference; Abs_R and Abs_S are the absorbance reading of the reference and sample, respectively; at an excitation wavelength of 360 nm at a slit width of 2 nm and η refers to the refractive index of the solvent (1.33 for both the sample and reference). The quantum yield (Φ) of quinine sulfate was 54%. The resulting carbon dots exhibit stable fluorescence with a quantum yield of 15.5%

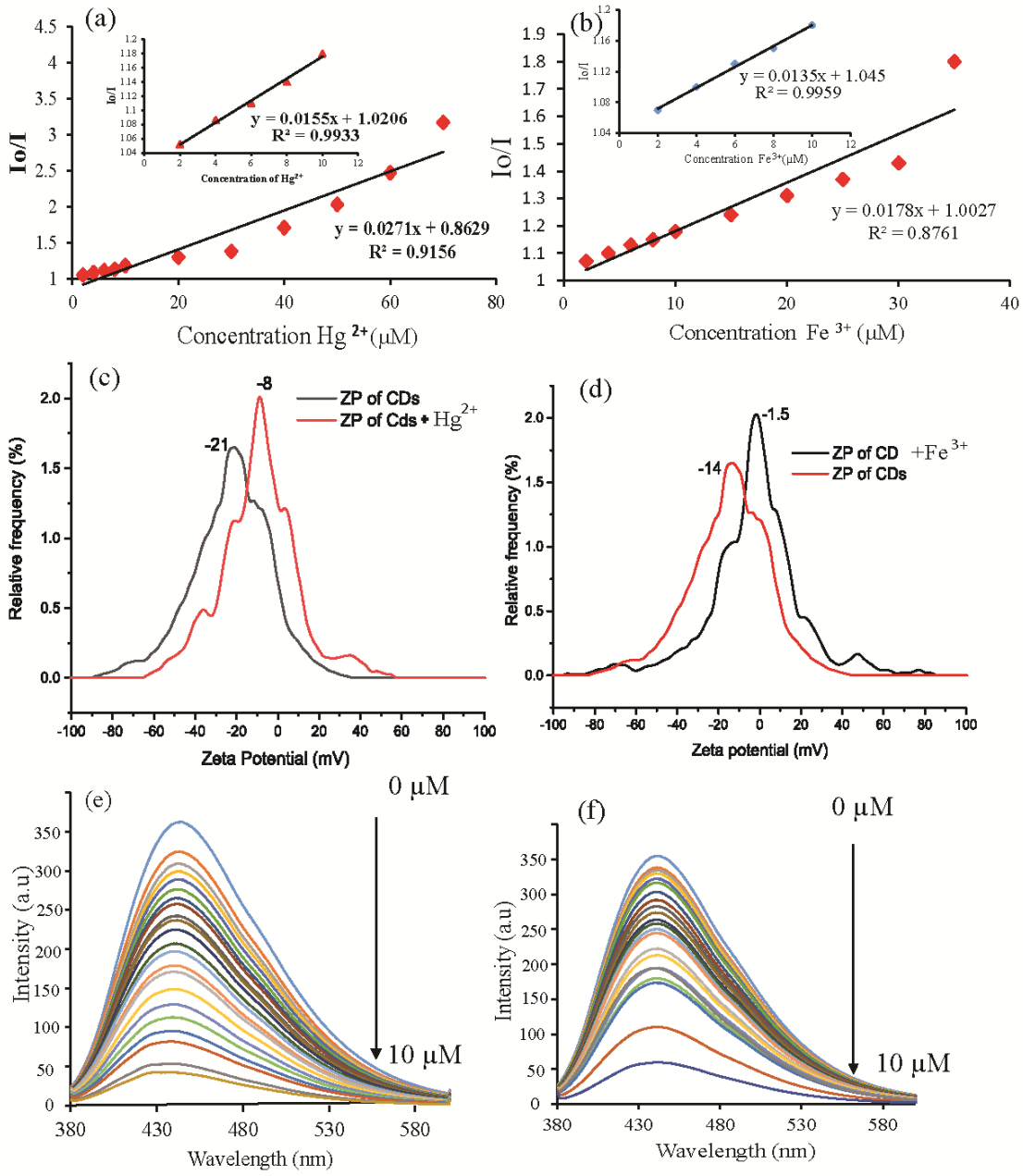

Figure 5.8 (a,b) Stern–Volmer plot representing the linear relationship between I_0/I value and the concentration of Hg^{2+} and Fe^{3+} ions (c,d) Zeta potential plot of the NCDs before and after the addition of Hg^{2+} and Fe^{3+} ions and (e,f) fluorescence titration experiment with a slow increase in the concentration of Hg^{2+} and Fe^{3+} ions (0–10 μM).

5.3.5. Mechanism of quenching

To explain the quenching mechanism of the synthesized NCD, the time-resolved photoluminescence (TRPL) study was performed in the presence of Fe^{3+} ions. The fluorescence decay pattern of the NCDs shows a slight change after an incremental addition (5–20 µM) of Fe^{3+} ions (Fig. 8). The photoluminescence (PL) decay was fitted with a bi-exponential function, and the average fluorescence lifetime (t) is calculated using the following eq. [5.58]

$$\tau = \frac{\alpha 1\ \tau 1^2 + \alpha 2\ \tau 2^2}{\alpha 1 \tau 1 + \alpha 2 \tau^2} \quad (8)$$

The values of the fitting parameter (χ^2), exciton lifetimes (τ_1, τ_2), and pre-exponential factors (α_1, α_2) are indicated in Table 5.5. The photoluminescence lifetime decay of the as-prepared NCDs was calculated to be 5.194 ns. The nearby PL lifetimes concentrations of Fe^{3+} ions (5–20 µM) are found to be 5.194, 5.138, 5.053, 4.995, and 4.79 ns, respectively, which establish the static quenching effect [5.59,5.60] of the NCDs due to the formation of non-fluorescent NCD– Fe^{3+} complexes [5.56].

Table 5.5 Photoluminescence (PL) lifetime decay analysis of NCDs with different concentrations of Fe^{3+}

Sample	χ^2	τ_1(ns)	τ_2(ns)	α_1 (%)	α_2 (%)	τ (ns)
NCDs	1.001	1.1553	1.204	85.4755	86.284	5.194
NCDs + 5µM Fe^{3+}	1.00	1.1098	1.103	88.60	85.119	5.138
NCDs + 10µM Fe^{3+}	1.00	1.0571	1.022	93.870	87.620	5.053
NCDs + 15µM Fe^{3+}	1.002	1.0633	1.078	85.3821	83.520	4.995
NCDs + 20µM Fe^{3+}	0.999	0.9931	1.140	74.2237	81.817	4.779

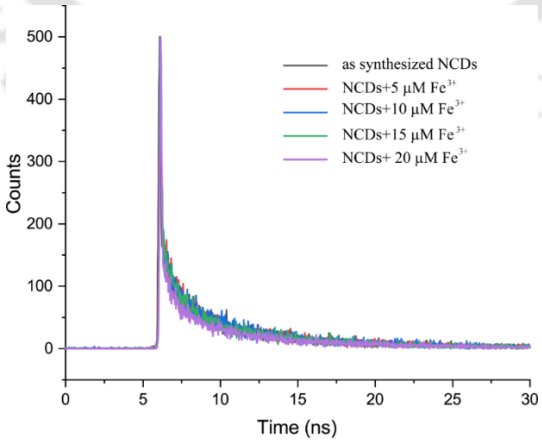

Fig. 5.9 Time-resolved photoluminescence (TRPL) decay of the NCDs after incremental addition of Fe^{3+} ions.

5.3.6 Environmental water sample analysis

The synthesized NCDs from the *Colocasia esculanta* stem were utilized in the sensing application of Hg^{2+} and Fe^{3+} ions in different water samples. Water samples from various sources, namely laboratory tap water and lake water (IIT Guwahati Lake), were collected and filtered with a 0.22 mm nylon membrane to remove solids. The pH of the water samples was adjusted to pH 6.8 using 0.01 N HCl/0.1N NaOH. The water samples were spiked with 10 µM of Hg^{2+} and Fe^{3+} ions and added to the solution of NCDs to observe the fluorescence change. The emission intensity of NCDs was quenched by 83%, 81%, and 79% for the distilled water, tap water, and lake water, respectively (Fig. A5.10). The results indicate that the presence of Hg^{2+} and Fe^{3+} in water samples (tap water and lake water) gave a stable and robust fluorescence response compared with the control (deionized water). Furthermore, the filtered water samples were spiked with different concentrations of Hg^{2+} and Fe^{3+} ions (100, 200, and 300 nM) and added into the probing system to record the resulting fluorescence response (Table 5.6).

Table 5.6. Comparison of the Hg^{2+} and Fe^{3+} detection performance using CD and AAS-based method

Metal ions	Water samples	Spiked level	CD based method			AAS-based method		
			Spike detected (nM)	Spike recovery (%)	%RSD (n=5)	Spike detected (nM)	Spike recovery (%)	%RSD
Hg^{2+}	Distilled water	100 200 300	96.8 197.65 295.20	96.8 98.82 98.40	1.45 1.98 2.42	100.23 201.58 298.41	100.23 100.79 99.47	0.87 1.28 1.56
	Tap water	100 200 300	96.21 195.74 299.63	96.21 97.87 99.87	1.81 2.86 3.20	101.36 198.47 300.26	101.66 99.23 100.08	1.23 1.52 2.19
	Lake water	100 200 300	96.62 201.53 303.56	96.62 100.76 101.18	2.58 2.06 3.32	99.87 200.57 298.36	99.87 100.28 99.45	2.26 1.56 2.95
Fe^{3+}	Distilled water	100 200 300	97.5 199.36 298.3	97.5 99.68 99.43	1.35 1.94 2.35	100.14 200.42 299.58	100.23 100.79 99.47	0.82 1.31 1.65
	Tap water	100 200 300	99.69 198.69 299.87	99.69 99.34 99.95	1.78 2.76 3.09	100.63 199.63 300.98	101.66 99.23 100.08	1.29 1.62 2.22
	Lake water	100 200 300	96.62 198.63 299.32	96.62 99.30 99.77	2.69 2.09 3.23	99.56 200.45 299.78	99.87 100.28 99.45	2.30 1.62 2.98

5.4 Conclusion

Our studies demonstrate that Hydrochar prepared from *Colocasia esculanta* stem through a facile, economical, and eco-friendly hydrothermal method can efficiently remove toxic metal ions like

Pd^{2+} and Cd^{2+}. Nitrogen-doped carbon dots synthesized from the filtrate can selectively sense Hg^{2+} and Fe^{3+} ions in aqueous medium and environmental water samples. The detection limit of Hg^{2+} ion was ~12 nM, comparable to the safe limit (~10 nM) set by WHO. Based on the results emerging from the current study, it was evident that NCD based sensing method is highly sensitive in practical applications.

Reference:

[5.1] H. Medhi, P.R. Chowdhury, P.D. Baruah, K.G. Bhattacharyya, Kinetics of Aqueous Cu(II) Biosorption onto Thevetia peruviana Leaf Powder, (2020). https://doi.org/10.1021/acsomega.9b04032.

[5.2] G. Crini, E. Lichtfouse, Advantages and disadvantages of techniques used for wastewater treatment, Environ. Chem. Lett. 17 (2019) 145–155.

[5.3] X. Wang, W. Deng, Y. Xie, C. Wang, Selective removal of mercury ions using a chitosan--poly (vinyl alcohol) hydrogel adsorbent with three-dimensional network structure, Chem. Eng. J. 228 (2013) 232–242.

[5.4] S.E. Bailey, T.J. Olin, R.M. Bricka, D.D. Adrian, A review of potentially low-cost sorbents for heavy metals, Water Res. 33 (1999) 2469–2479.

[5.5] S.Y. Quek, B. Al-Duri, D.A.J. Wase, C.F. Forster, Coir as a biosorbent of copper and lead, Process Saf. Environ. Prot. 76 (1998) 50–54.

[5.6] J.M. Randall, B. RL, others, Use of bark to remove heavy metal ions from waste solutions, (1974).

[5.7] S. Senthilkumaar, S. Bharathi, D. Nithyanandhi, V. Subburam, Biosorption of toxic heavy metals from aqueous solutions, Bioresour. Technol. 75 (2000) 163–165.

[5.8] X. Xu, R. Ray, Y. Gu, H.J. Ploehn, L. Gearheart, K. Raker, W.A. Scrivens, Electrophoretic analysis and purification of fluorescent single-walled carbon nanotube fragments, J. Am. Chem. Soc. 126 (2004) 12736–12737. https://doi.org/10.1021/ja040082h.

[5.9] W. Lu, X. Qin, S. Liu, G. Chang, Y. Zhang, Y. Luo, A.M. Asiri, A.O. Al-Youbi, X. Sun, Economical, green synthesis of fluorescent carbon nanoparticles and their use as probes for sensitive and selective detection of mercury(II) ions, Anal. Chem. 84 (2012) 5351–5357. https://doi.org/10.1021/ac3007939.

[5.10] S. Sahu, B. Behera, T.K. Maiti, S. Mohapatra, Simple one-step synthesis of highly luminescent carbon dots from orange juice: application as excellent bio-imaging agents, Chem. Commun. 48 (2012) 8835. https://doi.org/10.1039/c2cc33796g.

[5.11] B. De, N. Karak, A green and facile approach for the synthesis of water soluble fluorescent carbon dots from banana juice, RSC Adv. 3 (2013) 8286–8290. https://doi.org/10.1039/c3ra00088e.

[5.12] H. Guo, B. You, S. Zhao, Y. Wang, G. Sun, Y. Bai, L. Shi, Full-color tunable photoluminescent carbon dots based on oil/water interfacial synthesis and their applications, RSC Adv. 8 (2018) 24002–24012. https://doi.org/10.1039/C8RA03723J.

[5.13] J. Shen, Y. Zhu, X. Yang, C. Li, Graphene quantum dots: emergent nanolights for bioimaging{,} sensors{,} catalysis and photovoltaic devices, Chem. Commun. 48 (2012) 3686–3699. https://doi.org/10.1039/C2CC00110A.

[5.14] C.S. Lim, K. Hola, A. Ambrosi, R. Zboril, M. Pumera, Graphene and carbon quantum dots electrochemistry, Electrochem. Commun. 52 (2015) 75–79. https://doi.org/https://doi.org/10.1016/j.elecom.2015.01.023.

[5.15] J. Pan, Y. Sheng, J. Zhang, J. Wei, P. Huang, X. Zhang, B. Feng, Preparation of carbon quantum dots/ TiO2 nanotubes composites and their visible light catalytic applications, J. Mater. Chem. A. 2 (2014) 18082–18086. https://doi.org/10.1039/C4TA03528C.

[5.16] J. Shen, S. Shang, X. Chen, D. Wang, Y. Cai, Facile synthesis of fluorescence carbon dots from sweet potato for Fe3 +sensing and cell imaging, Mater. Sci. Eng. C. 76 (2017) 856–864. https://doi.org/10.1016/j.msec.2017.03.178.

[5.17] L.-H. Mao, W.-Q. Tang, Z.-Y. Deng, S.-S. Liu, C.-F. Wang, S. Chen, Facile Access to White Fluorescent Carbon Dots toward Light-Emitting Devices, Ind. Eng. Chem. Res. 53 (2014) 6417–6425. https://doi.org/10.1021/ie500602n.

[5.18] S. Liu, J. Tian, L. Wang, Y. Zhang, X. Qin, Y. Luo, A.M. Asiri, A.O. Al-Youbi, X. Sun, Hydrothermal treatment of grass: A low-cost, green route to nitrogen-doped, carbon-rich, photoluminescent polymer nanodots as an effective fluorescent sensing platform for label-free detection of Cu(II) ions, Adv. Mater. 24 (2012) 2037–2041. https://doi.org/10.1002/adma.201200164.

[5.19] M. Liu, Y. Xu, F. Niu, J.J. Gooding, J. Liu, Carbon quantum dots directly generated from electrochemical oxidation of graphite electrodes in alkaline alcohols and the applications for specific ferric ion detection and cell imaging, Analyst. 141 (2016) 2657–2664. https://doi.org/10.1039/C5AN02231B.

[5.20] C. López, M. Zougagh, M. Algarra, E. Rodríguez-Castellón, B.B. Campos, J.C.G. Esteves da Silva, J. Jiménez-Jiménez, A. Ríos, Microwave-assisted synthesis of carbon dots and its potential as analysis of four heterocyclic aromatic amines., Talanta. 132 (2015) 845–850. https://doi.org/10.1016/j.talanta.2014.10.008.

[5.21] M.P. Sk, A. Chattopadhyay, Induction coil heater prepared highly fluorescent carbon dots as invisible ink and explosive sensor, RSC Adv. 4 (2014) 31994–31999. https://doi.org/10.1039/C4RA04264F.

[5.22] T. Ogi, K. Aishima, F.A. Permatasari, F. Iskandar, E. Tanabe, K. Okuyama, Kinetics of nitrogen-doped carbon dot formation via hydrothermal synthesis, New J. Chem. 40 (2016) 5555–5561. https://doi.org/10.1039/C6NJ00009F.

[5.23] Z. Yang, Z. Li, M. Xu, Y. Ma, J. Zhang, Y. Su, F. Gao, H. Wei, L. Zhang, Controllable synthesis of fluorescent carbon dots and their detection application as nanoprobes, Nano-Micro Lett. 5 (2013) 247–259.

[5.24] Y.-P. Sun, X. Wang, F. Lu, L. Cao, M.J. Meziani, P.G. Luo, L. Gu, L.M. Veca, Doped carbon nanoparticles as a new platform for highly photoluminescent dots, J. Phys. Chem. C. 112 (2008) 18295–18298.

[5.25] L. Wu, X. Cai, K. Nelson, W. Xing, J. Xia, R. Zhang, A.J. Stacy, M. Luderer, G.M. Lanza, L. V Wang, others, A green synthesis of carbon nanoparticles from honey and their use in real-time photoacoustic imaging, Nano Res. 6 (2013) 312–325.

[5.26] Q. Xu, J. Zhao, Y. Liu, P. Pu, X. Wang, Y. Chen, C. Gao, J. Chen, H. Zhou, Enhancing the luminescence of carbon dots by doping nitrogen element and its application in the detection of Fe (III), J. Mater. Sci. 50 (2015) 2571–2576.

[5.27] J. Liao, Z. Cheng, L. Zhou, Nitrogen-doping enhanced fluorescent carbon dots: green synthesis and their applications for bioimaging and label-free detection of Au3+ ions, ACS Sustain. Chem. \& Eng. 4 (2016) 3053–3061.

[5.28] P. Roy, P.C. Chen, A.P. Periasamy, Y.N. Chen, H.T. Chang, Photoluminescent carbon nanodots: Synthesis, physicochemical properties and analytical applications, Mater. Today. 18 (2015) 447–458. https://doi.org/10.1016/j.mattod.2015.04.005.

[5.29] B. De, N. Karak, A green and facile approach for the synthesis of water soluble fluorescent carbon dots from banana juice, RSC Adv. 3 (2013) 8286–8290. https://doi.org/10.1039/C3RA00088E.

[5.30] G. Somaraj, S. Mathew, T. Abraham, K.G. Ambady, C. Mohan, B. Mathew, Nitrogen and Sulfur Co-Doped Carbon Quantum Dots for Sensing Applications: A Review, ChemistrySelect. 7 (2022). https://doi.org/10.1002/slct.202200473.

[5.31] J. Zhu, H. Chu, T. Wang, C. Wang, Y. Wei, Fluorescent probe based nitrogen doped carbon

quantum dots with solid-state fluorescence for the detection of Hg2+ and Fe3+ in aqueous solution, Microchem. J. 158 (2020) 105142. https://doi.org/10.1016/j.microc.2020.105142.

[5.32] A. Mewada, S. Pandey, S. Shinde, N. Mishra, G. Oza, M. Thakur, M. Sharon, M. Sharon, Green synthesis of biocompatible carbon dots using aqueous extract of Trapa bispinosa peel, Mater. Sci. Eng. C. 33 (2013) 2914–2917. https://doi.org/10.1016/j.msec.2013.03.018.

[5.33] V. Ramanan, B. Siddaiah, K. Raji, P. Ramamurthy, Green synthesis of multifunctionalized, nitrogen-doped, highly fluorescent carbon dots from waste expanded polystyrene and its application in the fluorimetric detection of Au3+ ions in aqueous media, ACS Sustain. Chem. \& Eng. 6 (2018) 1627–1638.

[5.34] H. Li, Z. Kang, Y. Liu, S.-T. Lee, Carbon nanodots: synthesis, properties and applications, J. Mater. Chem. 22 (2012) 24230–24253. https://doi.org/10.1039/c2jm34690g.

[5.35] S. Lu, G. Xiao, L. Sui, T. Feng, X. Yong, S. Zhu, B. Li, Z. Liu, B. Zou, M. Jin, others, Piezochromic carbon dots with two-photon fluorescence, Angew. Chemie. 129 (2017) 6283–6287.

[5.36] X. Gong, W. Lu, M.C. Paau, Q. Hu, X. Wu, S. Shuang, C. Dong, M.M.F. Choi, Facile synthesis of nitrogen-doped carbon dots for Fe3+ sensing and cellular imaging, Anal. Chim. Acta. 861 (2015) 74–84.

[5.37] M. Kavand, P. Eslami, L. Razeh, The adsorption of cadmium and lead ions from the synthesis wastewater with the activated carbon: Optimization of the single and binary systems, J. Water Process Eng. 34 (2020) 101151. https://doi.org/10.1016/j.jwpe.2020.101151.

[5.38] T. Sizmur, T. Fresno, G. Akgül, H. Frost, E. Moreno-Jiménez, Biochar modification to enhance sorption of inorganics from water, Bioresour. Technol. 246 (2017) 34–47.

[5.39] A.R.P. Hidayat, D.O. Sulistiono, I.K. Murwani, B.F. Endrawati, H. Fansuri, L.L. Zulfa, R. Ediati, Linear and nonlinear isotherm, kinetic and thermodynamic behavior of methyl orange adsorption using modulated Al2O3@UiO-66 via acetic acid, J. Environ. Chem. Eng. 9 (2021) 106675. https://doi.org/10.1016/j.jece.2021.106675.

[5.40] W.J. Weber Jr, J.C. Morris, Kinetics of adsorption on carbon from solution, J. Sanit. Eng. Div. 89 (1963) 31–59.

[5.41] A. Jawed, L.M. Pandey, Application of bimetallic Al-doped ZnO nano-assembly for heavy metal removal and decontamination of wastewater, Water Sci. Technol. 80 (2019) 2067–2078.

[5.42] A. Regti, A. El Kassimi, M.R. Laamari, M. El Haddad, Competitive adsorption and optimization of binary mixture of textile dyes: A factorial design analysis, J. Assoc. Arab Univ. Basic Appl. Sci. 24 (2016) 1–9. https://doi.org/10.1016/j.jaubas.2016.07.005.

[5.43] A.K. Kushwaha, N. Gupta, M.C. Chattopadhyaya, Adsorption behavior of lead onto a new class of functionalized silica gel, Arab. J. Chem. 10 (2017) S81–S89. https://doi.org/10.1016/J.ARABJC.2012.06.010.

[5.44] D. Sachan, A. Ghosh, G. Das, Valorization of aquatic weed Salvinia minima to value-added eco-friendly biosorbent: preferential removal of dye and heavy metal, Int. J. Environ. Sci. Technol. (2022). https://doi.org/10.1007/s13762-022-04126-7.

[5.45] Q. Wu, W. Li, P. Wu, J. Li, S. Liu, C. Jin, X. Zhan, Effect of reaction temperature on properties of carbon nanodots and their visible-light photocatalytic degradation of tetracyline, RSC Adv. 5 (2015) 75711–75721. https://doi.org/10.1039/C5RA16080D.

[5.46] Isnaeni, Y. Herbani, M.M. Suliyanti, Concentration effect on optical properties of carbon dots at room temperature, J. Lumin. 198 (2018) 215–219. https://doi.org/10.1016/j.jlumin.2018.02.012.

[5.47] V.A. Ansi, N.K. Renuka, Table sugar derived Carbon dot – a naked eye sensor for toxic Pb2+ ions, Sensors Actuators, B Chem. 264 (2018) 67–75. https://doi.org/10.1016/j.snb.2018.02.167.

[5.48] D. Wang, X. Wang, Y. Guo, W. Liu, W. Qin, RSC Advances their sulphur and nitrogen doped analogues †, (2014) 51658–51665. https://doi.org/10.1039/c4ra11158c.

[5.49] R. Bandi, R. Dadigala, B.R. Gangapuram, F.K. Sabir, M. Alle, S.-H. Lee, V. Guttena, N-Doped carbon dots with pH-sensitive emission, and their application to simultaneous fluorometric

determination of iron (III) and copper (II), Microchim. Acta. 187 (2020) 1–10.

[5.50] D. Hong, X. Deng, J. Liang, J. Li, Y. Tao, K. Tan, One-step hydrothermal synthesis of down/up-conversion luminescence F-doped carbon quantum dots for label-free detection of Fe3+, Microchem. J. 151 (2019) 104217.

[5.51] A. Pankaj, K. Tewari, S. Singh, S.P. Singh, Waste candle soot derived nitrogen doped carbon dots based fluorescent sensor probe: An efficient and inexpensive route to determine Hg (II) and Fe (III) from water, J. Environ. Chem. Eng. 6 (2018) 5561–5569.

[5.52] Y. Wang, S.-H. Kim, L. Feng, Highly luminescent N, S-Co-doped carbon dots and their direct use as mercury (II) sensor, Anal. Chim. Acta. 890 (2015) 134–142.

[5.53] B. Zhu, G. Ren, M. Tang, F. Chai, F. Qu, C. Wang, Z. Su, Fluorescent silicon nanoparticles for sensing Hg2+ and Ag+ as well visualization of latent fingerprints, Dye. Pigment. 149 (2018) 686–695.

[5.54] J. Zhu, H. Chu, T. Wang, C. Wang, Y. Wei, Fluorescent probe based nitrogen doped carbon quantum dots with solid-state fluorescence for the detection of Hg2+ and Fe3+ in aqueous solution, Microchem. J. 158 (2020). https://doi.org/10.1016/j.microc.2020.105142.

[5.55] R. Liu, M. Gao, J. Zhang, Z. Li, J. Chen, P. Liu, D. Wu, An ionic liquid promoted microwave-hydrothermal route towards highly photoluminescent carbon dots for sensitive and selective detection of iron (III), RSC Adv. 5 (2015) 24205–24209.

[5.56] Y. Liu, Q. Zhou, Y. Yuan, Y. Wu, Hydrothermal synthesis of fluorescent carbon dots from sodium citrate and polyacrylamide and their highly selective detection of lead and pyrophosphate, Carbon N. Y. 115 (2017) 550–560.

[5.57] S. Li, L. Lu, M. Zhu, C. Yuan, S. Feng, A bifunctional chemosensor for detection of volatile ketone or hexavalent chromate anions in aqueous solution based on a Cd (II) metal--organic framework, Sensors Actuators B Chem. 258 (2018) 970–980.

[5.58] A. Ghosh, G. Das, Environmentally benign synthesis of fluorescent carbon nanodots using waste PET bottles: highly selective and sensitive detection of Pb^{2+} ions in an aqueous medium , New J. Chem. 45 (2021) 8747–8754. https://doi.org/10.1039/d1nj00961c.

[5.59] Y. Hu, Z. Gao, J. Yang, H. Chen, L. Han, Environmentally benign conversion of waste polyethylene terephthalate to fluorescent carbon dots for “on-off-on” sensing of ferric and pyrophosphate ions, J. Colloid Interface Sci. 538 (2019) 481–488. https://doi.org/10.1016/j.jcis.2018.12.016.

[5.60] X. Luo, Y. Han, X. Chen, W. Tang, T. Yue, Z. Li, Carbon dots derived fluorescent nanosensors as versatile tools for food quality and safety assessment: A review, Trends Food Sci. Technol. 95 (2020) 149–161. https://doi.org/10.1016/j.tifs.2019.11.017.

Annexure 5

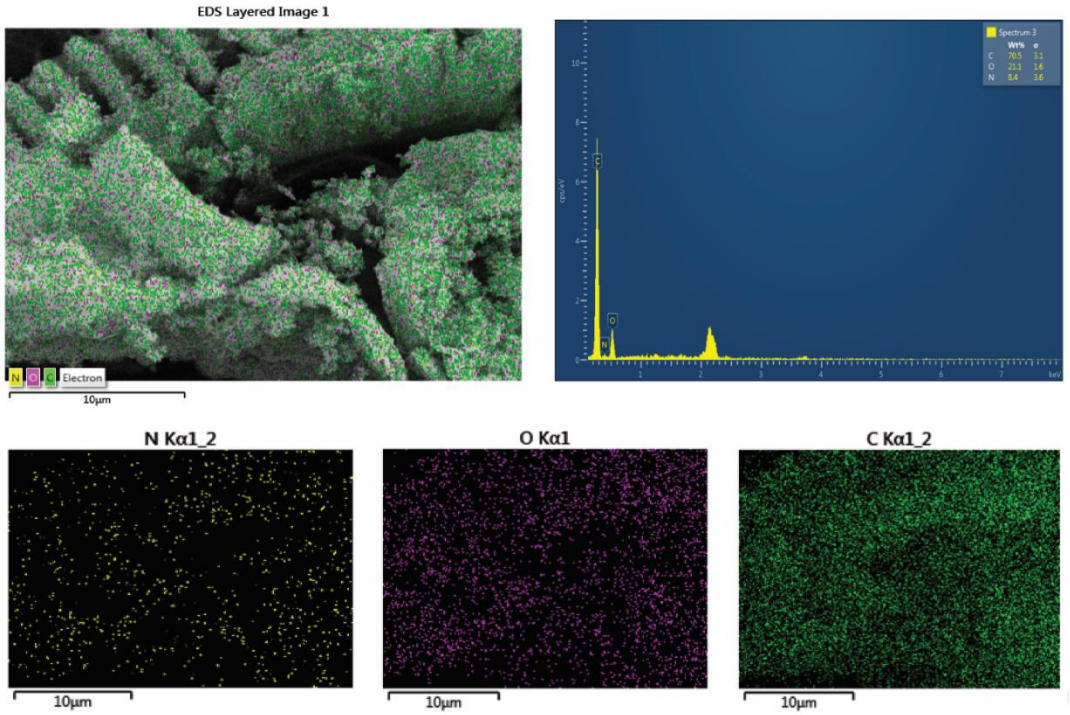

Figure A5.1 EDAX and elemental mapping image of CESH

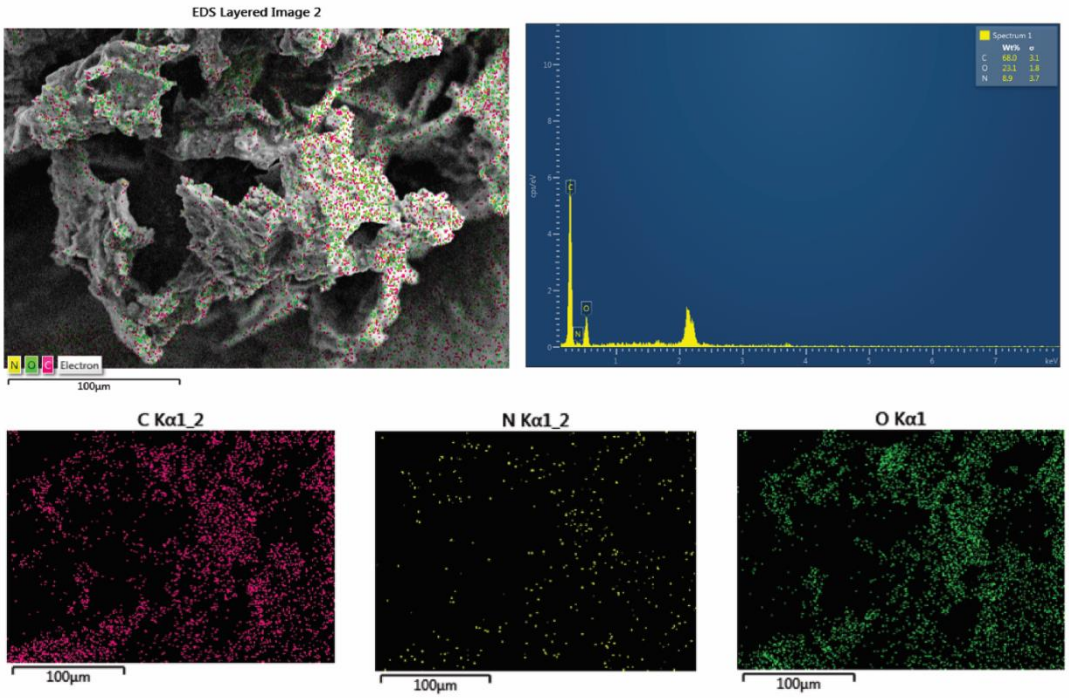

Figure A5.2 EDAX and elemental mapping image of NCD

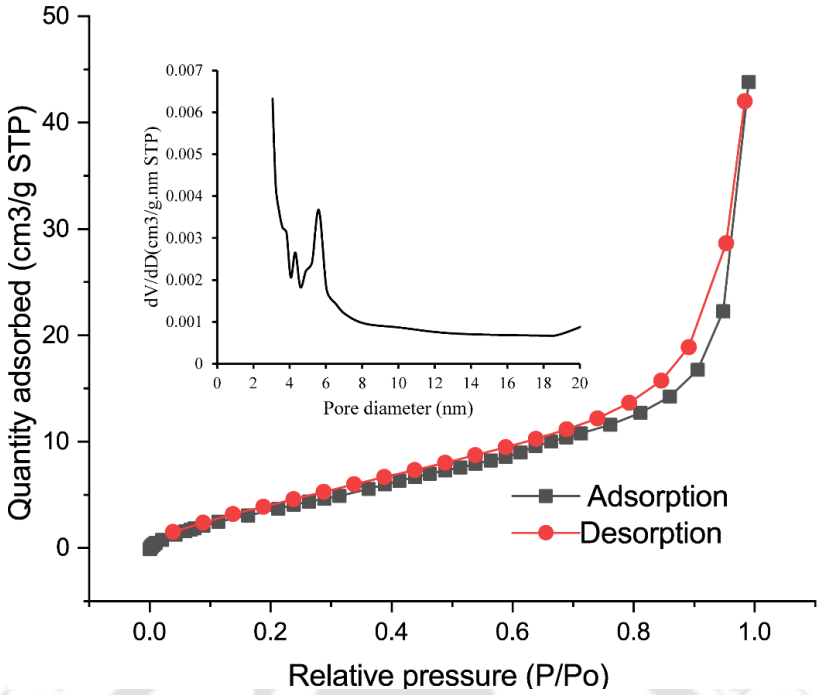

Figure A5.3 Nitrogen adsorption-desorption isotherm (INSET: pore-size distribution curve) of CESH

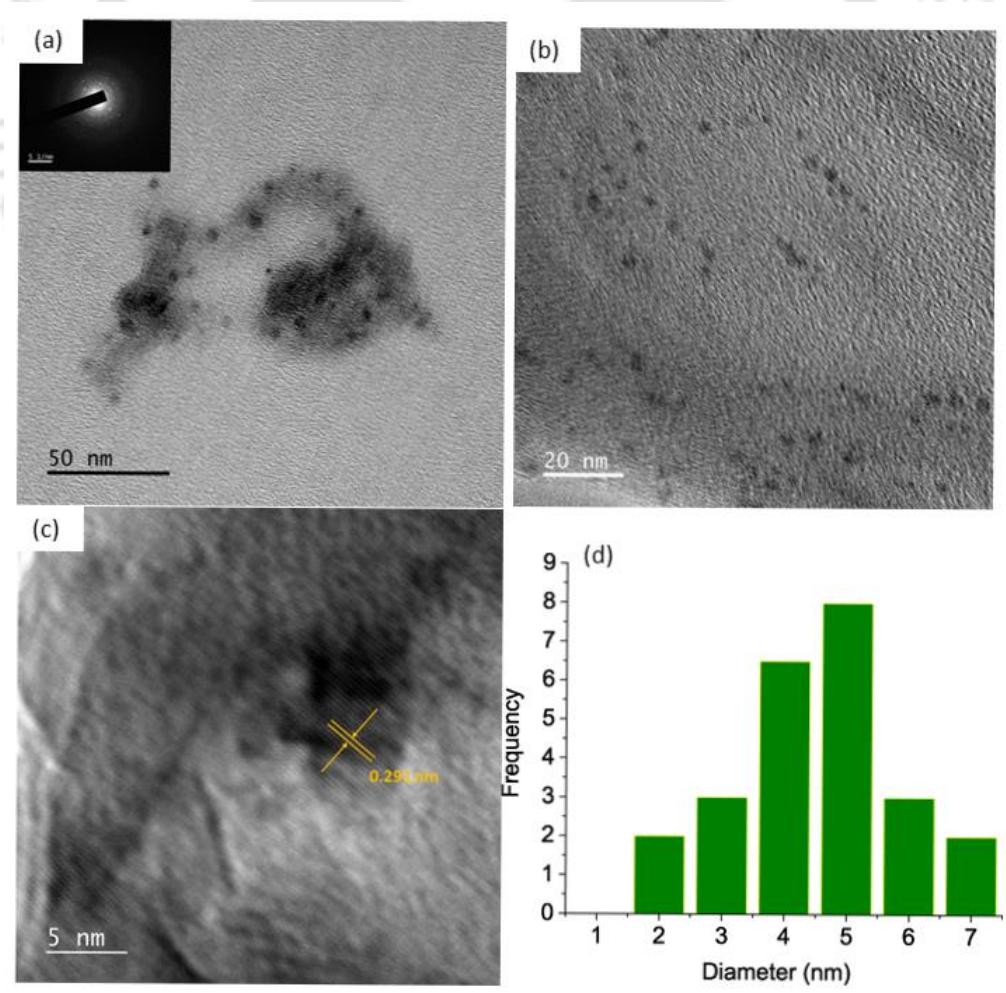

Figure A5.4*:* FETEM images (a-b), HRTEM and (d) Average carbon dot particle diameter.

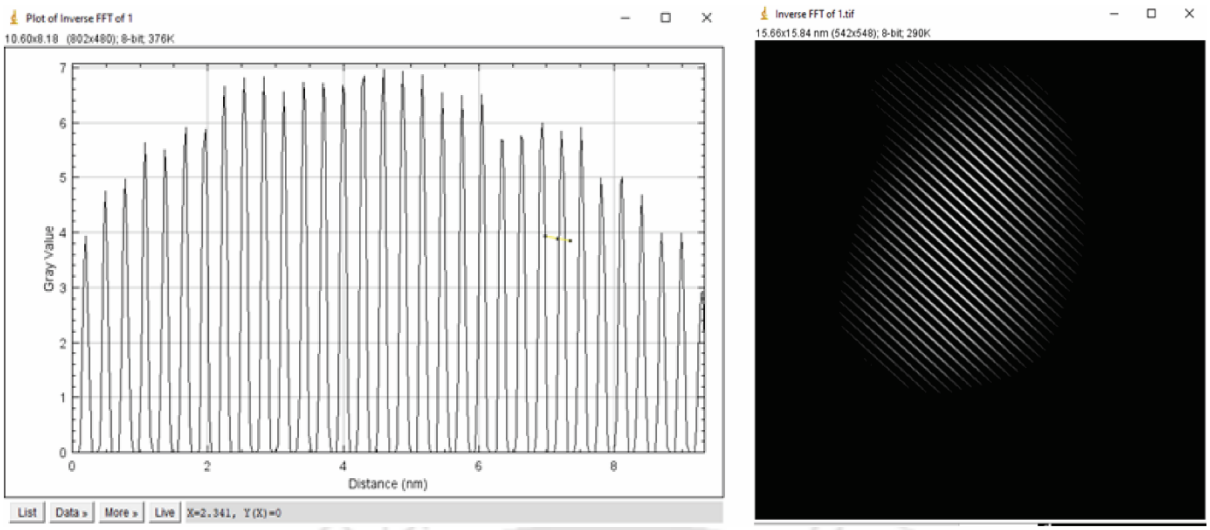

Figure A5.5 HRTEM analysis of carbon dots exhibited lattice fringes with a d-spacing of 0.29 nm

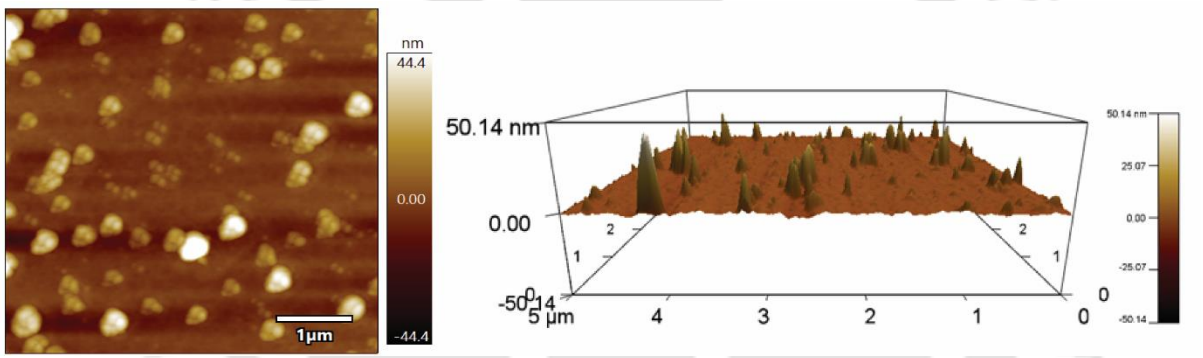

Figure A5.6 AFM image of diluted NCD solution.

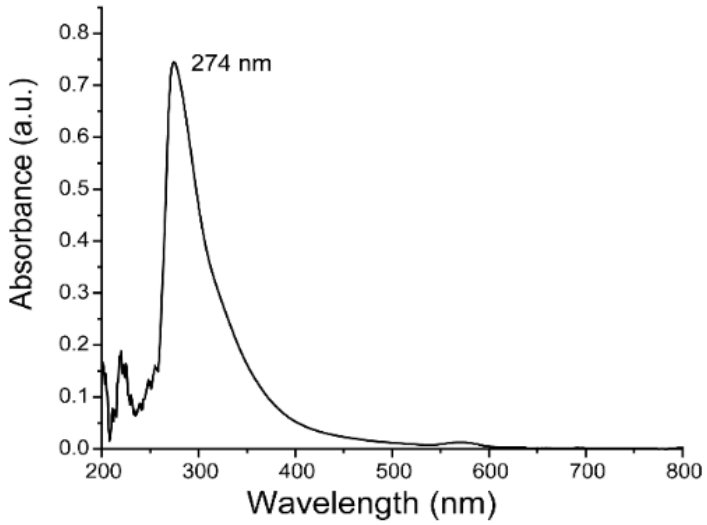

Figure A5.7 UV-Vis spectra of NCDs

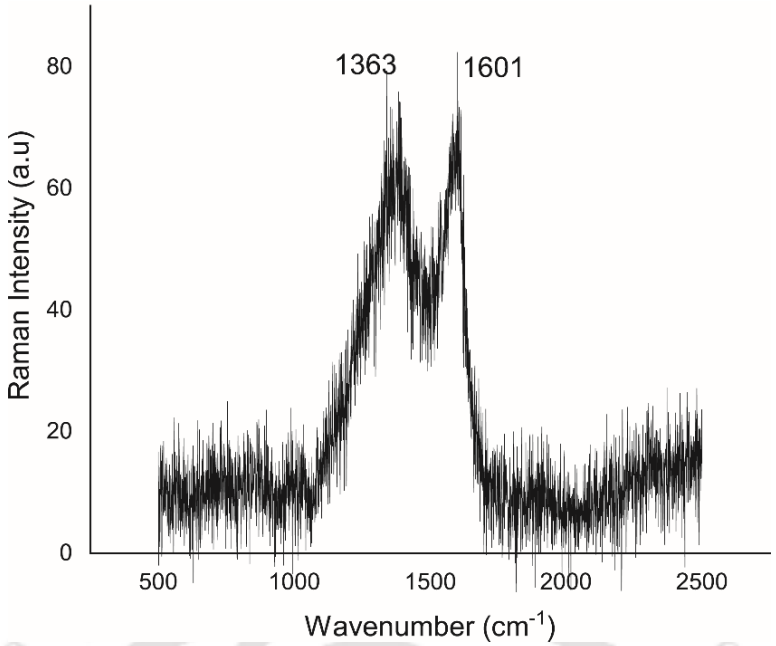

Figure A5.8 Raman spectra of NCDs

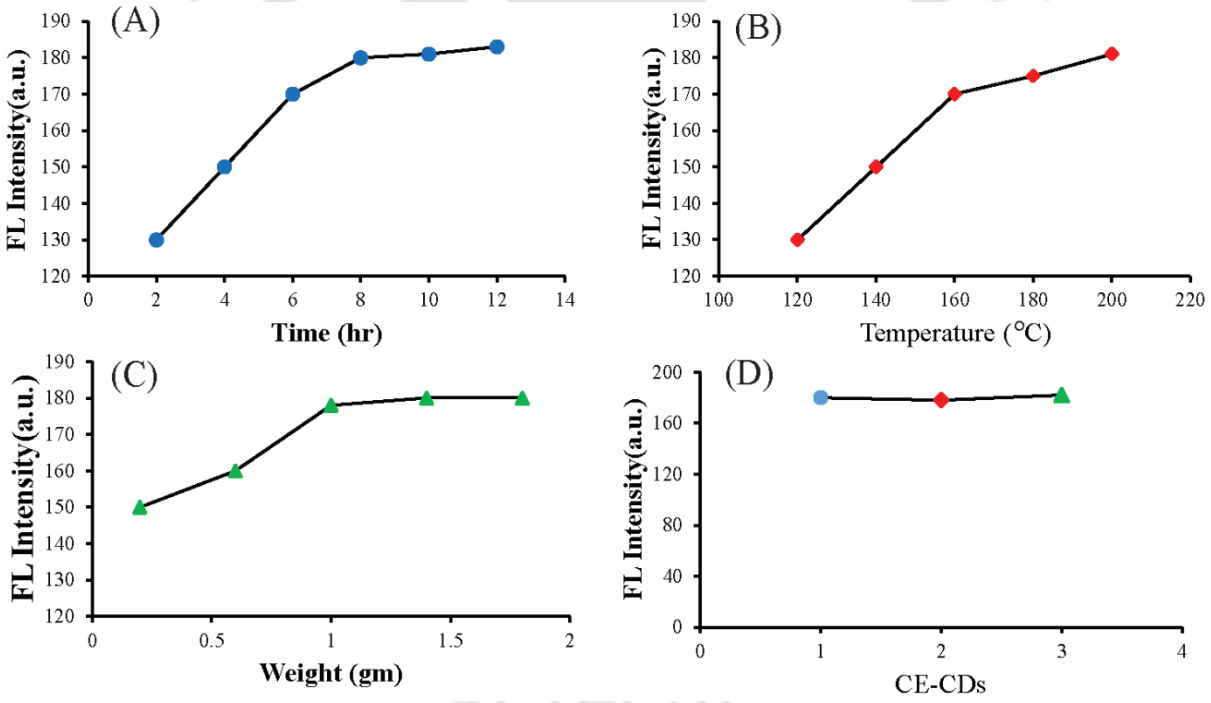

Figure A5.9 Comparison of NCDs prepared at various (A) hydrothermal time durations (2,4,6,8, 10, and 12 h) at 200˚C, B) hydrothermal temperatures (120, 140, 160, 180, 200˚C) for 8 h) (C) weight of CE powder in 50 mL H_2O (0.2, 0.6, 1.4, 1.8 g) at 200˚C of temperature and 8 h of time duration, and (D) the FL intensities of the same synthetic conditions (temperature = 200˚C, time = 8 h, the weight of CE powder = 1.0 g), (excitation wavelength = 357 nm, emission wavelength = 435 nm, slit width=5 nm)

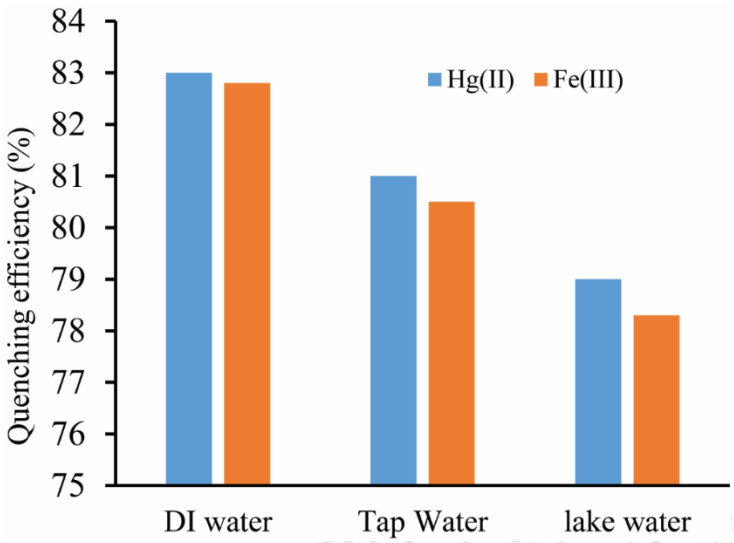

Figure A5.10 Fluorescence quenching efficiency of different water samples spiked with Hg^{2+} and Fe^{3+} ions.

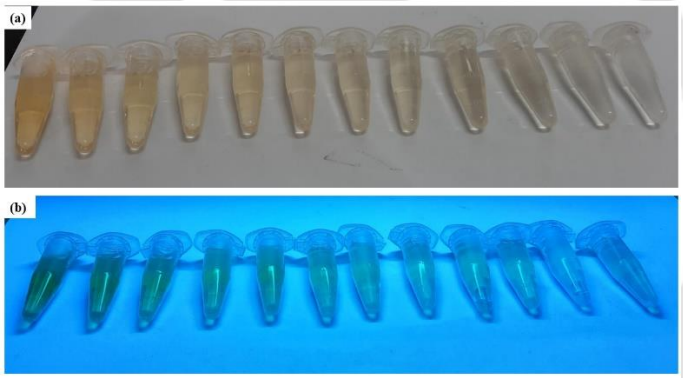

Figure A5.11 Different concentrations of NCDs (a) under normal light and (b) NCDs under UV light

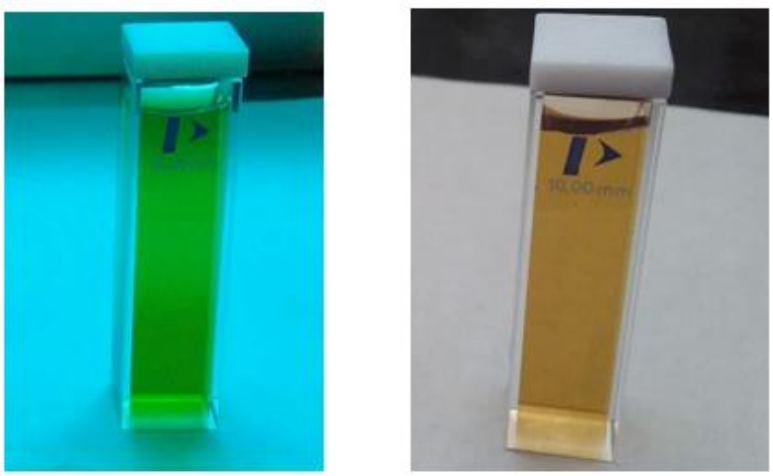

Figure A5.12 NCD (a) Under UV light (b) Under normal light

Conclusion and future perspective

In summary, the present study focused on environmental pollutant removal from an aqueous medium using plant-derived materials such as biochar, hydrochar, and pollutant sensing applications using carbon dots. The key findings of the study are discussed in this part of the thesis. Conclusion of the thesis are mentioned below

- Dye removal study:
  - Plant-derived raw and K_2CO_3 activated biosorbents were explored in the preferential removal of cationic dyes (methylene blue and malachite green).
  - Synthesized biochar at 300˚C which is lower temperature and cost-effective than other reported methods.
  - For these cationic dyes, adsorption followed the Intraparticle diffusion kinetic model and the adsorption mechanism involved is predominantly chemisorption.
  - Adsorption mechanism followed monolayer adsorption explained by Langmuir adsorption isotherm.
  - RCS and RCSB were proved to be stable with good reusability.
  - Cost estimation shows 1 g of RCSB and 1 g CESB production cost is 33 ₹ and 12₹ respectively.
- Heavy metal removal study:
  - Both biochars RCSB and CESB exhibited efficient heavy metal ions removal up to 99%. Adsorption followed by second-order kinetic model and the mechanism involved is predominantly chemisorption.
  - Adsorption mechanism followed by multilayer adsorption explained by Freundlich adsorption isotherm.
  - Synthesized biochar (RCSB and CESB) at 300˚C which is lower temperature and cost-effective than other reported methods.
  - Both activated biochar is a potent economical alternative for wastewater treatment containing heavy metal ions effluent.
- Simultaneous removal of heavy metals using hydrochar and metal sensing using carbon dots
  - Hydrochar (CESH) was prepared using *Colocasia esculanta* stem using the hydrothermal method.
  - Filtrate of the hydrothermal method could be used for carbon dots synthesis and metal sensing applications of Hg^{2+} and Fe^{3+} ions.

- ❖ Adsorption followed the pseudo-second-order kinetic model.
- ❖ Adsorption mechanism involved is predominantly chemisorption.
- ❖ Adsorption mechanism followed by multilayer adsorption explained by Freundlich adsorption isotherm. Thermodynamic studies indicated that adsorption was chemisorptive and endothermic in nature.

Plants are an abundant and renewable source of biomaterials that can be used for a variety of applications, including environmental remediation and nanotechnology. In conclusion, the use of plant-derived biosorbents (Biochar and hydrochar) derived from *Ricinus communis* stem and *Colocasia esculata* stem could be used for the removal of dyes and heavy metals, synthesis of carbon nanoparticles, and the development of metal sensors. These sensors have shown promising results for the detection of a range of metals, including iron and mercury. This biochar has been synthesized at a comparatively lower temperature than previously reported. Cost analysis shows the synthesis process is economic. Further research is needed to optimize the biosorption process, improve the properties of carbon nanoparticles, and develop more sensitive metal sensors. Nevertheless, the potential of plant-derived materials for these applications makes them an attractive and sustainable alternative to conventional materials.

The future scope of plant-derived biosorbents for pollutant removal and carbon dot synthesis holds immense potential in various applications. With growing environmental concerns and the need for sustainable solutions, utilizing plant-based materials as biosorbents offers a renewable and eco-friendly approach to pollutant removal from water. These biosorbents, derived from plants such as agricultural waste, or other biomass sources, can effectively adsorb heavy metals, organic compounds, and even emerging pollutants. Additionally, plant-derived materials can be utilized in the synthesis of carbon dots, which are nanoparticles with unique optical and electronic properties. These carbon dots have applications in diverse fields, including bioimaging, sensing, drug delivery, and energy conversion. The combination of pollutant removal and carbon dot synthesis using plant-derived materials presents a promising avenue for creating sustainable and multifunctional solutions for environmental remediation and advanced technologies.

CURRICULAM VITAE

Partha Protim Bakal
Centre for the Environment
Indian Institute of Technology Guwahati, Guwahati, Assam, India-781039
Email : pbakal@iitg.ac.in, parthabakal@gmail.com
Phone: +919957947447

Academic Summary:

2016-2023: Ph.D. Centre for the Environment, IIT Guwahati
Thesis: Plant-Derived Biosorbents for Pollutant Removal and Carbon Nanoparticle Synthesis.
Supervisor: Prof. Gopal Das
Co-Supervisor: Prof. Aiyagari Ramesh

2004-2005: M.Sc in Inorganic Chemistry (62.18%), Dibrugarh University, Assam

2000-2003: B.Sc. in Chemistry (Major), (60.25%), JIST (Formerly Science College, Jorhat) under Dibrugarh University, Assam

1998-2000: Higher Secondary (10+2) in Science (63%) from AHSEC, Assam

1998 : Secondary Education (10^{th}) (61.44%) from SEBA, Assam

Professional Summary:

2006 : Worked as Research Assistant, Under TIFAC-CORE, Department of Petroleum Technology, Dibrugarh University. (3 months)

2007-2011: Worked as a Research Chemist in Chembiotek (TCG Lifesciences Ltd), Kolkata (March 2007- Jan 2011)

2011-2012: Worked as Sr. Technical Assistant at Guwahati Biotech Park (Feb 2011-Jan 2012)

2012-2018: Worked as Jr. Technical Superintendent at Centre for the Environment, IIT Guwahati (Feb 2012-Aug 2018)

2018-till date: Working as Technical Superintendent Centre for the Environment, IIT Guwahati

Research Interest:

- Biosorption for water pollutant removal.
- Synthesis of Biochar, hydrochar and its application in pollutant removal.
- Carbon nano dot synthesis from plant-based material and its application as a chemosensor in sensing toxic metal ions in aqueous solution.

Expertise:

- All experimental setups for adsorption of organic and inorganic pollutants from aqueous solution.
- Characterization of biomass using various sophisticated analytical instruments.
- Spectroscopic (UV-Vis, Fluorescence, FTIR) , Ion Chromatography (IC), Atomic absorption Spectrophotometer(AAS), Dynamic light Scattering (DLS), HPLC , Column chromatography.

Publications:

1. Bakal, P.P., Das, G. "A Comparative Study of Raw vs. Activated Biochar Derived from "Ricinus communis Stem" for Preferential Removal of Cationic Dyes. Water Conserv Sci Eng 8, 19 (2023). https://doi.org/10.1007/s41101-023-00192-1

2. Partha Protim Bakal, Gopal Das "Biochar Derived from the Stem of Ricinus Communis L. and Colocasia Esculanta: Efficient Adsorbent for the Removal of Cd(II) and Pb(II) Ions from an Aqueous Environment (J. Water Chem. Technol. 45, 200–210 (2023) https://doi.org/10.3103/S1063455X23030025

3. Partha Protim Bakal, Gopal Das, Aiyagari Ramesh, Hydrochar and NCDs derived from *Colocasia esculanta* stem for effective removal and sensing of toxic metal ions. (Manuscript under preparation)

Presentations and workshop/Conference attended:

1. Poster presentation at the Workshop on "Advances in Environmental Protection and Sustainability AEPS 2018" at IIT Guwahati on 2nd June 2018
2. Poster presentation on the topic "Ecofriendly Bio-adsorbent derived from *Ricinus Communis* Stem: Efficient removal of organic and Inorganic Environmental pollutants" in the International Conference "Recycle 2020" on 13-14 February 2020 at IIT Guwahati
3. Oral presentation entitled "Efficient removal of heavy metals and green synthesis & Application of carbon nanoparticles from Ricinus Communis Stem" in the International Conference on Advances in Energy, Environment for Sustainable development (AEESD-2022) organized by Department of Chemistry Siksha O Anusandhan Deemed to be University in Collaboration with Department of Civil Engineering NIT Meghalaya held on 7-8 January 2022

References

1. Prof. Gopal Das (Professor, Department of Chemistry, IIT Guwahati)
   Email : gdas@iitg.ac.in
2. Prof. Aiyagari Ramesh (Professor, Department of Biosciences & Bioengineering, IIT Guwahati), Email: aramesh@iitg.ac.in
3. Prof. Lal Mohan Kundu (Professor, Department of Chemistry, IIT Guwahati)
   Email: lmkundu@iitg.ac.in

Decleration:

I hereby declare that all the information in my curriculum vitae is accurate to the best of my knowledge.

(Partha Protim Bakal) Place: IIT Guwahati, India